Active motion and self-propulsion of polymers and fibers

Arthur Baumann

Université de Strasbourg

UNIVERSITÉ DE STRASBOURG

ECOLE DOCTORALE pcp

École Doctorale physique et chimie-physique

UPR 22: Institut Charles Sadron

THÈSE

présentée par :

Arthur BAUMANN

soutenue le : **20 Décembre 2018**

pour obtenir le grade de : **Docteur de l'université de Strasbourg**

Discipline/ Spécialité : Physique

Active Motion and Self-Propulsion of Polymers and Fibres

THÈSE dirigée par :

Mr. JOHNER Albert, directeur de recherche CNRS, ICS, UPR 22, CNRS-Université de Strasbourg

Mr. KULIĆ Igor, chargé de recherche CNRS, ICS, UPR 22, CNRS-Université de Strasbourg

RAPPORTEURS :

Mr. MOHRBACH Hervé, professeur, ICPM, EA 4632, CNRS-Université de Lorraine

Mr. LÖWEN Hartmut, professeur, C2N, Institut fur Theoretische Physik II, Heinrich-Heine-Universität Düsseldorf

---

AUTRES MEMBRES DU JURY :

Mr. YBERT Christophe, directeur de recherche CNRS, ILM, UMR 5306, CNRS-Université de Lyon I

Mr. DI MEGLIO Jean-Marc, professeur, MSC, UMR 7057, CNRS-Université Paris Diderot

Mme. DRENCKHAN Wiebke, chargée de recherche, ICS, UPR 22, CNRS-Université de Strasbourg

Mr. STOCCO Antonio, chargé de recherche, ICS, UPR 22, CNRS-Université de Strasbourg

Acknowledgments

I would first like to thank deeply anyone taking the time to read this manuscript, it is the legacy of my work and I am very happy to share it with the world. I hope it will be a pleasant read.

On the professional side of things, I am indebted to Igor Kulić who has been mentoring me for the last four years, his incredible ideas motivated me to accomplish all the work presented here. Albert Johner, the second mind behind this PhD was always available for discussions and to tamper unrealistic or overambitious ideas. I was blessed with fantastic collaborators throughout the journey. In IPCMS, Wilfried Grange, Marie-Noëlle Lalloz-Vogel and their numerous interns (Dimitri Andriovitch and Julien Moreau to cite a few) guided me through my first steps in molecular biology. Jacek Arabski, Romain Bernard and all the personnel of the STnano platform made it possible to explore the mysteries of gold with the surfaces they provided me. In my own institute, ICS, I would like to thank the whole M^3 team for their help with sample preparation and handling of the microscope, especially André Shröder for his invaluable experience. I cannot cite all the people that have helped me this last three years but I would like to mention Leandro Jacomine, Fouzia Boulmedais, Olivier Felix, all my fellow members at the BJC, the organizing cast of Fête de la Science and in general all the PhD students for moral support.

A healthy individual takes care of both his body and his mind. I could not have gone through with the PhD without the relief provided by practicing a lot of sports. I would like to thank the rugby team for the weekly dose of suffering, Etienne, Tom, Isatay, Jean-Luc, Thierry, Guillaume & Guillaume, Claire and Robin. I really enjoyed the time I spent on the wall with Tapas, Mel and Etienne. But I learned the most with my other two mentors Pascal and Audrey. I am grateful for all the time spent in the dojo with all the members of the club.

The mind aspect was covered with the interactions with my friends and family. I really enjoyed the "scientific discussions" of Monday evenings that often evolved in board games and cards, with Oussama, Matthieu, Ziyad, Etienne, Julien, Meltem, Thibaut, Andra and all the others. I couldn't go through the days without my lunch and coffee crew, Johanna, Thomas, Edo and Damianos. The progress was punctuated with fantastic reads. I cannot recommend Terry Pratchett enough, his bibliography carried me through almost two whole years of this work. Daniel Kahneman and Eckhart Tolle both enlightened me in their own ways. I thank my musical gurus, Freddy and Manu. I learned a lot through the countless hours spent listening to the advices and stories of Jeff, Tim, Joseph and Mark. The great

Bob Ross provided me with the best sleep in the last months leading to the end of this PhD.

Et je garde le meilleur pour la fin. Je voudrais remercier mes amis proches, Antoine & Antoine, Guillaume, Thierno, Malik, Adrien, Alexis et Simon. Ma chère et tendre qui se reconnaîtra a fait preuve d'une patience à toute épreuve pour me supporter pendant trois ans. Je suis extrêmement redevable de mes parents pour leur soutien et de l'opportunité qu'ils m'ont donné de réaliser ces études, à ma soeur qui a ouvert la voie. Je dédie ce texte à mon grand-père et à Mamoudou Sow. Ils sont d'éternelles sources d'inspiration et je suis sûr qu'ils sont fiers de moi.

Merci à vous

Arthur Baumann

Contents

1 Introduction **15**

2 Motorizing Fibers with Zero Elastic Energy Modes **19**
2.1 Motors with Zero Elastic-Energy Modes 20
2.1.1 Zero Elastic-Energy Modes 20
2.1.2 Examples 22
2.1.3 Principles of Active ZEEM Motion 26
2.2 Theoretical Model 27
2.2.1 Torque Creation, Torque Balance and Thermally Induced Curvature 29
2.2.2 Dynamics of the Temperature Distribution 32
2.2.3 Onset of Motion 33
2.2.4 Energy Storage in Spirals 36
2.3 Outlook 38

3 A Case Study : the Heat-Driven Fiberdrive **41**
3.1 Sample Preparation and Characterization 41
3.2 Fiberdrive 42
3.2.1 The Toroidal Fiberdrive 42
3.2.2 The Spiral Fiberdrive 43
3.3 Fiberboids 48
3.3.1 Annealing of the Linear Fibers 49
3.3.2 Linear and Angular Velocities 52
3.3.3 Thermally-Induced Curvature 53
3.3.4 Dynamics of the Fiberboids 53
3.4 Conclusion 56

4 A Rotary Motor Made out of DNA : the Hyperdrive **57**
4.1 Confotronics 58
4.2 The Hyperdrive design 63
4.2.1 Motivation 63
4.2.2 Conceptual Design 66
4.3 Conclusion 68

5 Ongoing Experimental Endeavors **69**
5.1 Confotronic Fiber 69
5.2 The Hyperdrive 73

5.3 Microscopy Measurements 76
5.4 Conclusion 82

6 Conclusion and Perspectives **83**

A Characterization of the Nylon Fibers **87**
A.1 Mechanical Characterization of Nylon Fibers 87
A.2 Structural Characterization of the Nylon Fibers 88

B Theoretical Description **91**
B.1 Torque Creation, Torque Balance and Thermally -Induced Curvature . . . 91
B.2 Dynamics of the Temperature Distribution 95
B.3 Onset of Motion 98
B.3.1 Fiber Closed to a Circle 98
B.3.2 Straight Fiber 99

C Molecular Biology **101**
C.1 List of Reagents and Compounds 101
C.1.1 List of Reagents 101
C.1.2 List of Oligonucleotides 103
C.2 Experimental Protocols 105
C.2.1 Preparation of DNA samples 105
C.2.2 Gels Preparation 106
C.2.3 Surface Preparation 107

Résumé

Le noyau du manuscrit sera axé sur l'effet Fiberdrive. Un principe de la physique de la matière condensée stipule que chaque fois qu'une symétrie continue d'un système est brisée, un mode "hydrodynamique" pouvant être entraîné avec une énergie pratiquement nulle est créé. Lors de la généralisation de ce concept aux solides élastiques, si l'on prend une tige et rompt la symétrie en la refermant dans une boucle et en formant un tore, un mode de déformation à énergie élastique nulle est "incrusté" dans le matériau. Ceci correspond à la rotation de la fibre autour du grand axe du tore, une "roue à l'intérieur" du matériau. Lorsqu'un flux est appliqué pour déformer la fibre, il peut minimiser son énergie élastique grâce à ce mode zéro en effectuant une rotation. Il en résulte la création du moteur le plus simple imaginable, constitué d'un seul matériau. En considérant des fibres linéaires, la gravité brise la symétrie par confinement dans le plan et le même principe crée des moteurs bidirectionnels.

Un échantillon de modèle sous la forme de fils de nylon 66 de différents diamètres a été étudié de manière approfondie au cours de la présente thèse. Dans ce travail expérimental, une plaque chauffante a été utilisée comme entraînement pour démontrer l'effet des moteurs bidirectionnels pour fibres linéaires ainsi que des moteurs unidirectionnels pour tores et spirales. Le caractère général de cet effet, ancré dans la géométrie de la fibre, a été illustré expérimentalement par l'utilisation de plusieurs polymères, notamment le PDMS, le PVDF et même des spaghettis réguliers. En plus de la preuve expérimentale, un modèle théorique prenant en compte les propriétés élastiques des fibres, leur dissipation ainsi que leur réponse à un stimulus thermique a été dérivé. Ainsi, l'effet était expliqué en détail par de simples considérations physiques.

L'essentiel est le suivant. Lorsqu'une fibre confinée dans le plan (ici la surface de la plaque chauffante) est soumise à un gradient d'énergie (le flux de chaleur de la surface chaude à l'interface fibre / air à température

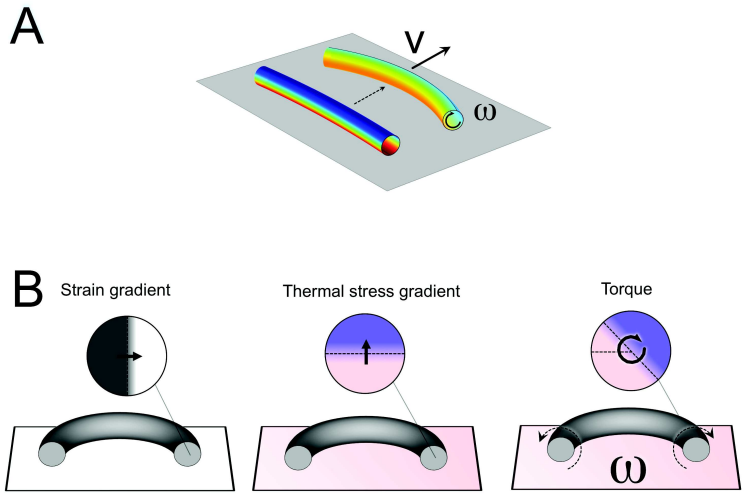

Figure 1: A : Cas de la fibre linéaire bidirectionnelle. B : Cas du tore. De par sa géométrie, il est compréssé à l'intérieur et étiré à l'extérieur, la chaleur provoque plus de compression vers le bas donc la fibre tourne sur elle-même pour minimiser sa frustration.

ambiante), elle crée un gradient de contrainte dans la direction normale à la plaque chauffante qui plie la fibre hors du plan. En raison du confinement dans le plan et pour minimiser son énergie élastique, la fibre tourne alors vers un minimum d'énergie élastique. Le flux de chaleur étant continu, il en résulte une frustration géométrique entraînée de manière dynamique, d'où le mouvement de rotation du moteur. Ce travail à fait l'objet d'une publication dans le journal *Nature Materials* [6].

Conséquemment, il a été démontré que ce mécanisme était beaucoup plus général que cet exemple brut basé sur la chaleur. Avec une géométrie en forme de tige, cet effet peut être généré à une interface par toute forme de flux perpendiculaire à son axe. La prochaine étape de l'enquête est réalisée avec des échantillons d'hydrogel et une fois encore, les spaghettis se déplacent sous l'effet hydroscopique et les gradients d'humidité de la même manière que précédemment. Cependant, dans ce cas, les échelles de temps pertinentes sont ralenties jusqu'à quatre ordres de grandeur. Actuellement, la synthèse de fibres sensibles à la lumière est en cours afin de générer ce type de mouvement par illumination. Toutes ces différentes démonstrations de ce même principe physique du mouvement montrent que ce phénomène est universel et peut-être déjà présent dans les systèmes biologiques, où il existe une abondance de filaments aux interfaces. Une prédiction théorique frappante du modèle est la mise à l'échelle de la vitesse de rotation en fonc-

tion du diamètre des fibres. Plus les fibres sont fines, plus elles devraient être rapides. Cela ouvre la voie à des développements expérimentaux passionnants pour les microsystèmes.

Le reste du manuscrit sera consacré à un projet parallèle expérimental impliquant des structures d'ADN motorisantes liées à des surfaces en or. N'ayant aucune connaissance ni expérience préalable dans ce domaine, le projet n'a pas encore abouti. Cependant, des observations extrêmement intéressantes ont été faites en cours de route. Tout en essayant de visualiser des brins d'ADN marqués par fluorescence, des ondes auto-ADN de fluorescence ont été générées à la surface. Des investigations ultérieures ont montré que la géométrie du système, associée à l'éclairage, donnait lieu à de puissants flux de convection pouvant être dirigés. Ces observations, même si elles ne sont pas encore complètement comprises, méritent un compte rendu attentif dans ce manuscrit.

Le chapitre 2 introduit le concept des modes à énergie élastique nulle (ZEEM). Ce sont des modes de déformation élastiques présents dans les systèmes à rupture de symétrie qui peuvent être entraînés hors d'équilibre par une source d'énergie externe pour créer un nouveau type de mouvement. Cette présentation est suivie d'exemples de tels modes dans le paysage scientifique actuel. Enfin, un système modèle d'un nouveau type de moteur récupérant ce concept est dérivé.

Dans ce chapitre, le concept de la motorisation de machines molles avec un mode à zéro énergie élastique est exploré. Un nouveau paradigme, la "roue intégrée" est décrit. Les exemples simples présentés ici montrént l'utilité et la faisabilité de l'enrobage de la roue et de l'entraînement de polymères et de matériaux banals en tant que moteurs monodirectionnels ou bidirectionnels. Ces fibres se transforment en moteurs robustes constitués d'une seule pièce lorsqu'ils sont éloignés de l'équilibre par la frustration dynamique qui émerge au sein du matériau. Les modes d'énergie élastique nulle s'avérent être vraiment omniprésent dans les matériaux élastiques et dans la nature. Générer une frustration dynamique pour les conduire peut s'avérer aussi simple que de placer un spaghetti ordinaire sur une casserole bien chaude, mais la théorie présentée dans ce chapitre laisse entrevoir de nombreux autres mécanismes moteurs potentiels, tels que les flux de solvants, les espèces ioniques, les flux électriques ou optiques et ouvrent de

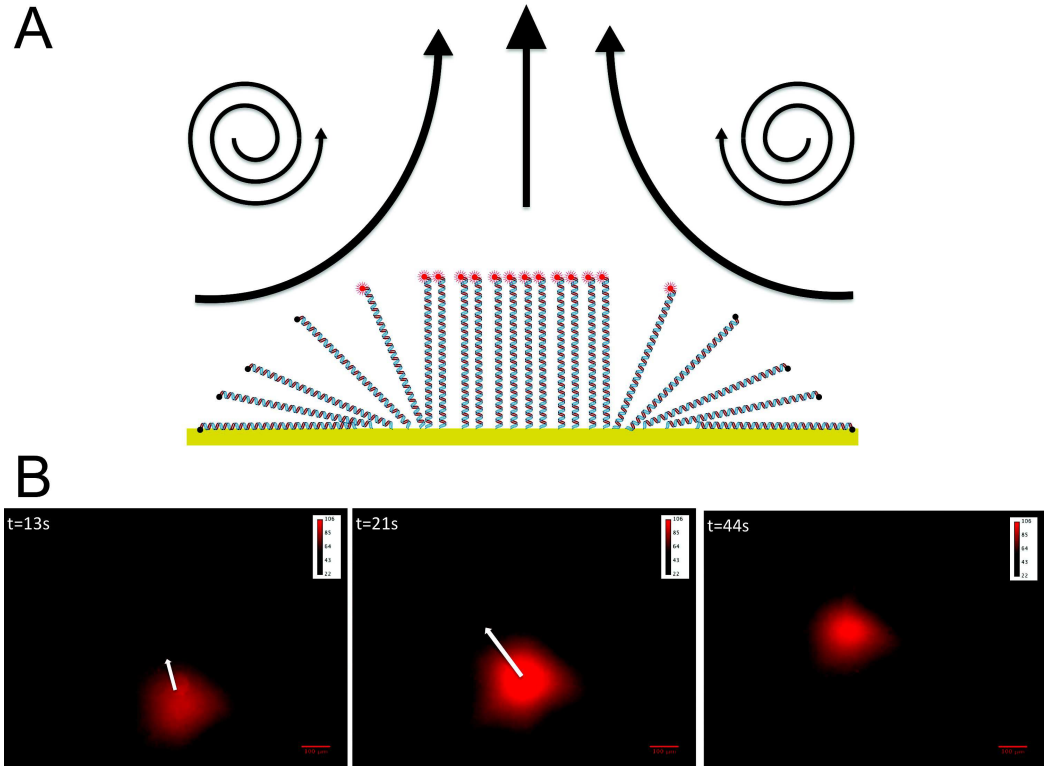

Figure 2: A : ADN marqué par fluorescence attaché sur une surface d'or par des liaisons thiols : la fluorescence est inhibée pour les brins d'ADN trop proches de la surface. L'illumination chauffe l'or et créé un courant de convection dans la chambre d'observation. Le flux soulève les brins et permet l'observation d'un signal de fluorescence. B : Trois étapes de la vague à différents temps après le début de l'illumination, les flèches indiquent la direction de propagation de la vague. Echelle : 100 μm, Carte de couleur : Niveaux de gris 8-bit.

vastes et intéressants terrains de jeux dans les années à venir. Peut-être que les micro-machines les plus complexes seront bientôt alimentées par ce mécanisme. Penser que l'on peut maintenant faire sans le motif classique de roue et d'essieu et utiliser plutôt les modes d'énergie élastique nulle intrinsèques pour induire des mouvements complexes nécessite de repenser le sens même des matériaux intelligents. Cet effet éloigne les projecteurs des propriétés microscopiques finement réglées vers la symétrie et la topologie des systèmes. à travers eux, le matériau physique acquiert une nouvelle forme d'intelligence collective, ne résidant dans aucune de ses parties individuelles, mais pourtant codé de manière globale dans leurs interactions délicates.

Sur une dernière note, compte tenu de la simplicité et de la robustesse d'un tel mouvement, il est probable qu'il est de nature omniprésente et que les mystères scientifiques pourraient être résolus en les considérant sous cet angle. Dans les systèmes biologiques, il existe une abondance de biofilaments confinés aux interfaces. L'effet Pickering tend à y confiner les fibres, ce qui est exactement l'une des conditions du mouvement induit par les modes d'énergie élastique nulle. Compte tenu de la forme inhabituelle des filaments de filovirus, tels que les virus de Marburg et Ebola, ils pourraient présenter une forme possible de motilité de roulement de surface entraînée par le gradient.

Le chapitre 3 présente une série de réalisations expérimentales du système modèle décrit au chapitre 2. Les fibres polymères les plus simples sont utilisées pour créer le moteur le plus simple imaginable, constitué d'un matériau unique, la fibre elle-même, tournant autour de lui-même. Cette machine souple - la roue "intégrée" - est étudiée en profondeur ainsi que d'autres géométries utilisant un type de mouvement piloté par un mode d'énergie élatique nulle.

Ce chapitre est consacré au compte-rendu de la première démonstration expérimentale de l'effet Fiberdrive et Fiberboid. Les différents échantillons utilisés dans les expériences sont brièvement décrits avant de donner les détails de la conception du fibredrive. Il présente d'intéressantes propriétés auto-cicatrisantes et peut être étendu au dessin en spirale pour le rendre plus pratique. Pour les fibres optiques, la procédure de recuit est expliquée

ainsi que quelques considérations géométriques intéressantes. Pour les deux systèmes, les résultats expérimentaux sont comparés à la théorie présentée dans le chapitre précédent lorsque cela est possible.

Les travaux expérimentaux présentés dans ce chapitre montrent la faisabilité pratique de la "roue incorporée" décrite dans le précédent en utilisant de simples fibres polymères disponibles dans le commerce. Les fibres optiques toroïdales et spiralées, ainsi que les fibres optiques linéaires, constituent des moteurs mous monoblocs qui présentent un mouvement unidirectionnel et bidirectionnel lorsqu'ils sont hors d'équilibre par une source de chaleur. Cela montre que le concept abstrait des modes d'énergie élastique nulle peut être utilisé pour générer de vraies machines capables d?effectuer un travail. Les détails du modèle ainsi que certaines expériences préliminaires impliquent que de nombreux autres mécanismes moteurs peuvent induire une telle rotation. Le flux de chaleur peut être remplacé par un gradient d'humidité, des gradients d'ions ou un éclairage lumineux, à condition qu'ils soient couplés élastiquement au matériau. Le nouveau paradigme du mouvement basé sur les modes d'énergie élastique nulle appelle à une révolution dans le domaine des machines molles. Les géométries étudiées ici sont les plus simples imaginables et ne représentent qu?une preuve de concept. Les propriétés de mise à l?échelle de la vitesse des fibres linéaires à fibres optiques vont dans le sens de la miniaturisation de telles machines, tirant peut-être parti de leurs propriétés collectives.

Le chapitre 4 entre dans les détails de la motivation initiale de cette thèse, la synthèse d'une fibre artificielle confotronique. Il définit d'abord le domaine de la confotronique avec quelques exemples trouvés dans la nature, puis décrit une conception utilisant des structures d'ADN ramifiées comme monomère pour un polymère confotronique. Dans une seconde partie, nous nous sommes inspirés des travaux en cours sur la nanotechnologie de l'ADN et des travaux antérieurs de ce groupe afin de créer un nanomoteur rotatif à base d'ADN, l'Hyperdrive. Sa conception et ses mécanismes d'actionnement sont présentés.

Ce chapitre reprend le thème principal des précédents - "le matériel est la machine". Un concept pour un nanomoteur rotatif à base d'ADN est présenté. De la même manière que pour le fibredrive, l'action rotative du

moteur provient de la géométrie et de la topologie de l'assemblage de l'ADN. Avant de suivre le cheminement vers l'étude des modes d'énergie élastique nulle et des machines molles, l'objectif initial de la thèse était d'étudier la mécanique statistique des biofilaments confotroniques. La première partie de ce chapitre est consacrée à la définition du concept global de la confotronique, d?un point de vue conceptuel général, à la description d?une fibre confotronique à base d?ADN. La deuxième partie explique comment l'étude des travaux récents sur la commutation électrique d'assemblages d'ADN greffés sur des surfaces en or, couplée à une expertise antérieure dans le domaine des machines moléculaires, a orienté le projet vers la fabrication d'un nanomoteur à base d'ADN. Enfin, la conception et les principes de fonctionnement du moteur sont présentés.

Dans ce chapitre, le concept de la confotronics est décrit. Cela peut être défini comme l'étude de grands systèmes composés d'unités commutables individuellement. De nombreux exemples peuvent être trouvés dans la nature et, étant donné les dénominateurs communs dans ces exemples, il est possible de concevoir une idée de systèmes synthétiques confotroniques. Un tel système est décrit sous la forme d?une fibre confotronique à base d?ADN, exploitant les propriétés de la jonction de Holliday pour intégrer des caractéristiques collectives dans un polymère synthétique.

Les travaux antérieurs de ce groupe sur le tanglotron sont brièvement présentés. Cela a servi, avec la fonctionnalité de migration de la jonction Holliday et le travail sur la construction d'ADN commutable électriquement greffée sur des surfaces dorées, comme motivation pour la conception d'un nanomoteur rotatif fabriqué à partir d'ADN. Ce moteur - l'hyperdrive - combine toutes les idées précédentes en un seul et même projet. Il s?agit d?une construction d?ADN à actionnement électrique greffée sur une électrode en or qui transmet le mouvement de rotation d?une construction basée sur une jonction Holliday à une perle de taille micromètrique. Il associe efficacement des échelles de longueur nanométriques à des objets de taille micrométrique.

Le chapitre 5 est consacré aux travaux expérimentaux en cours qui, à la différence des fibres optiques et des fibres optiques, ne pourraient pas être terminés à la fin des trois années. Les progrès actuels sur la fibre confotronique et l'Hyperdrive sont présentés en premier. La dernière partie du chapitre traite des découvertes inattendues survenues lors de la tentative

de visualisation de l'ADN sur une surface dorée. Il donne une explication possible des phénomènes observés sous la forme d'écoulements de convection induits par la lumière dans les chambres d'observation causés par l'éclairage.

Dans ce chapitre, plusieurs projets expérimentaux en cours sont discutés. Pour tous, ils ont commencé au cours de la thèse de doctorat sans aucune connaissance préalable dans le domaine. Le budget de ces projets étant très limité, les premières étapes (présentées ici) ont toutes été effectuées en interne ou dans l'institut voisin (Institut de physique et de chimie des matériaux de Strasbourg ou IPCMS). étant donné le stade très précoce du développement, la plupart des résultats sont qualitatifs plutôt que quantitatifs et certains n?ont pas d?explication appropriée. Pour la plupart, les expériences sont réalisées sur le terrain ou en biologie moléculaire. Ils ont été réalisés dans l'IPCMS sous la direction d'un proche collaborateur biophysicien, le Dr. Wilfried Grange. Certains des protocoles ont été créés par lui et d?autres ont été conçus après avoir étudié la littérature scientifique. Par souci de brièveté, seules les tentatives "réussies" sont rapportées ici. Les détails des procédures expérimentales sont dans autoref chp: biology.

Deux projets sont présentés ici. La première est une brève excursion dans la fabrication de la fibre confotronique présentée dans autoref sect: confotheory. La seconde concerne le nanomoteur Hyperdrive. Sa conception et sa construction sont détaillées et suivies par la présentation d'un intéressant contretemps expérimental. En essayant d'observer de l'ADN marqué par fluorescence greffé sur une surface dorée, une autowave fluorescente se forme. Cette onde est la conséquence d?écoulements de convection supposés être induits par le chauffage de la surface de l?or par la lumière d?excitation. Ce flux est décrit et les pistes possibles pour ses applications sont explorées.

Ce chapitre présente les développements expérimentaux réalisés sur trois projets différents: la fibre confotronique, le nanomoteur Hyperdrive et le flux de convection induit par la lumière. La courte présentation faite ici a masqué tous les échecs rencontrés sur le chemin afin de présenter uniquement les résultats finaux et les protocoles. Partir de zéro sans aucune connaissance préalable dans les domaines de la biologie moléculaire et de la microscopie était certes une tâche difficile, mais il s'agissait d'un voyage merveilleux, riche en découvertes intéressantes.

Un expérimentateur plus chevronné n'aurait peut-être pas passé autant de temps sur ce phénomène bizarre de "taches", ignorant les flux induits par la lumière. Dans l'état actuel des choses, ces projets n'attendent que des hommes pour être orientés dans de nouvelles directions. La fibre confotronique pourrait bientôt devenir un axone artificiel, tandis que la structuration en or sur des surfaces pourrait être la clé d'un écoulement facile, contrôlé de l'extérieur et précis dans les solutions. Quant à l?Hyperdrive qui était le projet clé de cette partie, le tanglotron avait déjà montré que le couplage du nanomètre et de l?échelle micrométrique était possible. .

Chapter 1

Introduction

Machines have always been a fascination and the source of some of the greatest dreams of mankind. Even at the age of simple machines (see Fig. 1.1), Archimedes quoted by Pappus of Alexandria allegedly said "Give me the place to stand, and I shall move the earth", talking about the lever. The Egyptians actually moved the earth while constructing some of the most jaw-dropping monuments built to date, the great pyramids. To achieve this remarkable feat, they used a combination of these simple machines with physical ingenuity [1].

At the turn of the XVII$^{\text{th}}$ and XIX$^{\text{th}}$ centuries, the co-development of electrical science along with steam technologies was the main trigger behind the industrial revolution. This period has seen the world radically change with the transition from hand production to large scale production methods, the rise of chemical industries, new iron production processes but mostly the development of machine tools that enabled the creation of the factory system. Machines that were until then a helpful tool at the service of humanity became omnipresent and perfused all aspects of daily life. Today, complex machines using all the scientific knowledge available from classical mechanics, fluid mechanics, chemistry and thermodynamics can be found literally everywhere. From the fridge and the microwave in kitchens, showers and toilet in the bathroom to the multitude of motorized vehicles, one cannot spend a single day without encountering one of them. They feed us, heat us and drive us all around the world in cars, boats and planes.

Yet all of this is nothing but the tip of the iceberg. The advance of microscopy techniques in the past century enabled biologists, chemists and physicists alike to marvel at the complexity of living systems. And it didn't take long for them to notice that life is extremely talented in creating its own complex machinery. For instance, a literal gear [2] can be found in the planthopper insect *Issus*. When considering the realm of the human body, biological machines [3] can be found at almost every level of description, from the great mechanical pump that is the heart, to the smallest molecular motors [4] myosin, kinesin and dynein running along biofilaments. Allosteric regulation is used to control enzymatic action while ion channels act as customs granting or denying entry within cells. All these protein machines [5] are at the core of the central dogma, the processes whereby the genetic information is expressed chemically within the body.

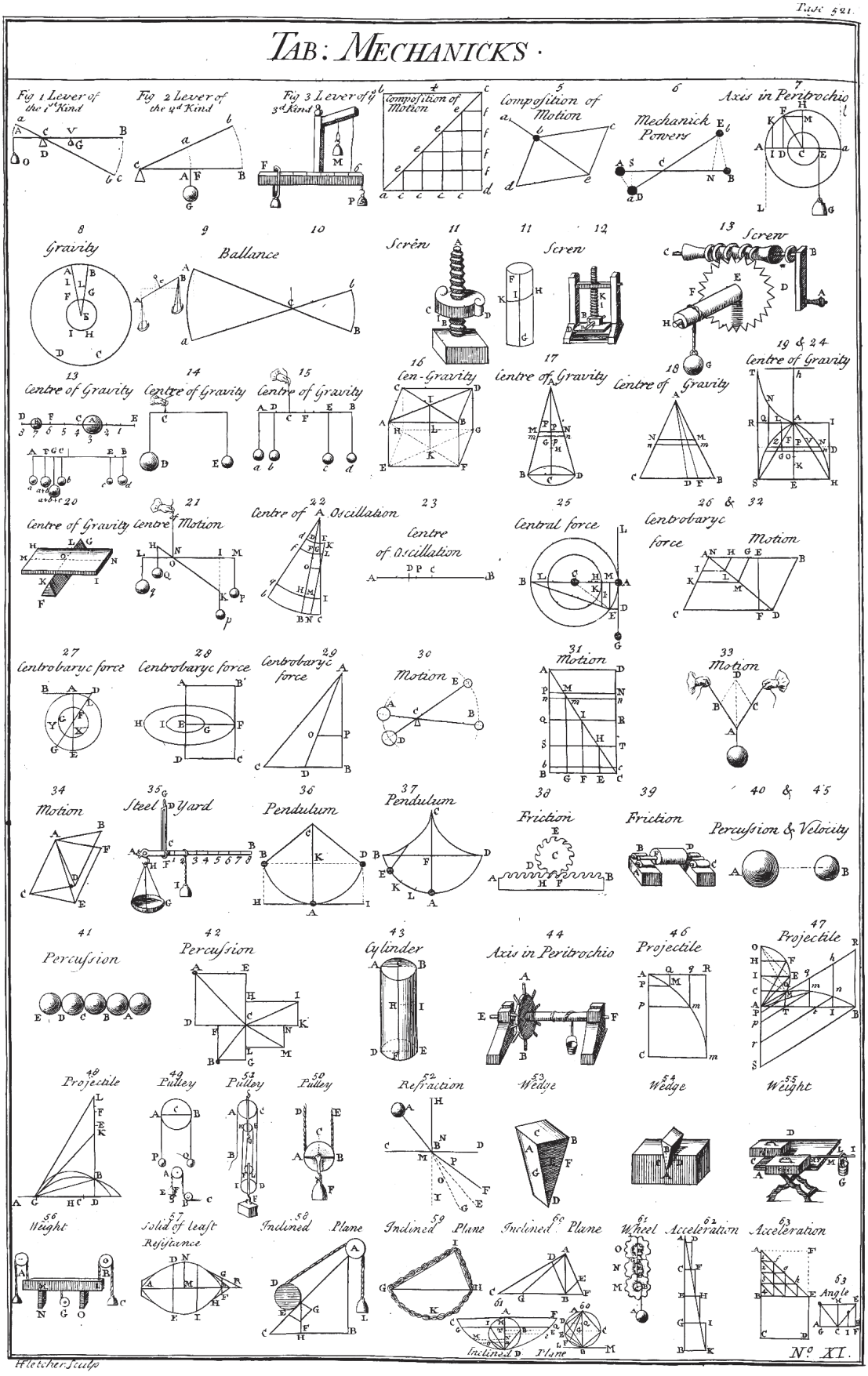

Figure 1.1: Table of simple mechanisms, from *Chambers' Cyclopaedia*, 1728.

The discovery of this molecular machinery called for the creation of artificial counterparts in the pure tradition of biomimetics. The current scientific literature is overflowing from marvelous examples of man made artificial machines from nano to microscale, developed with a wide array of smart materials. This manuscript will present some of them along with the one that was invented during the course of this PhD. One of the bold aims of this work is actually to reinvent the wheel [6].

Chapter 2 introduces the concept of zero elastic-energy modes (ZEEMs). These are modes of elastic deformation present in symmetry-breaking systems that can be driven out-of-equilibrium by an external source of energy to create a new type of motion. This presentation is followed by examples of such modes in the current scientific landscape. Finally, a model system of a new type of engine harvesting this concept is derived.

Chapter 3 presents an experimental realizations of the model system described in chapter 2. Mundane polymer fibers are used to create the simplest motor imaginable, consisting of a unique piece of material, the fiber itself, rotating around itself. This soft machine - the "embedded" wheel - is studied in depth along with other geometries that are using ZEEMs-driven type of motion.

Chapter 4 goes into details in the original motivation of this PhD work, the synthesis of an artificial confotronic fiber. It first defines the field of confotronics along with some examples found in nature and then describes the a design using branched DNA structures as monomer for a confotronic polymer. In a second part, inspiration is taken from current studies done in DNA nanotechnology as well as from previous work done in this group in order to create a rotary nanomotor made out of DNA, the Hyperdrive. Its design and actuation mechanisms are presented.

Chapter 5 is dedicated to ongoing experimental works that unlike the fiberdrives and fiberboyds could not be finished in time by the end of the three years. Current progress on the confotronic fiber and the Hyperdrive are presented first. The last part of the chapter deals with unexpected discoveries that arose when trying to visualize DNA on gold surface. It gives a possible explanation of the phenomena observed in the form of light-induced convection flows in the observation chambers caused by the illumination.

Chapter 2

Motorizing Fibers with Zero Elastic Energy Modes

In the last half-century, new developments in material science led to the design of responsive materials [7, 8, 9] that have been used to generate various structures with built-in complex geometries (such as the morphing of 2-dimensional (2D) sheets into 3-dimensional (3D) material via a differential concentration of monomer constituents [10], the design of temperature-responsive gel sheets through halftone gel lithography [11] or geometric composite structures that deform by residual swelling [12]), linear actuators(electrically actuated elastomer sheets [13], thermally actuated threads made of fishing line [14] and a wide range of artificial muscles driven via electrostatic forces, electrostriction, ion insertion and molecular conformational changes [15]) and microswimmers (assembly of colloidal magnetic particles driven by an external magnetic field [16], liquid-crystal elastomers (LCE) [17] and hydrogels [18] actuated by light). These results surely hint at complex, fully functional machines composed solely of shape-changing materials [19]. The monopol of directed motion achieved through the conversion of external energy from the medium was once held by living systems, with systems that harvest energy provided by nutrients such as swimming bacteria [20], crawling cells [21] or the molecular motors that hydrolyse adenosine triphosphate (ATP) to achieve direct motion [22]. Non-living systems that can achieve the same features have been described. Examples include Janus colloids that use a chemical catalyst to achieve self-propulsion [23] or the Quincke rollers [24], dielectric particles propelled through a conducting fluid by an electric field. Despite these elegant designs, so far rotary machines made from these materials always relied on the classical wheel and axle motif.

This chapter describes what is possibly the simplest possible machine made to date, an "embedded wheel" made out of a single piece of material. In the first part, geometric zero-energy modes needed to elicit the rotation in elastic materials are introduced. Secondly, a theoretical model describing the physical mechanism at play is derived and then finally future possibilities are discussed.

2.1 Motors with Zero Elastic-Energy Modes

2.1.1 Zero Elastic-Energy Modes

In the field of smart materials, a significant amount of research has been done to build artificial actuators, simple machines capable of producing translational motion. Among those, some respond to light as an external stimuli (systems as LCE fibers swimming in the dark [17] or LCE sheet-rings rolling on a suface [25], oscillating azobenzene sheets [26] or liquid crystal polymer networks embedded with azobenzene molecules [27], photoactuators based on carbon nanotubes [28] and finally hydrogel based actuators [29]), others to electric stresses (to provoke the collapse of hydrogels [9] or to accentuate the stress/strain response in prestrain dielectric elastomers [13]) and osmotic stresses [30] (with transport of ions within polymers [15], polymer composite driven by water gradients [31]). However, these systems are limited to a simple linear motion and miss out on the complexity and potential that can be attained with the remaining concepts of classical mechanical machines. In order to build truly complex continuum machines, one needs to take a step back from the complexity of smart materials and first reflect on the geometry, topology and symmetry of the sample.

This part is about frustration and its duality with motion, in particular how various forms of frustration can lead to continuous motion in dissipative, driven materials. There can be no complex motion without frustration, a catalyst to change the mechanical, chemical or thermodynamical state of the system from one moment to the next. Indeed, all natural shape and motion emerge from frustration. In a physical sense, one describes frustration as the inability of a system as a whole to reach a stress-free equilibrium state, at any time, in the mechanical and/or in the thermodynamic sense. In the following, soft machines driven by global zero elastic-energy modes (ZEEMs) are discussed, mechanically frustrated systems that structurally encode their own motion. They are similar to classical (both macroscopic and microscopic) motors, active objects that harvest and dissipate energy to create motion in a continuous manner.

Potentially the earliest of such continuous motion-encoding system is the wheel and axle motif. When attaching a wheel (rotor) onto a static axle (stator), its rotation round the axle becomes the natural mode of motion for this system. In this work, the wheel is reinvented in a new motif, with a twist. Utilizing elastic material and smart topological design, a machine made out of a single component but still displaying a continuous cyclic motion is created.

The general idea behind it is to generate and actively drive cyclic zero-modes in elastic objects with internally trapped mechanical prestrains. It is known among condensed matter physicist in a principle stated by the hydrodynamic Goldstone theorem [32, 30, 33] that when the continuous symmetry of a system is broken, a zero wavenumber, zero frequency "hydrodynamic" mode emerges [34, 35]. This "symmetry restoring" deformation can be applied to the system without changing its energy. Some most classical examples are the nematic phase in liquid crystals in which the rotation symmetry is broken by the director, the ordered spin phase in the XY model where the rotational symmetry is broken by the

spin orientation [34]. Considering virtually no energy cost to rotate the molecules or spins collectively, the corresponding long wavelength distortion becomes a new hydrodynamic variable in the system.

When generalizing the concept to elastic solids with the introduction of zero elastic-energy modes, the proposed model in this manuscript, coined "the embedded wheel", allows the construction of soft motors into responsive materials. Their operation is enabled by inducing and actively driving out-of-equilibrium elastic modes in systems that bear internally trapped mechanical prestrains.

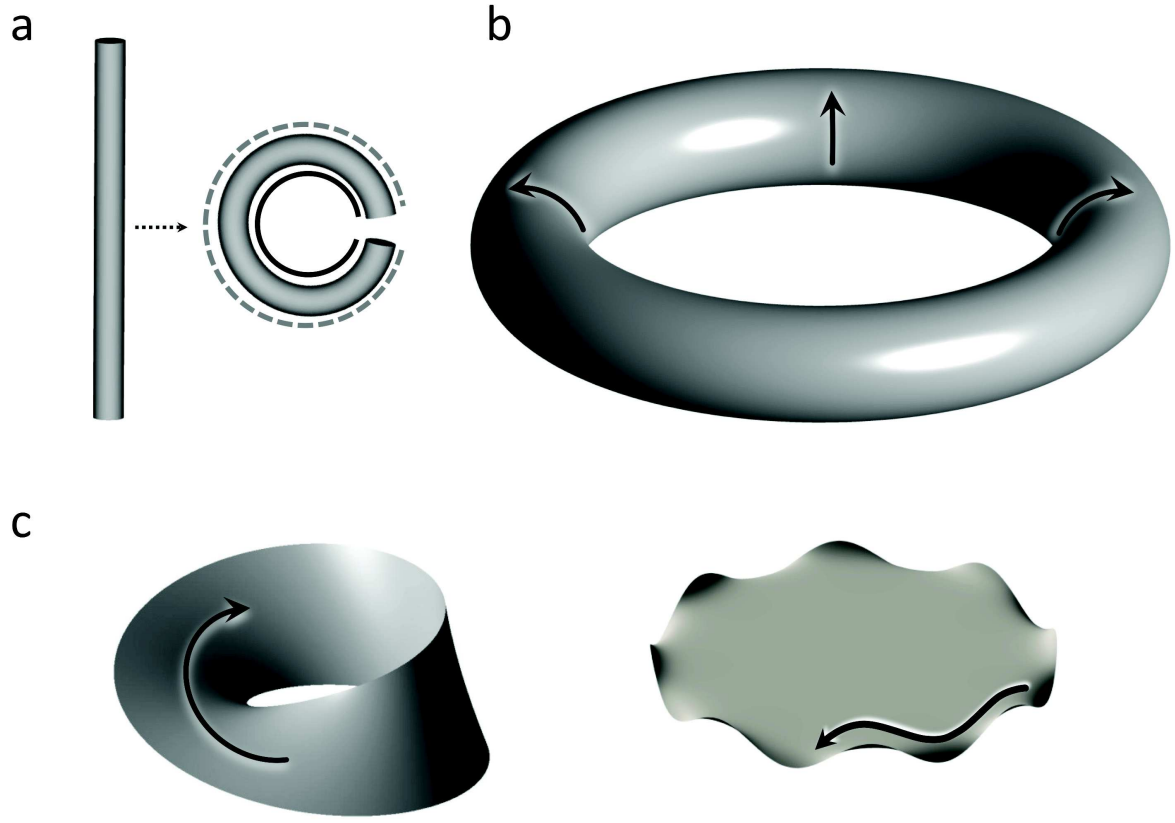

Figure 2.1: **"The embedded wheel" paradigm : Global zero elastic energy modes (ZEEMs) in prestrained elastic objects.** a) Closing an elastic fiber into a ring induces compressive strain in the inner portion (solid line) and tensile strain on the outside (dashed line). b) The torus now has a deformation mode that leaves its elastic energy unchanged : the collective rotation of the fiber's cross-sections around their axis. c) A wide array of elastic objects such as a Möbius strip or an edge-crumpled disk possess global ZEEMs.

One of the simplest examples of such an object is depicted in Fig. 2.1 a). An elastic rod, initially straight is closed into a circular loop. By adopting the shape of a torus, the initially cylindrical rod is now displaying compressive strain on the inside (dark line) and tensile strain on the outside (dashed line). The system is prestrained by its topology and

the initial symmetry is broken. In a similar fashion to the hydrodynamic scenario, this breaking of the rotational symmetry around the rod's axis creates a zero-energy mode : the collective rotation of the fiber's cross-sections around their axis, see Fig. 2.1 b). In an perfect elastic material, without viscous dissipation and no defects, this mode of deformation would truly cost no energy.

These global zero elastic-energy modes are not restricted to the one example of toroidal geometry [35, 36], and are actually surprisingly common in nature. On the macroscopic scale, they can be found in the wrinkles on the surfaces of elastic objects [37], the ripples on edge-stressed sheets [13, 37], in isometric excess-angle cones [38] or in the sliding of the kink in a Möbius strip along its surface [39], see Fig. 2.1 c). On the microscopic scale, a ZEEM can be observed in the "slithering" (conveyor-belt-like type of motion) of plectonemic supercoils along closed DNA (deoxyribonucleic acid) molecules that brings together in juxtaposition specific sites of the sequence [40], in the "universal-joint" reshaping of the bacterial flagellum hook [41, 42], the wobbling motion of microtubules [43] and in the propulsion of left and right-handed kinks along the contractile sheet of the bacterium spiroplasma [44, 45, 46, 47, 48].

2.1.2 Examples

All previous examples might seem rather complex and abstract but there are actually rather mundane examples that can be witnessed on a daily basis. This type of motion happens spontaneously in an emergent, self-organized manner. A phenomenon observed all around the world in the summer is the bending of initially straight sausages upon cooking, something often overlooked as a transient thermo-elastic phenomenon. But if one is lucky enough to get exactly the right type of sausage, something incredible happens, it starts to rotate around its long axis and self-bakes in the pan, see Fig. 2.2. A possible explanation could be that the sausage's moisture vaporizes at the contact with the hot pan and the expanding gas creates a force strong enough to propel it, in a similar fashion to droplets propelled by the Leidenfrost effect [49, 50, 51]. But this explanation can be overruled when considering a similar yet completely different sample. When taking a piece of cylindrical dried starch (a simple spaghetti !) and putting it onto a hot plate, the same rolling-type of motion can be observed, it rolls across the surface.

A better understanding of the driving mechanism can be obtained by looking at another common example given by nature. The bending and preferential growing direction of every plant towards the sun, called phototropism [53] was first reported by the end of the XIX$^{\text{th}}$ century by none other than Charles Darwin [54]. In this book, Darwin describes a mysterious substance (later revealed to be auxin) that is transduced from the tip of the seedling, where the light signal is perceived, to lower portions of the seedling, where the signal response can be observed in the form of directional growth changes. The accumulation of auxin in the shadowy side of the plant induces a tensile strain that bends the tip towards the light source, see Fig. 2.3. This process is active and maintained throughout the whole life cycle of the plant, enabling it to adapt to any change of environment provided it gets enough light to sustain photosynthesis.

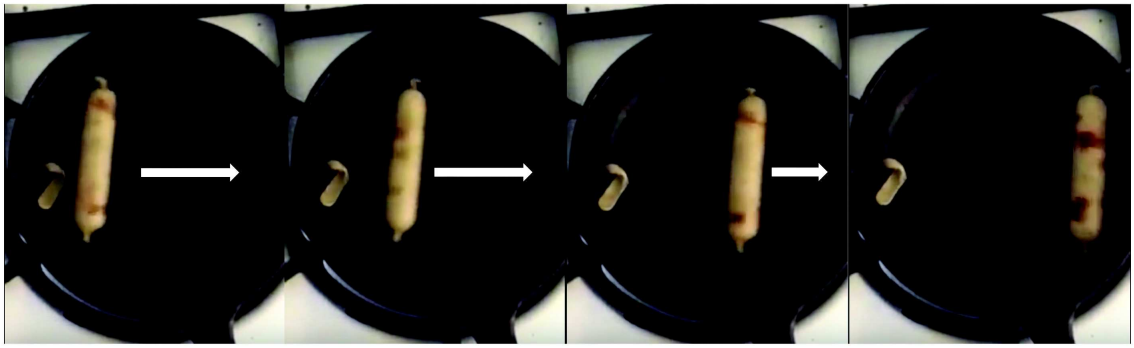

Figure 2.2: A sausage rolling on the inside of a pan upon cooking, the four consequent images span approximately one second, see [52].

Soft machines driven along their ZEEMs are conceptually far more general than spinning sausages and spaghettis which are merely one of the simplest realization. Another prototype is the case of the ring described above. Taking a simple piece of nylon fishing line and closing it into a loop creates the "embedded wheel". When placing the ring onto a hot plate of a temperature of about 160-180°C, it starts to turn after a short warm up of about a second, cf. Fig. 2.4. What is observed is not actually rotation in the classical sense, it is a continuous collective reshaping of the fiber's cross-sections around their axis. It has a definite directionality for any given material. For nylon and polyvinylidene difluoride (PVDF), the upper portion of the fiber moves to the outside of the center line. A polydimethylsiloxane (PDMS) ring will turn in the opposite way with respect to the nylon ring. The direction in which the ring moves is dictated by the sign of the thermal expansion coefficient $\alpha_{\parallel}$ as will be seen in the theoretical part later on. Nylon is contracting upon heating and thus rotates inwards whereas the thermally expanding PDMS rotates in the opposite direction, cf. Fig. 2.4.

In analogy with sausage and spaghetti, the same experiment can be performed with a straight piece of polymer fiber in a very robust and reproducible manner. When placing the fiber on the hot surface, it bends slightly and starts to rapidly roll on the surface, see Fig. 2.5. The initial direction of movement is random and these fibers are actually bidirectional motors that can switch direction when confronted to an obstacle or hindered in some way. When confined between two parallel obstacles, the motion can be observed reliably for hours. As was the case with the torus, the open fiber is not rotating and rolling, but rather consistently reshaping in its own reference frame (a pure classical rotation of the whole sample is not possible with the active curvature displayed here). The motion observed is again a ZEEM that is actively driven. This time though, it is not imposed by the geometry of the sample but emerges through a self-induced buckling of the fiber on the plate. Looking back at the spaghetti example, another interesting observation can be made. If after running it for a few seconds in a hot pan, it is put onto a cold surface at room temperature (around 20°C), the spaghetti still rolls on the surface sometimes even more rapidly than before. On this surface, the spaghetti will invert its movement direction with respect to its curvature direction. This effect is inherent to the phenomenon and also

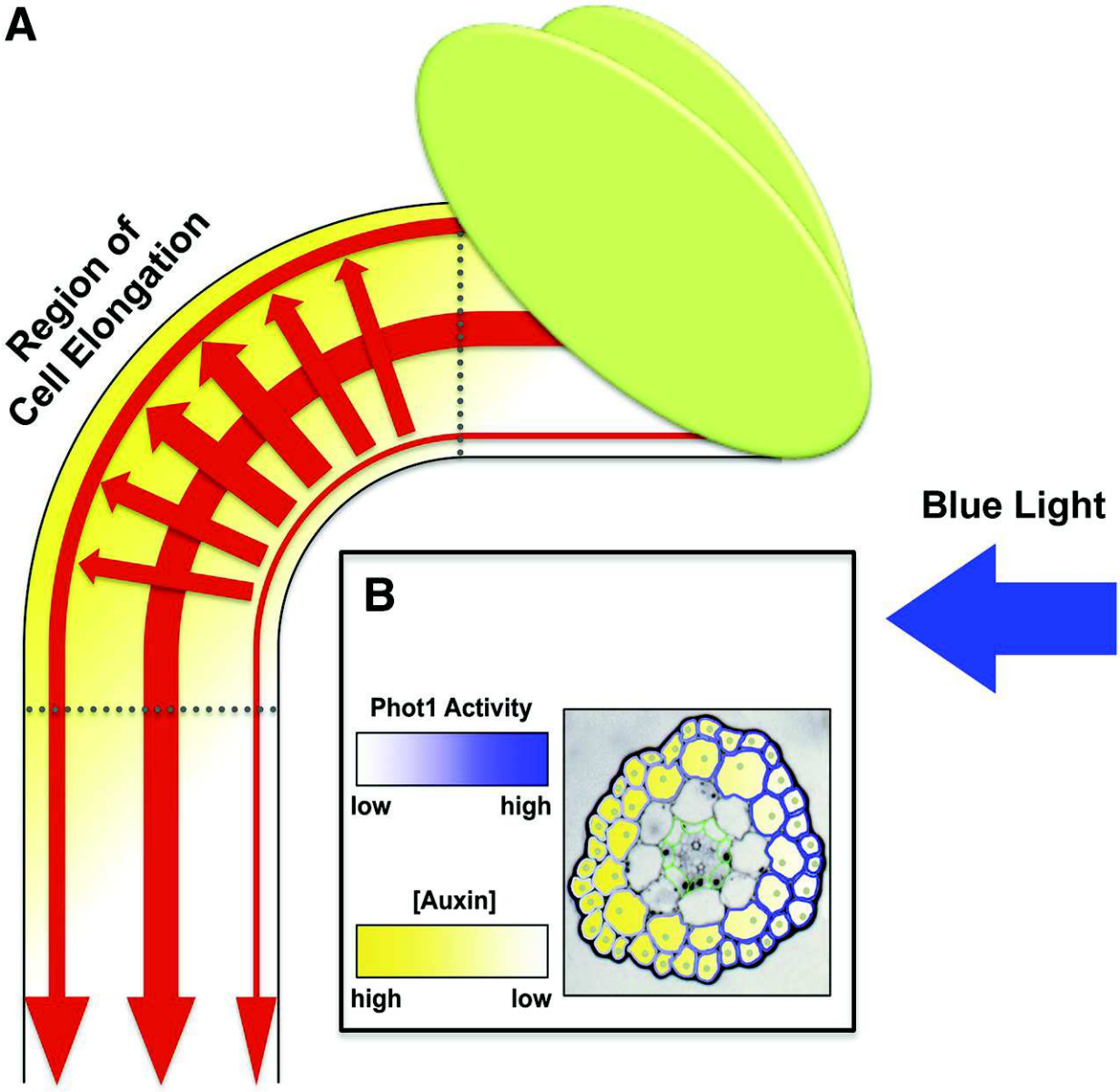

Figure 2.3: Blue light induced phototropism in higher plants requires the establishment of a differential gradient of auxin (from [53]. A)Diagram of a hypocotyl exhibiting a phototropic response. Auxin synthesized in the apical portions of the stem is polarly transported toward the root predominately through the central vasculature and to a lesser extent via epidermal and subepidermal cell layers (downward pointing red arrows). B) Cross section within the elongation zone of an Arabidopsis seedling hypocotyl illustrating the gradients of phot1 (blue light sensitive receptor) activity (false-colored white to blue) and auxin accumulation (false-colored white to yellow).

explained by the theoretical model.

Although in the case of the torus, the ZEEM resembles a rigid rotation conserving both the elastic energy and the geometry of the object, the more complex examples presented

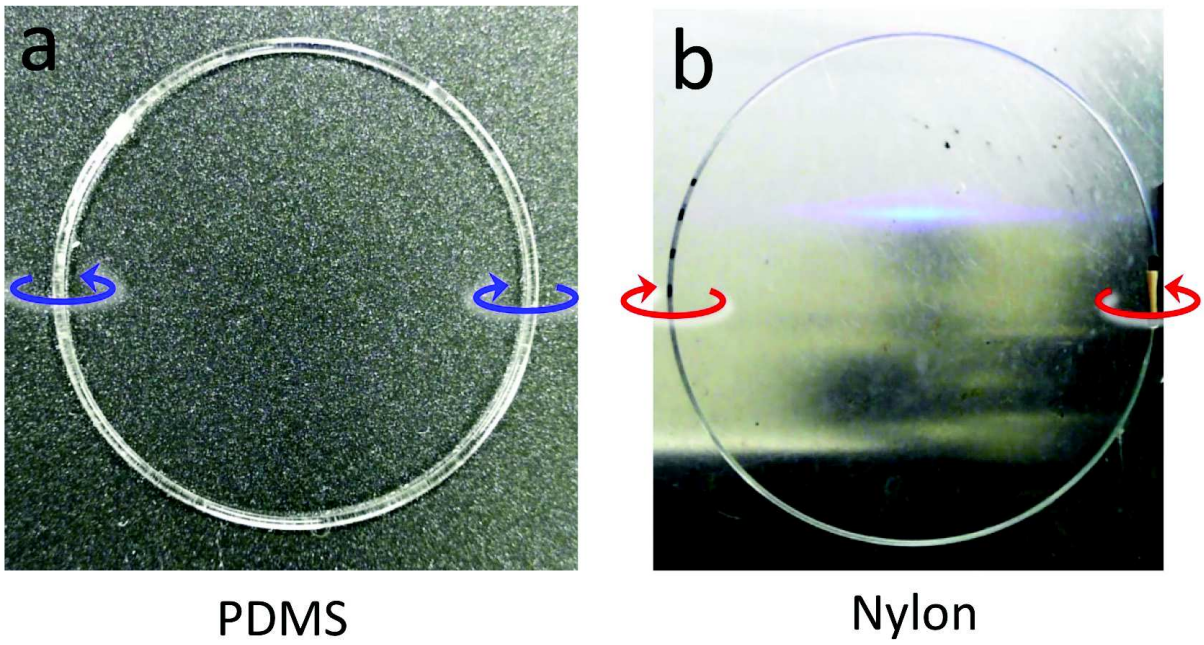

Figure 2.4: Experimental realizations of the fiberdrive with a) PDMS (radius 2cm, thickness 0.6mm) and b) Nylon (radius 6cm, thickness 0.6mm). The direction of rotation depends on the sign of the thermal expansion coefficient, positive for PDMS and negative for Nylon.

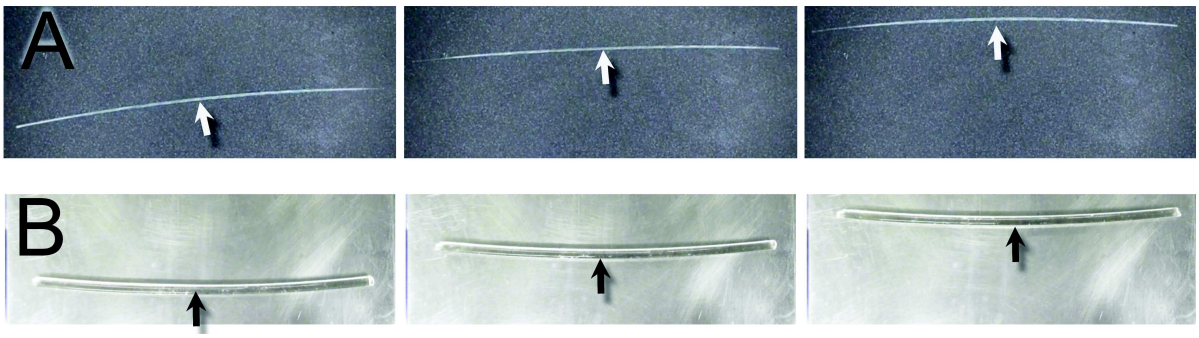

Figure 2.5: Rolling motion of a nylon-6 rod (diameter 0.6 mm, length 12 cm) (A) and a PDMS rod (diameter 3 mm, length 11 cm) (B).

above show that this is not the case. They instead form a distinct class of motion that involves continuum material deformations in the system. The striking feature of these modes is their ability to be actively driven by dissipative self-organization. A proof of concept of the phenomenon is presented in the following chapter, a toroidal polymer fiber in contact with a heat source undergoes a non-rigid rotation, performs mechanical work, stores energy and self-propels.

2.1.3 Principles of Active ZEEM Motion

Following the examples presented above, the reader should now be convinced that there are a plethora of driven ZEEMs systems in nature and that the surface has barely been scratched. This part is concerned with the necessary geometric and physical requirements to produce this type of motion in an elasto-responsive system : namely a competition between static and dynamic frustration.

In order for an elastic object to display a ZEEM different from a trivial rotation, it must bear internal prestrains that lead to a symmetry breaking. It should contain buit-in mechanical frustration, what was referred above as the static frustration. For the case of the torus discussed previously, the static frustration follows the closure into a ring. By its topology, the constraint of closure in a torus freezes static frustration into the sample in the form of the compression on the inside and the elongation on the outside. This is one of the simplest ways to introduce prestrain and symmetry breaking into an unstressed sample (the initially straight cylindrical fiber). In the same manner, introducing a half-twist into a flat sheet of material and closing it around itself to create a Möbius strip follow the same pattern. However, there are more subtle and fine-tuned methods to introduce prestrain in a material. It can be done by permanently shrinking or swelling different portions of the object, like in an edge crumpled disk [10]. The swollen perimeter forces the disk to buckle and a ZEEM emerges, the ripples can collectively slide along the edge of the disk.

The second ingredient necessary to generate active motion of the object along the ZEEM is a source of energy, or more accurately a flux of energy, to drive the system out of thermodynamical equilibrium. Although all the experiments described in this manuscript use a heat flux (from a hot surface to the cold ambient air), it can be a flux of humidity (evaporation of water or other solvents through air), ions, or even photons from a light source. When the direction of the flux with respect to the system and the response of the object to the flux meet certain symmetry conditions, continuous motion along the ZEEM is generated.

The interesting aspect about these prerequisites to motion is that depending on how the two types of frustrations emerge, two different modes of motion appear. The first one exemplified by the toroidal ZEEM (also called toroidal fiberdrive) is when the static frustration is embedded into the topology of the system. The zero-mode is present in the system before any type of external perturbation is applied to the system. The external drive generates a dynamic frustration that conflicts with the static one and thus the ZEEM is driven to overcome this conflict. In this type of systems, the motion onset occurs in a continuous fashion (starting from zero velocity) once the external drive is sufficient to overcome the prevalent dissipation mechanisms. The second mode is found in the linear samples (referred to as the linear fiberboids). There is no static frustration to start with but it co-emerges with the dynamic frustration once the energy flux is applied. In contrast with the torus, the system needs first to buckle and break the symmetry. The ZEEM emerges from a spontaneous symmetry breaking instead of being prescribed by the geometry of the sample. This can happen only after a certain threshold of driving power is applied to the sample and the onset of motion is discontinuous (starting with a finite

velocity) in this case. The major difference between these two modes of motion is that the former is a unidirectional engine, while the latter acts as a bidirectional one, that can change direction upon encountering an obstacle or a defect on the surface. The second type is easier to conceive because they don't need a geometrically prescribed ZEEM even on smaller scales. Their prestrains emerge spontaneously with the active driving force. They can even exhibit collective behaviour, see Fig. 2.12 c). However this random bi-directionality greatly diminishes their potential as motors. On the other hand, the second type demands more initial effort to create a sound ZEEM within the material but will prove to be robust engines.

In order to become active, the material has to be able to respond to an external stimulus. The stimulus can be anything from temperature, a gradient of chemical's concentration in the solution, to the intensity of light. Assuming that the stimulus is a scalar quantity T, the simplest case is when it can induce an isotropic prestrain in the material proportional to the driving field : $\epsilon_{ii} = \alpha T$ where α is the coupling coefficient and ϵ_{ij} is the elastic strain tensor. The description presented here is limited to the isotropic and linear coupling case. It is not necessary to assume isotropy of the material and its expansion or that the stimulus is a scalar quantity but these assumptions are sufficient to explain the simple cases of the toroidal fiberdrive and the linear fiberboid. An important requirement to drive ZEEMs is that the stimulus field must be out of equilibrium, meaning that it displays gradients and directional fluxes along these gradients. Taking the examples above and thinking of the stimulus as the temperature of a heating plate in room temperature, the temperature gradient will be uniform within the plane parallel to the surface and point towards the heating plate. In the case of light-sensitive materials, the gradients in the light intensity fields will appear through differential absorption of photons within the material. The side directly facing the light will get more photons while the shadowy side will get less or none at all depending on the opacity of the material.

When subjected to a stimulus gradient, different layers of the sample will respond with different strains at different depths. In effect, for a given stimulus gradient, a strain gradient in the same direction is created within the material. Given the simple case of a scalar stimulus presented above, it is then easy to see that the sign of the coupling coefficient α will determine wether the material will bend away from or towards the direction of the flux. It explains why the sign of the thermal expansion coefficient $\alpha_{\parallel}$ gives the direction of rotation for the fiberdrive or curvature for the fiberboid. However, if the topology constraints prevents simple bending deformations, deformations upon excitation by the flux can become very intricate. Thankfully, the fiberdrive and fiberboid geometries stick to the simple case of uniform bending and represent a perfect example to study both theoretically and experimentally.

2.2 Theoretical Model

By generating a mechanically frustrated dynamic steady state within the fiber's cross-section, the toroidal fiber is actively driven and the so-called fiberdrive is created. In order to do this, a thin elastic rod of circular cross-section is closed into a torus and

placed on a heating plate. As discussed previously, the topology of the torus induces a geometric strain gradient within the cross-section in the direction parallel to the surface. The inner side is compressed while the outer region is elongated, see Fig. 2.6 a). The gradient of temperature between the hot surface and the cooler ambient air (along the z-direction) creates a thermal strain gradient normal to this geometrically induced strain, see Fig. 2.6 b). From the energetic point of view, it would be preferable for the fiber to align its thermally compressed/elongated regions to those already compressed/contracted in the inner/outer circumference of the torus. The dynamic frustration necessary for an active ZEEM to emerge arises from the fact that the thermal strain gradient is externally driven, and maintained, by the thermal pumping through the hot plate. Thus a torque around the torus' axis is generated. If this driving torque is big enough to overcome the viscous dissipation within the material as well as the friction with the surface, a continuous internal rotational mode sets in and the embedded wheel starts to turn, see Fig. 2.6 c).

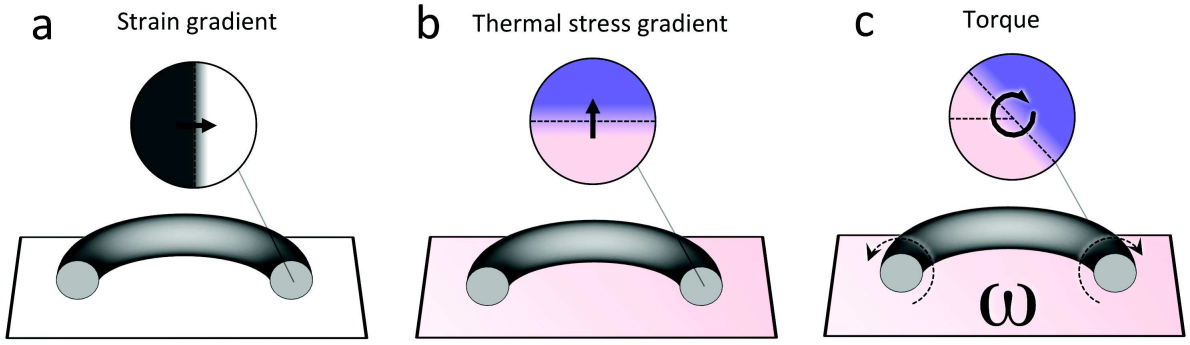

Figure 2.6: a) From its topology, the torus has a strain gradient imposed by the bending. b) When put in contact with a hot plate, the temperature gradient between the surface and the ambiant air induces a thermal prestrain in the z-direction perpendicular to the plane. c) The conflict between the geometrically imposed prestrain and the thermally driven prestrain gives rise to a dynamic instability : the torus begins to turn with a constant speed ω.

Given the rotational symmetry of the torus or the translational symmetry of a linear fiber, all that needs to be considered to describe the system is a cross-section of the material. Both systems will be equivalent from the theoretical point of view with the exception that for the torus, an external curvature is imposed on the cross-section by the geometry of the torus. In the following part, it is assumed that the fiber is confined by its own weight in the 2D plane parallel to the heating plate. This point is crucial to accurately describe the fiberboid. To start with, the creation of a torque within the cross-section by temperature gradients when a ZEEM is present is discussed. The creation of a thermally induced curvature in the case of the fiberboid is adressed and the description is completed by the balance of torques acting on the system. The motion generation is described by a general thermal diffusion equation with angular advection to compute the dynamics. These considerations give all the equations necessary to describe both the fiberdrive as well as the fiberboid and finally the case of fiber confined into a spiral pattern. The details of the calculations can be found in Appendix B.

2.2.1 Torque Creation, Torque Balance and Thermally Induced Curvature

The geometry of the sample is depicted in Fig. 2.7. The heating plate defines the X-Y plane. When considering a cross-section of the fiber, its axis can be laid along the Y-axis without any restriction considering the symmetry of the sample. The fiber's vectorial curvature is then along the X-axis (both for the torus and the linear fiber), $\vec{\kappa} = \kappa \cdot e_x$. This defines the laboratory frame.

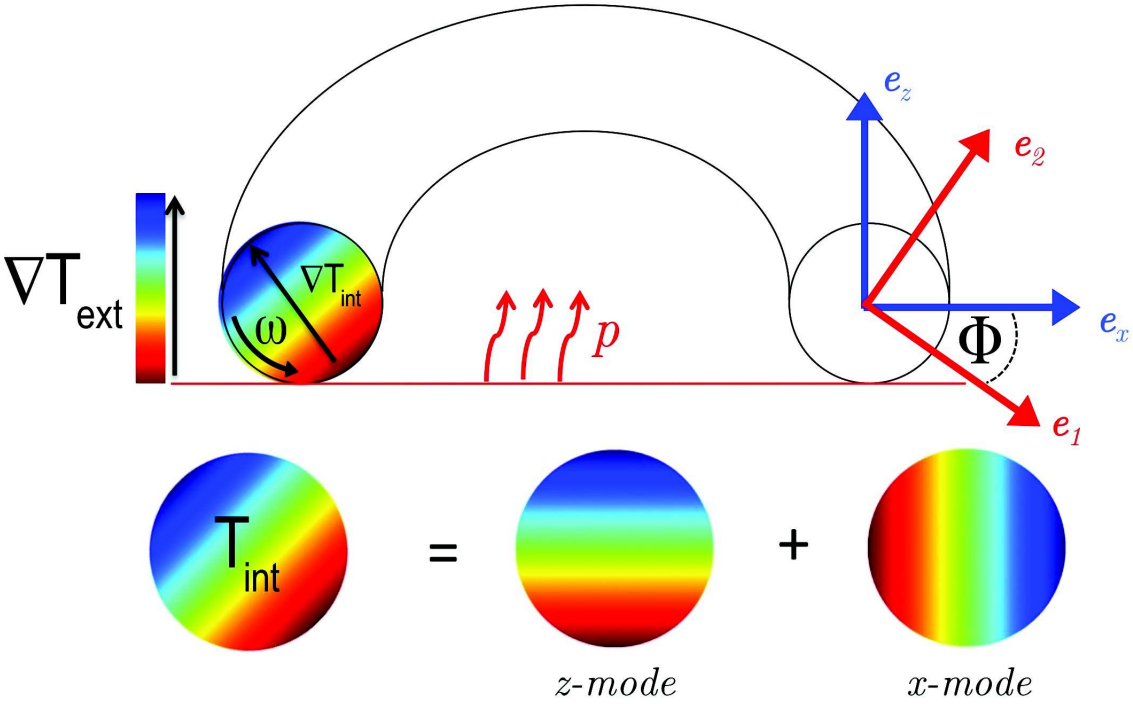

Figure 2.7: The geometry of the toroidal fiberdrive. The internal temperature profile T_{int} of each cross-section is decomposed in two modes. The thermal z-mode is pumped by the heat flux p normal to the substrate (represented by the red horizontal line). The x-mode ΔT_x emerges from the z-mode ΔT_z by frame rotation with the angle Φ.

The angle Φ, see Fig. 2.7 with respect to the X-axis describes a rotation of the cross-section around its axis and introduces the internal coordinate system, whose base is given in the laboratory frame coordinates by

$$e_1 = (cos\Phi, sin\Phi), e_2 = (-sin\Phi, cos\Phi), \tag{2.1}$$

with the internal coordinates X', Z' or (ρ, ϕ) in the polar form. In this internal frame, the total axial strain in the cross-section is

$$\epsilon_{tot}(\rho,\phi) = -\rho\kappa cos(\phi+\Phi) + \bar{\epsilon} - \epsilon_T(\rho,\phi). \tag{2.2}$$

The first contribution is due to the bending of the fiber, $\bar{\epsilon}$ is related to axial compression/elongation and ϵ_T is the thermal prestrain due to uniform axial thermal expansion/shortening. The thermal axial prestrain is given by

$$\epsilon_T(\rho,\phi) = \alpha_\parallel \Delta T(\rho,\phi), \tag{2.3}$$

with $\alpha_\parallel$ the linear thermal expansion coefficient along the fiber's axis (the coupling coefficient between the flux and the sample) and ΔT the temperature distribution within the cross-section. It can be decomposed as

$$\Delta T(\rho,\phi) = \Delta T_c \frac{\rho}{R} cos\phi + \Delta T_s \frac{\rho}{R} sin\phi + T_0, \tag{2.4}$$

where ΔT_c and ΔT_s are the two main temperature modes in the rotating frame and T_0 is a homogeneous offset. The elastic energy per unit length of the cross-section $E = \frac{Y}{2}\int \epsilon_{tot}^2 \rho d\rho d\phi$ then reads after simplification

$$E(\kappa,\phi) = B\left\{\frac{1}{2}\kappa^2 + \alpha_\parallel \frac{\kappa}{R}(\Delta T_c cos\Phi - \Delta T_s sin\Phi) + \frac{\alpha_\parallel^2}{2R^2}(\Delta T_c^2 + \Delta T_s^2)\right\}. \tag{2.5}$$

$B = \frac{\pi}{4} Y R^4$ is the bending stiffness of the material with Y the Young's modulus. The last term of (2.5) has no consequences for the dynamics of κ and Φ.

Given the explicit expression for the elastic energy of the system, the driving torque (per unit length) that is responsible for motion can be derived as $m = -\frac{\partial E}{\partial \Phi}$

$$m = B\alpha_\parallel \frac{\kappa}{R}(\Delta T_c sin\Phi + \Delta T_s cos\Phi), \tag{2.6}$$

with $\kappa = \kappa_{ext} = \frac{1}{R_{ext}}$ the externally imposed curvature of the torus (R_{ext} being the radius of the ring).

In the case of the linear fiber, (2.5) can also be used to determine the thermally induced curvature. When the open filament is first placed onto the hot plate, it initially bends out of plane until collapsing back in the XY-plane due to its own weight. During this process, the fiber acquires a curvature that is conserved during subsequent motion. This stationary curvature κ_s enters the expression of the driving torque in 2.6 in place of κ_{ext} when considering the case of the fiberboid. It can be obtained by minimizing the elastic energy with respect to κ, $0 = -\frac{\partial E}{\partial \kappa}$,

$$\kappa_s = -\frac{\alpha_\parallel}{R}(\Delta T_c cos\Phi - \Delta T_s sin\Phi). \tag{2.7}$$

These equations can be simplified further by transforming them back to the laboratory frame. Starting by identifying the two temperature modes $\Delta T_x = \Delta T_c cos\Phi - \Delta T_s sin\Phi$ and $\Delta T_z = \Delta T_c sin\Phi + \Delta T_s cos\Phi$ (see Fig. 2.7) and introducing the main thermal strain differences

$$x = \alpha_{\parallel} \Delta T_x, \text{ and } z = \alpha_{\parallel} \Delta T_z, \tag{2.8}$$

the driving torque per length and the stationary thermally-induced curvature finally read

$$m = B \frac{\kappa}{R} \alpha_{\parallel} \Delta T_z = \frac{\pi}{4} Y R^3 \kappa z, \tag{2.9}$$

$$\kappa_s = -\frac{\alpha_{\parallel} \Delta T_x}{R} = -\frac{x}{R}. \tag{2.10}$$

The thermally-induced curvature is directly proportional to the thermal strain difference in the plane which is itself depending on the thermal expansion coefficient $\alpha_{\parallel}$. This explains why the direction of the vectorial curvature relative to the direction of motion changes for different materials, see Fig. 2.8. In a similar fashion, $\alpha_{\parallel}$ appears in the expression of the driving torque, hence the different directions of "rotation" of the fiberdrive for nylon and PDMS.

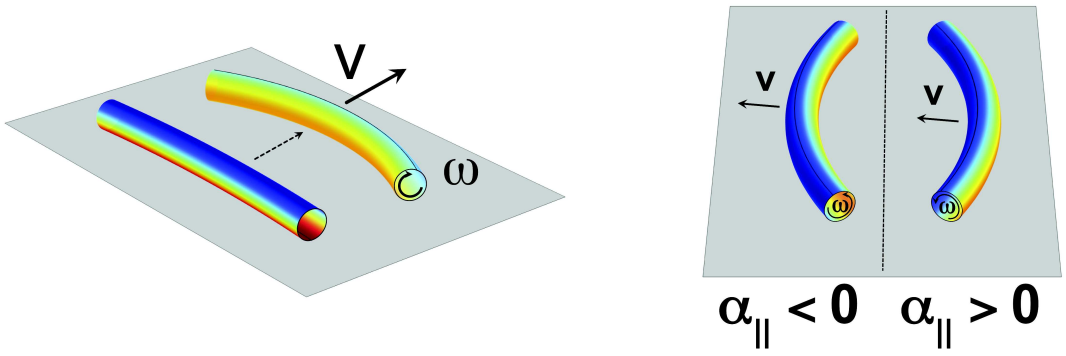

Figure 2.8: The temperature gradient between the hot plate and the ambient air bends the rod via thermal expansion or contraction. Due to the confinement (on the plate) the curving stays in-plane, which effectively creates a torque. The direction of the curvature $\boldsymbol{\kappa}$ relative to the velocity $\mathbf{V}$ depends on the sign of the thermal expansion coefficient.

To complete the description, the balance of torque acting on the system must be evaluated. On top of the driving torque derived in (2.9) and a potential external torque acting on the system, a dissipative torque must be taken into account. The two main dissipation mechanisms here are the rolling friction and the internal viscoelastic dissipation within the material. Depending on which system is considered (fiberdrive or fiberboid), one of the two mechanisms is dominant. In the case of the fiberdrive the typical strain enforced by the closure into a ring is $\epsilon \simeq \kappa_{ext} R = \frac{R}{R_{ext}} \simeq \frac{0.2mm}{2cm} = 10^{-2}$. The stress imposed by this externally imposed curvature is comparable to the loss modulus of the material E'' and

the internal viscoelastic dissipation dominates compared to the negligible rolling friction. The dissipative torque per length due to viscous internal dissipation is given by

$$m_{dissip} = E''\cdot (|\kappa_{ext}|R)R^2. \tag{2.11}$$

For the case of the fiberboid, the thermally induced curving strain from (2.8) is much smaller : $\epsilon \simeq \kappa R = x = \alpha_{\parallel}\Delta T_x \simeq 10^{-4}$. Hence dissipation in the material due to curving is negligible and rolling friction is the dominating dissipation mechanism. The dissipative torque due to rolling friction is given by

$$m_{fric} = C_r \pi R^2 \bar{\rho} g R, \tag{2.12}$$

where C_r is the coefficient of rolling friction, $\pi R^2 \bar{\rho} g$ is the gravitational normal force per length (with $\bar{\rho}$ the density and g the gravitational acceleration) and R is the lever arm. Both for the fiberdrive and the fiberboid, the dissipation is independent of angular velocity. The loss modulus E'' is independent of ω in the relevant temperature range and so is by extension the dissipative torque.

The general torque balance of the system is then

$$\frac{\pi}{4} Y R^3 \kappa_{ext} z = E''|\kappa_{ext}|R^3 - m_{ext}, \tag{2.13}$$

for the toroidal fiberdrive, and

$$\frac{\pi}{4} Y R^3 \kappa_s z = C_r \bar{\rho} g \pi R^3 - m_{ext}, \tag{2.14}$$

These equations predict that in the absence of an external torque acting on the system, the dependence on the cross-sectional radius cancels out in both cases. The main difference lies in the curvature appearing in the driving torque of 2.6), it is the externally imposed $\kappa_{ext} = \frac{1}{R_{ext}}$ for the torus and the thermally-induced κ_s for the linear fiber. This difference will play a role in the dynamics and is the origin of continuous vs discontinuous onset of motion of the motor.

2.2.2 Dynamics of the Temperature Distribution

In order to get the complete description of the system, dynamic equations for the thermal strain differences ΔT_x and ΔT_z are needed. They can be obtained via the thermal diffusion equation for the cross-section turning with constant angular frequency ω, see section B.2,

$$\partial_t T = \frac{D}{R^2}\nabla^2 T + \omega \partial_\varphi T. \tag{2.15}$$

This equation is in the laboratory frame (with (r, φ) the respective polar coordinates, with $\varphi = 0$ at the contact with the plate, i.e. φ is the angle with respect to the Z-axis)

and the length is scaled by the cross-section radius R (hence $r \in [0,1]$). D is the thermal diffusivity of the material and is given by the ratio of the thermal conductivity over the specific heat per unit volume, $D = \frac{k_{pol}}{C_{pol}}$. (2.15) has to be considered with the following boundary condition :

$$\frac{l(\varphi)}{R}\partial_r T + (T - T_{ext}(\varphi)) = 0 \text{ at } r = 1, \tag{2.16}$$

where $l(\varphi)$ is a thermal length scale, given by the ratio of the thermal conductivity of the material and the heat transfer coefficient, and $T_{ext}(\varphi)$ is the externally imposed temperature. Writing this boundary condition, perfect thermal contact is assumed at the surface of the heating plate and hence $T_{ext} = T_s$ and $l(\varphi = 0) = 0$. At the top of the cylinder at the contact with the air, heat transfer to a fluid has to be taken into account and the estimation for the present system gives $l_{th} \simeq R$.

Solving the thermal diffusion equation for the main two modes ΔT_x and ΔT_z (which are sufficient to capture the main physics of the problem) and reintroducing the thermal strain gradients from (2.8) gives

$$\dot{x} = -\frac{x}{\tau} - \omega z, \tag{2.17}$$

$$\dot{z} = p - \frac{z}{\tau} + \omega x. \tag{2.18}$$

τ is the characteristic time scale of the thermal relaxation, see eq. B.42. These two equations depict a dynamic interplay between x and z. In addition, the thermal strain gradient z is driven by the thermal drive $p = \alpha_{\|} q$ with q the pumping rate, see eq. B.43. In the case of $\omega = 0$, the solution in the long time limit gives $\Delta T_x = 0$ and $\Delta T_z = \frac{\Delta T_{ext}}{2\left(\frac{l_{th}}{R}+2\right)}$ which one would expect in the static case.

Equations (2.17) and (2.18) together with (2.13) for the fiberdrive and (2.14) for the fiberboid completely determine the dynamics of the system.

2.2.3 Onset of Motion

Fiber Closed to a Circle (the Fiberdrive)

In order to find the onset of motion, the following steady-state equations need to be solved

$$\frac{\pi}{4} Y R^3 \frac{z}{R_{ext}} = m_{dissip}(\omega) - m_{ext}, \tag{2.19}$$

$$0 = -\frac{x}{\tau} + \omega z, \tag{2.20}$$

$$0 = p - \frac{z}{\tau} + \omega x, \tag{2.21}$$

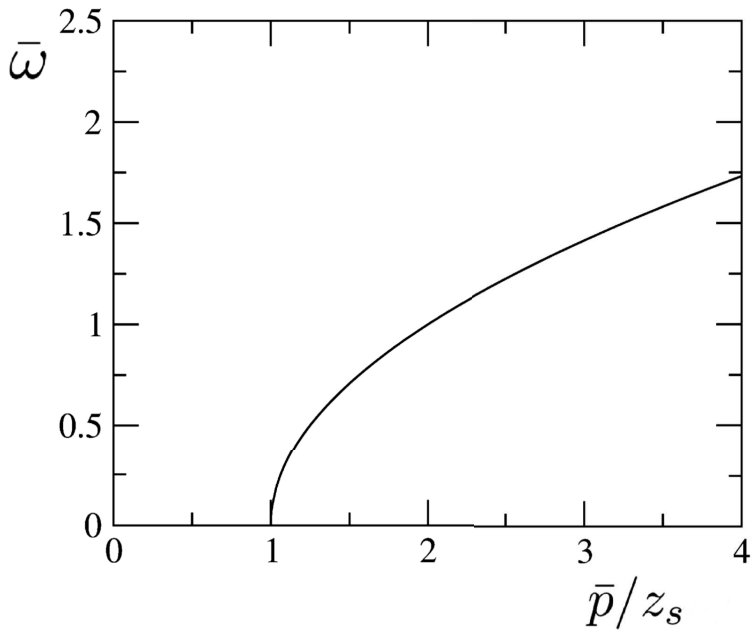

Figure 2.9: Continuous onset of rotation of a fiver closed to a ring as given by (2.22). Shown is the scaled angular velocity, $\bar{\omega}$, as a function of the rescaled effective driving $\frac{\bar{p}}{z_s}$.

where the externally imposed curvature $\kappa_{ext} = \frac{1}{R_{ext}}$ is inserted and the dissipative torque is given by $m_{dissip}(\omega = 0) = 0$ and $m_{dissip}(\omega \neq 0) = \frac{E'' R^3}{R_{ext}}$ for internal viscoelastic dissipation. The nontrivial solution for ω is given by

$$\bar{\omega} = \sqrt{\frac{\bar{p}}{z_s} - 1} = \sqrt{\frac{\pi}{4}\frac{E'}{E''}\bar{p} - 1}, \tag{2.22}$$

where the frequency and the thermal pumping are scaled by the thermal relaxation time, $\bar{\omega} = \omega\tau$ and $\bar{p} = p\tau$. This set of solutions for ω exists when the argument of the square root becomes positive, i.e. for

$$\bar{p} > \bar{p}_c = z_s = \frac{4}{\pi}\frac{E''}{E'}, \tag{2.23}$$

Above the critical value $\bar{p}_c$, an angular velocity ω sets in starting from zero, the onset of motion is continuous, see Fig. 2.9.

By solving for m_{ext} in (2.19), (2.20) and (2.21), the torque-velocity relation for a toroidal fiberdrive can be obtained and reads

$$m_{ext} = \frac{\pi}{4} Y \frac{R^3}{R_{ext}} \left(z_s - \frac{\bar{p}}{1 + \bar{\omega}^2} \right). \tag{2.24}$$

The torque is proportional to the imposed curvature $m_{ext} \propto \kappa_{ext} = \frac{1}{R_{ext}}$, which hence also holds for the stalling torque (the torque at the onset of motion when $\omega = 0$).

Using a mechanical holder (cf. Fig. 2.10), it is possible to confine the path of the fiber into a spiral. It has many advantages that will be discussed in further details in chapter 3. For this special case, the description is conceptually the same as for the closed circle, except that the imposed curvature varies along the arc length ($\kappa_{ext}(s) = \frac{1}{R_{ext}(s)}$), which makes a closed description difficult. For the spirals investigated in this thesis, the curvature does not vary much so a superposition of closed rings is used to describe the system in first approximation, using the mean curvature of the spiral.

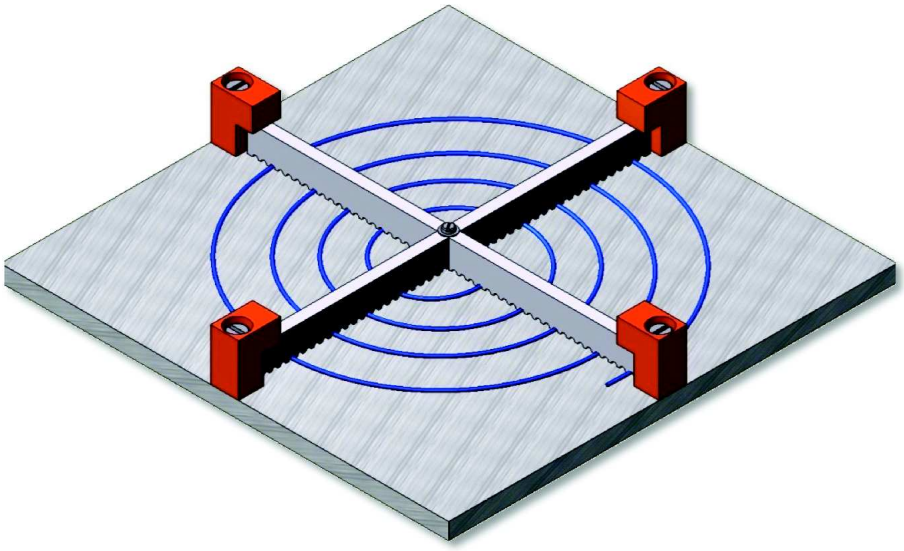

Figure 2.10: By constraining the fiber in place with a holder, a spiral can be created. It can be thermally driven to produce rotation using the same principle as for the fiberdrive.

Straight Fiber, the Fiberboid

For the case of the fiberboid, the same thinking process is applied, one has to look for nontrivial solutions to the steady-state equations

$$-bxz = m_{fric}(\omega) - m_{ext}, \tag{2.25}$$

$$0 = -\frac{x}{\tau} - \omega z, \tag{2.26}$$

$$0 = p - \frac{z}{\tau} + \omega x. \tag{2.27}$$

where the thermally induced curvature $\kappa_s = -\frac{x}{R}$ is inserted, $b = \frac{B}{R^2} = \frac{\pi}{4} Y R^2$ and the dissipative torque is given by $m_{fric}(\omega = 0) = 0$ and $m_{fric}(\omega \neq 0) = c = C_r \pi R^3 \bar{\rho} g$ for rolling friction. Nontrivial solutions for ω exist if

$$\bar{\omega}^2 - \sqrt{\frac{b}{c}} \bar{p} \sqrt{\bar{\omega}} + 1 = 0, \tag{2.28}$$

where the frequency and the thermal pumping are again scaled by the thermal relaxation time scale, $\bar{\omega} = \omega\tau$ and $\bar{p} = p\tau$. For sufficiently large drive (precisely for $\bar{p} > \bar{p}_c = \frac{4}{3}3^{\frac{1}{4}}\sqrt{\frac{c}{b}}$), a stable branch of finite ω-solution emerges, see Fig. 2.11. The frequency at threshold $\omega_c = \frac{1}{\sqrt{3}}$ is finite and hence the onset of motion is discontinuous for the fiberboid. The difference in the onset of motion for the fiberdrive and the fiberboid (continuous vs discontinuous) comes from the symmetry breaking in the system. It is imposed by the topology in the former case while it is achieved by transient thermal curving in the latter.

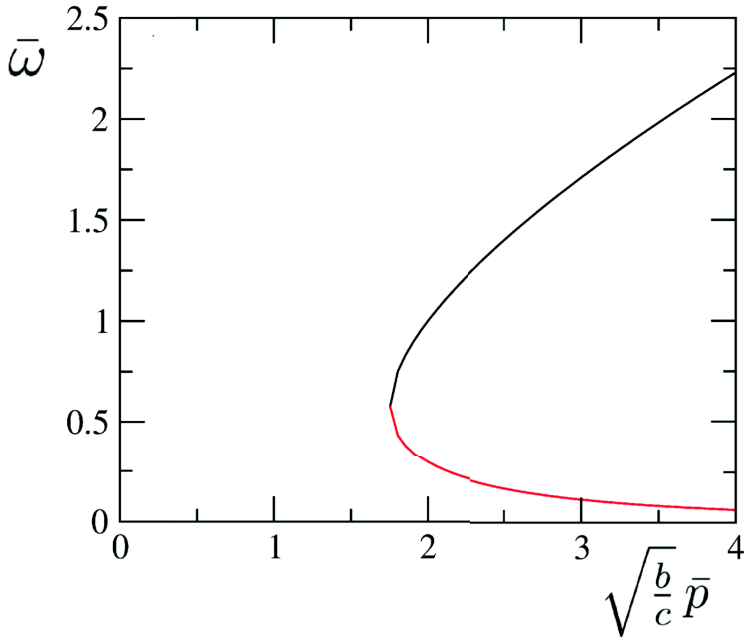

Figure 2.11: Discontinuous onset of rolling motion for a straight fiber given by solving (2.28). Shown is the scaled angular velocity, $\bar{\omega}$, as a function of the rescaled effective driving, $\sqrt{\frac{b}{c}}\bar{p}$. The black branch is stable, the red one unstable.

To conclude the description of the fiberboid, the torque-velocity relation can be obtained by solving equations (2.25) to (2.27) for the external torque to get

$$m_{ext} = c - b\bar{p}^2\frac{\bar{\omega}}{(1+\bar{\omega}^2)^2}. \tag{2.29}$$

2.2.4 Energy Storage in Spirals

To describe the experimentally studied spirals of chapter 3 in the scope of this theoretical model, their mean curvature $\langle\kappa_{ext}\rangle \simeq \frac{1}{\langle R_{ext}\rangle}$ is used. The angular velocity for free turning is given by (2.22) as $\omega_{fr} = \omega(m_{ext} = 0) = \frac{1}{\tau}\sqrt{\frac{\bar{p}}{z_s} - 1}$ and for the stalling torque, m_s, one gets from the torque-velocity relation (2.24),

$$m_s = m_{ext}(\omega = 0) = \frac{\pi}{4}Y\frac{R^3}{\langle R_{ext}\rangle}(z_s - \bar{p}) \propto \langle\kappa_{ext}\rangle. \tag{2.30}$$

This immediately gives the scaling for large thermal driving $\bar{p} \gg z_s$

$$m_s \simeq Y R^3 \kappa_{ext} \alpha_{\parallel} \Delta T_{ext}, \tag{2.31}$$

which for the total torque along the spiral, $M_s = L m_s$, yields the one discussed in chapter 3. For simplicity, the torque-velocity relation is approximated by the straight line connecting ($\omega = 0$, $m_{ext} = -m_s$) to ($\omega = \omega_{fr}$, $m_{ext} = 0$), i.e.

$$m_{ext} = -m_s + \frac{\omega}{\omega_{fr}} m_s. \tag{2.32}$$

In the next part, the situation where the inner end of the spiral is clamped while the outer end is let free to rotate as in Fig. 3.6 is considered. In the confined spiral geometry, the thermally driven torque induces rotations along the local tangent, with the fiber accumulating twist all along the spiral path. This can be interpreted via the approximate torque-velocity relation (2.32), as an equation for the twist angle of the fiber, $\psi(s)$, with s the arc length along the spiral path. Identifying $\omega = \dot{\psi}$ and $m_{ext} = C\psi''$, where $C = \gamma B = \gamma \frac{\pi}{4} Y R^4$ is the torsional stiffness, $\gamma = \frac{1}{1+\nu}$ and ν Poisson's ratio and rewriting then leads to

$$\dot{\psi} = D_\psi \psi'' + \omega_{fr}, \tag{2.33}$$

which has the form of a diffusion equation with a source term. The effective diffusion reads $D_\psi = \frac{C\omega_r}{m_s} \propto \langle \kappa \rangle^{-1}$.

The general solution of (2.33) for the boundary conditions $\psi(0) = 0$ and $\psi'(L) = 0$ (corresponding to one fixed end and one free end, with L the length of the fiber) and the initial condition $\psi(t = 0) = 0$ is given by

$$\psi(s,t) = \frac{2\omega_r}{L D_\psi} \sum_{n=0}^{\infty} \frac{sin(k_n s)}{k_n^3} (1 - exp(-D_\psi k_n^2 t)), \tag{2.34}$$

where $k_n = \frac{(2n+1)\pi}{2L}$. The fits to the experimental data (cf. Fig. 3.7) show that a one-mode approximation, taking only the slowest mode $k_0 = \frac{\pi}{2L}$ into account,

$$\psi(s,t) = \frac{16 L^2 \omega_{fr}}{\pi^3 D_\psi} sin\left(\frac{\pi s}{2L}\right) \left(1 - exp\left(-\frac{D_\psi \pi^2}{4L^2} t\right)\right), \tag{2.35}$$

is sufficient. The number of turns is then given by

$$N(t) = \frac{\psi(L,t)}{2\pi} = \frac{8 L^2 \omega_{fr}}{\pi^4 D_\psi} \left(1 - exp\left(-\frac{D_\psi \pi^2}{4L^2} t\right)\right), \tag{2.36}$$

which is fitted to the data (cf. Fig. 3.7 insert) to get D_ψ and ω_{fr} and finally via $D_\psi = \frac{C\omega_{fr}}{m_s}$ the total stalling force $M_s = L m_s$ as displayed in Fig. 3.8.

The stored energy (cf. Fig.3.7) is calculated as

$$E = \frac{C}{2}\int_0^L (\psi')^2 ds = \frac{16CL^3\omega_{fr}^2}{\pi^4 D_\psi^2}\left(1 - exp\left(-\frac{D_\psi \pi^2}{4L^2}t\right)\right)^2. \tag{2.37}$$

In the limit of $t \to \infty$ and large thermal driving, $\bar{p} \gg z_s$, using $D_\psi = \frac{C\omega_{fr}}{m_s}$ and (2.31), one gets the scaling

$$E \simeq \frac{CL^3\omega_{fr}^2}{D_\psi^2} \simeq \frac{L^3}{YR^4}m_s^2 = Y\kappa_{ext}^2(\alpha_\parallel \Delta T_{ext})^2 R^2 L^3. \tag{2.38}$$

Dividing by the fiber volume $V \simeq R^2 L$ gives the scaling seen in chapter 3. Even though the formulas given here fit the experimental data very well, they are only approximate due to the use of the mean curvature of the spiral and the simplification of the torque-velocity relation.

2.3 Outlook

From previous examples and the theoretical model derived above, two types of new soft machines can be differentiated, the fiberdrive and the fiberboid. The distinction is not purely mathematical but touches upon the very practical utility of these designs as machines. Even when thinking of more complex materials and geometries, a soft motor driven along a ZEEM can be expected to fall into one of the two categories. On the one hand, fiberboid are extremely easy to realize and don't rely on much more than the right material and driving flux. This can be seen with Fig. 2.12. On top of the nylon, PVDF and PDMS samples studied in depth in this thesis, the effect has been observed with regular pasta and silicon rubber. The effect is less dependent on material properties, only the right geometry necessary for a ZEEM to emerge is needed. These systems are great movers but not so suited to perform mechanical work given their bidirectional nature. But collective effects (see Fig. 2.12 c) might be a key to create organized motion.

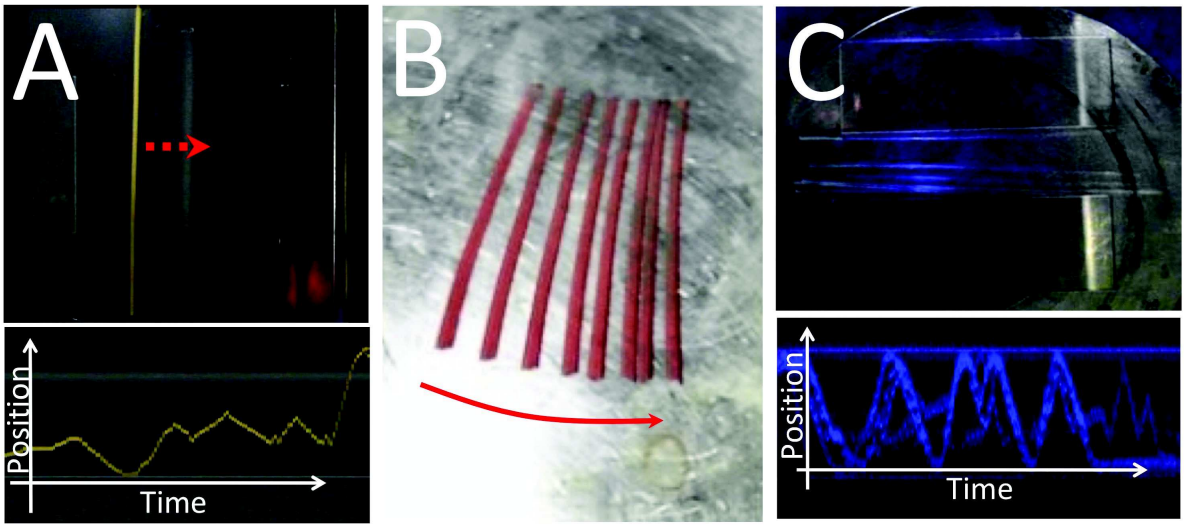

Figure 2.12: The fiberboid effect is shown to work on several types of polymers. A) Dried starch rods (spaghetti) propelled on a heating plate. The lower panel shows a kymograph (space-time plot) of the motion orthogonal to the fiber axis. B) Silicone rubber rod, superposition of images. The rolling trajectory is slightly curved due to the slight conical shape of the sample. C) Collective motion of several nylon-6 rods confined between two spacers. The lower panel again shows the kymograph.

As was explained previously, the drive need not necessarily to be thermal. Fig. 2.13 shows the first realization of fiberboids driven by evaporation. By placing spaghettis on top a wet flat sponge-like material, a gradient of water content is created within the cross-section of the pasta. It ensues that a ZEEM is developed within the material, it is then dynamically driven from the continuous evaporation of water on the top part. The effect is so far extremely poorly controlled in this crude setup. The crucial confinement onto the plate that is needed for the motion to occur is not always achieved, the water-induced bending is much greater than the thermally-induced one and the spaghettis tend to freeze out of plane. Further experiments, with better samples (possibly hydrogels) and humidity and temperature control will hopefully yield more reproducible results. However, even with this first examples, motion is observed with time scale four orders of magnitude greater than for the thermally driven fiberboids. This proves that the physical mechanism that generates motion is extremely robust and that this type of motion will surely be created with many different types of driving fluxes.

On the other hand, the fiberdrive type of motor is the closest to an actual machine with the potential to perform work. It needs more careful attention in order to design a mechanically prestrained system possessing a ZEEM from its topology. Miniaturizing fiberdrive-type motors might prove to be difficult but the example of going from the simple torus design to the the spiral showed that they can be compacted, parallelized and complexified to a degree limited only by inventivity and imagination.

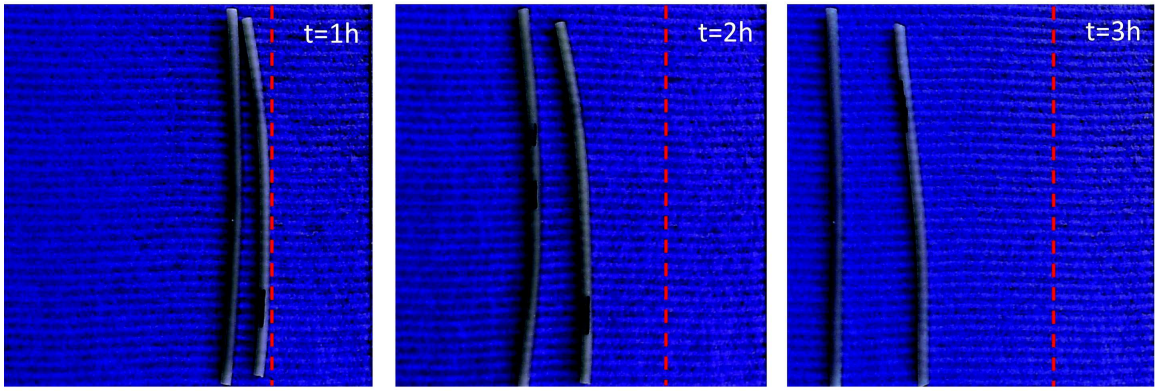

Figure 2.13: Macaroni noodles rolling on the surface of a wet sponge-like material. Pasta is a versatile tool to demonstrate the fiberboid effect. Here it is driven by an evaporation flux. The time scales are four orders of magnitude slower than for the thermal fiberboid but it is nonetheless the same physics that powers the motion.

In this chapter, the concept of motorizing soft machines with zero elastic-energy modes was explored. A new paradigm, the "embedded wheel" was described. The simple examples presented here have shown the practicality and feasibility of embedding the wheel and driving mundane polymers and materials as mono-directional or bidirectional motors. Theses fibers turn into robust motors consisting of one single piece when driven away from equilibrium by the dynamic frustration emerging within the material. ZEEMS have been shown to be truly ubiquitous in elastic materials and in nature. Generating dynamic frustration to drive them can as easy as placing a regular piece of spaghetti on a hot pan but the theory presented above hints at many other potential driving mechanism such as fluxes of solvent, ionic species, electrical or optical fluxes opening up some avenues towards vast and interesting playgrounds in the years to come. Perhaps the most complex micro machines [55] will soon be powered by this mechanism. Thinking that one can now make without the classical wheel and axle motif and instead utilize intrinsic ZEEMs to induce complex motion calls for the rethinking of the very meaning of smart materials. This effect shifts the spotlight away from finely tuned microscopic properties to the symmetry and topology of systems. Through them, the physical material acquires a novel form of collective smartness, residing in none of its individual parts, yet globally encoded in their delicate interplay.

On a last note, considering the simplicity and the robustness of such motion, it is likely that it is ubiquitous in nature and that scientific mysteries might be resolved by considering them into this light. In biological systems, there is an abundance of biofilaments confined at interfaces. The Pickering effect [56, 57] tends to confine fibers there, which is exactly one of the conditions for ZEEMs-induced motion. Considering the unusual filaments shape of filovirus such as the Marburg and Ebola virus, they might display a possible form of gradient driven surface rolling motility.

Chapter 3

A Case Study : the Heat-Driven Fiberdrive

This chapter is dedicated to the report of the first experimental demonstration of the fiberdrive and fiberboid effect. The different samples used in the experiments are briefly described before giving the details of the design of the fiberdrive. It exhibits interesting self-healing properties and can be expanded into a the spiral design of Fig. 2.10 to make it more practical. For the fiberboids, the annealing procedure is explained as well as a few interesting geometrical considerations. For both systems, the experimental results are compared to the theory presented in the previous chapter when possible.

3.1 Sample Preparation and Characterization

For the experimental demonstration of the effect, several types of polymeric materials were tested and both structurally anisotropic and semicrystalline (nylon-6 and PVDF) as well as isotropic and amorphous polymeric samples (starch, silicone rubber and PDMS) display the motile ZEEM effect. Some tests have been performed with more classical thermo-actuating materials, like a nickel-titanium (nitinol) fiber, that did not show any rotary motion. This pinpoints the importance of having low thermal conductivity in the material. If the cross-section thermalizes too quickly, the gradients of temperature cannot be established.

The most robust (and cheapest) samples are the nylon-6 fishing-line fibers (”Caperlan 4 x 4”, supplier Decathlon, France), cf. Fig. 3.1. They are gently annealed (see subsection 3.3.1) to remove built-in prestress that stemmed from their fabrication process. The annealed samples then display a very reproducible velocity-temperature dependence, cf. Fig. 3.9. Wide-angle X-ray scattering characterization of the samples (see Appendix A) shows a polymorphic order-to-order (alpha-gamma) transition within the crystalline domains as the origin of the large anisotropic thermal contraction with a negative expansion coefficient along the fiber axis of $\alpha_{\parallel} = -1.9 \cdot 10^{-4} K^{-1}$ between 120 and 180 °C.

The PDMS samples are prepared from a two-part kit that consists of liquid components (Rhodorsil RTV141 A+B (Bluestar)). The base and curing agents are mixed in a weight

ratio of ten parts base to one part curing agent, stirring the mixture to homogenize for about 2 minutes. The mixture is then placed in a vacuum chamber for 30 minutes to remove the air bubbles. The final PDMS filaments are formed in glass tubes (capillaries and glass pipettes) that are gently fragmented after the curing process, that lasts for 2h at 80°C. This PDMS rubber has a longitudinal expansion coefficient of $\alpha_{\|} = +3.3 \cdot 10^{-4} K^{-1}$.

The PDMS, PVDF and nylon rings are held together with short pieces of thermo-contracting PVDF shrink tubes or metallic brass tubes. The experimental setup for all experiments consists in a tabletop hot plate (IKA®RCT basic IKAMAG^{TM}safety control) on top of which an aluminium plate (15cmx15cmx4mm) was placed to homogenize the thermal contact. All data are acquired with a webcam (Microsoft Lifecam studio 1080p) connected to a laptop and the resulting movies are analyzed with ImageJ.

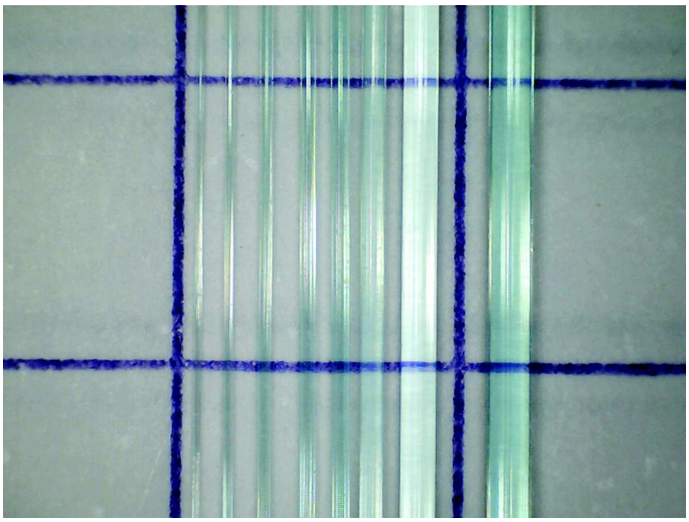

Figure 3.1: The main samples studied are fishing lines made of Nylon with diameters ranging from 0.12mm to 0.8mm.

3.2 Fiberdrive

3.2.1 The Toroidal Fiberdrive

To prepare the fiberdrives, commercially available fishing line made out of nylon-6 fibers with diameters of 0.6mm and 0.8mm are closed into rings of radii ranging from 2cm to 6cm via a small brass tube. The rings are gently annealed by raising the temperature just beyond the onset of rolling over the course of a few minutes in order to relieve mechanical prestresses entrapped during their fabrication (the extrusion process). While linear fibers are extremely delicate to anneal (see subsection 3.3.1), closed toruss display a robust and easy annealing process, probably due to their shape. The act of closing the ring makes energetically unfavorable to deform it in any other way than along the embedded ZEEM.

Compared to their linear counterpart, the rings can be more rapidly exposed to temperature greater than their onset temperature and they can be run robustly at slightly

higher temperature. While at too high temperature the (open fibers) fiberboids develop unrecoverable catastrophic deformations, a different interesting observation can be made for the rings.At elevated temperatures of 190-195°C, rings can occasionally from a localized strongly curved kink-like defect (see Fig. 3.2 at the 7s mark) that quickly reverts back to a uniform curvature from the continuous operation of the drive. The rotation of the cross-section at the site of the defect seems to smooth out and "repair" the material. Very rarely at 190-195°C rings suffer an irreversible damage that leads to a blocking of their rotation without any visible kink or obvious defect. Nevertheless, the majority of the rings stay functional and rotating for days. Once properly annealed, a ring can be subjected to high driving temperatures (up to 180 °C) without any problems even after several days of inactivity.

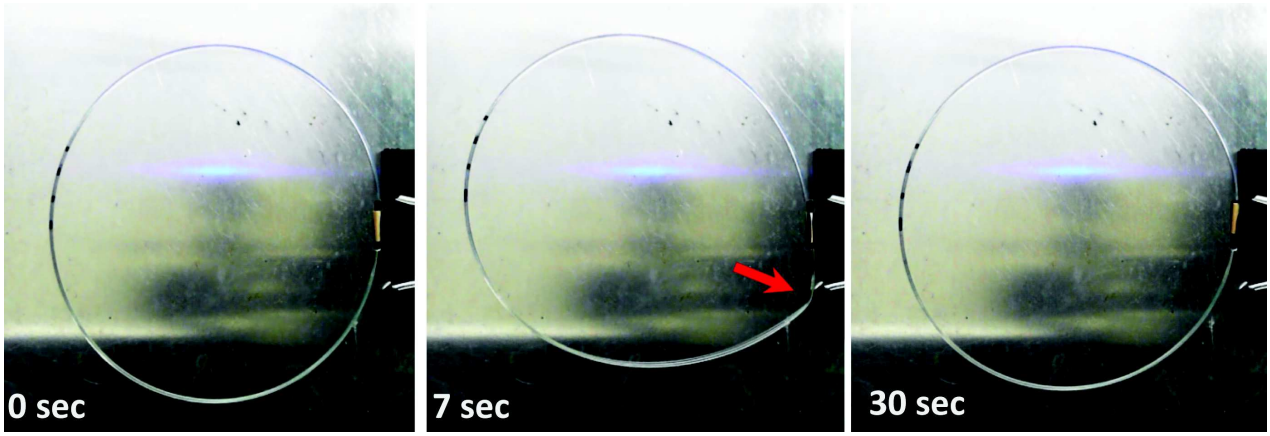

Figure 3.2: Collective spontaneous self-healing of defects in a circular fiber motor from nylon-6 rotating at 190°C. A strong deformation defect (kink) emerges at time t = 7 s and persists for several seconds. The continued collective rotation of the fiber leads to a complete self-healing at a later time (t = 30 s)

The fiber closed into a torus constitutes a unidirectional motor with its turning direction dictated by the sign of the thermal expansion coefficient. Fiberdrives constructed out of nylon-6 and PVDF turn outward while those constructed out of PDMS turn inward, cf. Fig. 2.4. A quantitative study of the angular frequency of rings of various diameter as a function of the driving temperature is summarized in Fig. 3.3. It shows that for high running temperatures, the angular velocity is almost independent of the radius of the torus (within the same order of magnitude). The data is in agreement with the theory : the onset of motion is continuous starting from zero angular velocity and the temperature (or equivalently the pumping rate) needed to start the motion goes up as the radius of the toruss goes down. With smaller rings, the imposed curvature is bigger and hence so is the dissipative torque $m_{dissip} \simeq E''|\kappa_{ext}|R^3$.

3.2.2 The Spiral Fiberdrive

The toroidal motors are elegant self-contained devices, but difficult to interconnect due to their closed geometry. This makes them poor candidates to do anything else but demon-

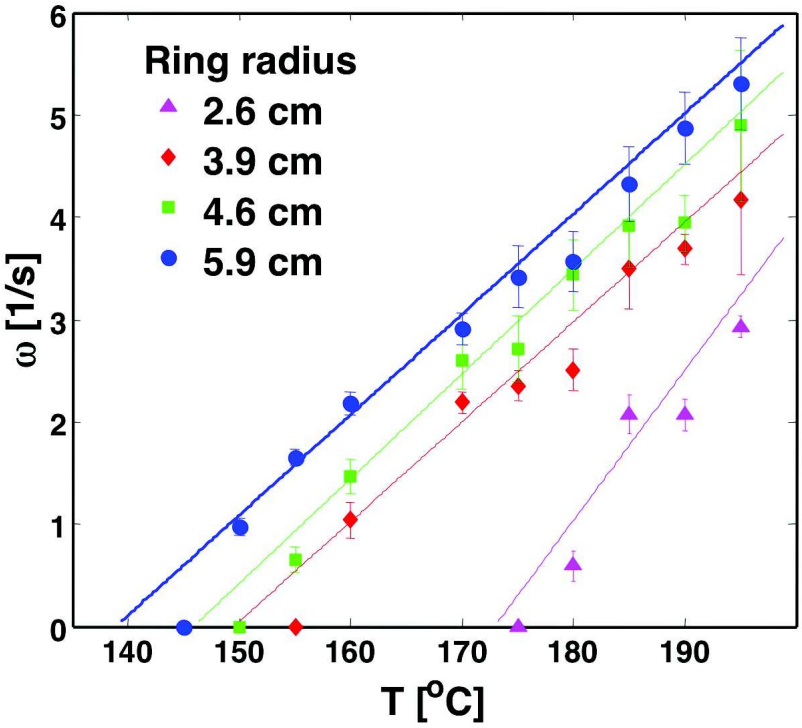

Figure 3.3: The angular frequency of various-sized nylon rings (fiber thickness 0.6 mm) as a function of plate temperature. The error bars are equal to the standard deviation of ten measurements on a ring and the lines are only guides for the eye.

strate the basic phenomenon of the fiberdrive. However, it turns out that the fiber "rotation" persists even when the curvature is externally imposed. With the use of the holding set-up depicted in Fig. 2.10, a long piece of fiber can be forced into a spiral path, an arrangement that can be seen as a parallel connection of many concentric partial toroidal motors.

Compared to the toroidal fiberdrive, spiral fiber motors (made from nylon-6) that are held in shape by the aluminum holder have to be annealed more carefully and slowly due to frictional interactions with the holder. The holder-fiber interactions leads to an occasional undesired pinning of the thermally shortening fiber onto the holder. The latter process can be prevented by a slower initial annealing cycle (gentle raising temperature in 10-15 minutes from 100-160°C) and occasional gentle stirring of the fiber (with a silicone brush) along its tangents to relieve built-up strains and to unpin it from the holder.

When tying a load to the outer end of the spiral (here a small replica of the Eiffel tower, cf Fig. 3.4, the continuous rotation of the fiber wraps the string around it and lifts it, effectively demonstrating the ability of the spiral fiberdrive to produce work. Given the geometry of the spiral, the effective torque produced is roughly the sum of each individual torques produced by the connected partial toruss. The spiral can thus exert a large torque sufficient to lift a payload more than ten times its own weight (20g for the load versus 1.5g for the whole fiber).

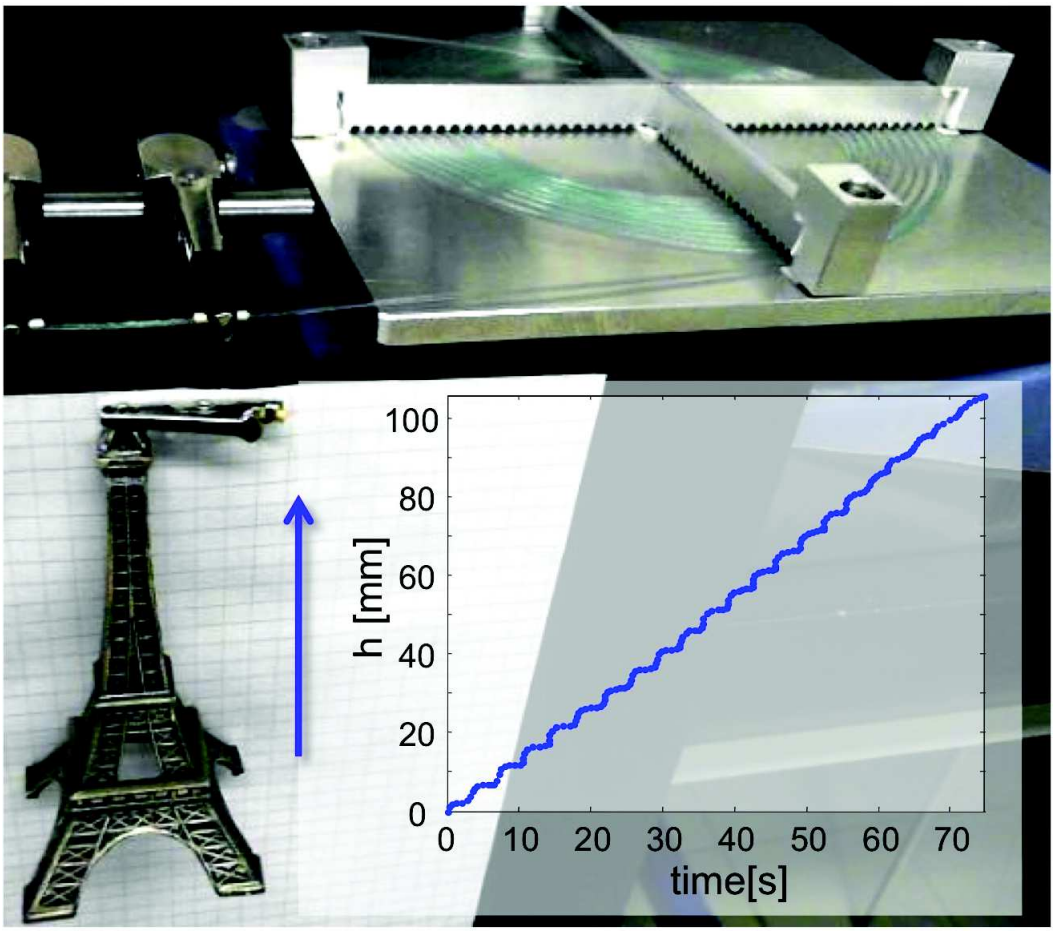

Figure 3.4: Spiral fiberdrive (fiber thickness 0.8mm, total spiral length 3.2m) realized according to the design showed in Fig. 2.10. It is rotating at 185°C lifting a payload (Eiffel Tower replica of weight 20 g). The fiber is guided from the spiral holder through two brass tubes and rotates freely there. Inset: position of the weight as it is lifted.

A long time testing, cf. Fig. 3.5, of annealed spiral motors reveals a continuous operation of the device with a gradual decay of turning speed on a timescale of tens of hours. Data have been obtained from a nylon-6 spiral (600 μm diameter, 3.2 m total length) running at an operating temperature of T = 160°C; the spiral was observed to operate continuously for 24 hours loosing approximately half of its initial angular velocity in this time period.

On top of its very robust operation and it scalability[1], one extra feature of the spiral fiberdrive is the ability to act as a storage device, an elastic battery. When rigidly stalled and prevented from rotating (by clamping one of the its free end), the fiber's free end continues to turn for several minutes and hundreds of turns before stalling cf. Fig. 3.6. This process harvest the residual thermal energy from pumping and stores it within the material itself in the form of torsional elastic energy. When the fixed end is released, this

[1]Many more spires can be added to the spirals with the right holder and one can even imagine going 3D with one continuous very long fiber and hand-designed heating devices.

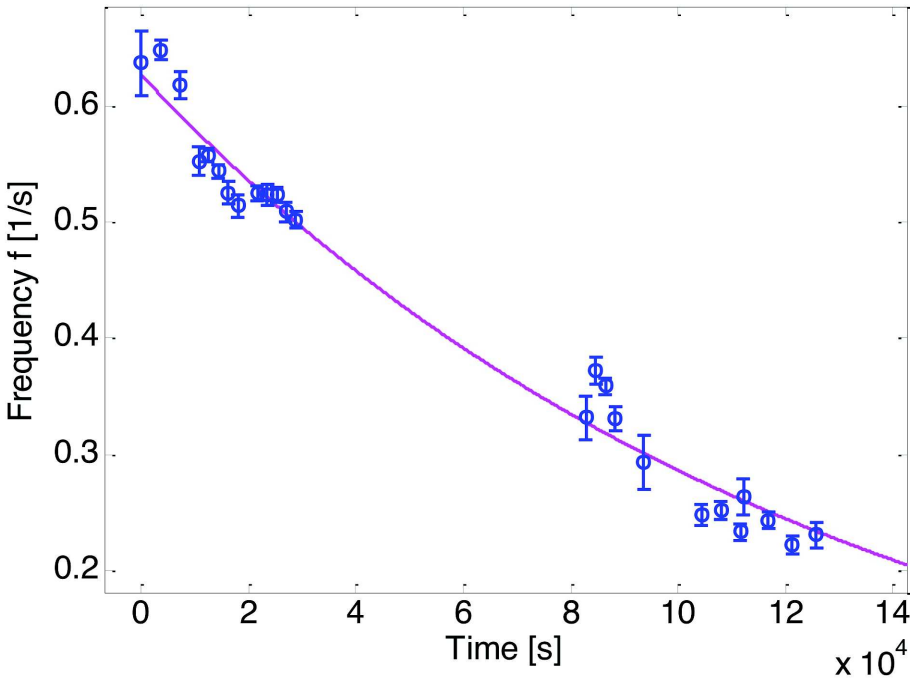

Figure 3.5: Continuous operation long time-testing of a spiral fiber motor. The fiber (nylon-6) is guided to a 13 turn, 0.6 mm diameter spiral and runs at T=160°C. The magenta line is a fit to $f(t) = f_0 exp(\frac{-t}{t_r})$, with $f_0 = 0.63$Hz and with the exponential frequency relaxation time of $t_r = 34h$ (1.28x10$^5 s$). The error bars are the standard deviations from 10 separate measurements.

stored energy can be retrieved (for instance to lift another Eiffel tower or the cathedral of Strasbourg).

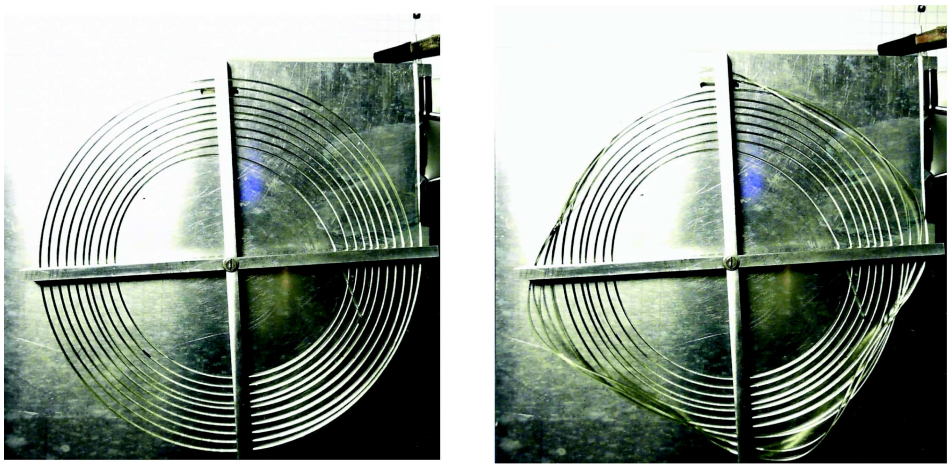

Figure 3.6: When clamping the spiral at one end, it continues to operate, storing elastic energy. The longer tests were performed until a buckling event as depicted on the right happened, the tests were stopped to prevent mechanical damage to the spirals.

The number of turns performed by the spiral torus plotted as a function of time can be measured for spirals of different length (practically by cutting a segment of the fiber

before each new measurement), see Fig. 3.7 inset, and then fitted to the dynamic solution of a torque balance model, see eq. 2.36. This allows in turn for an estimation of the stored elastic-energy within the spiral from eq. 2.37 (main panel of Fig. 3.7).

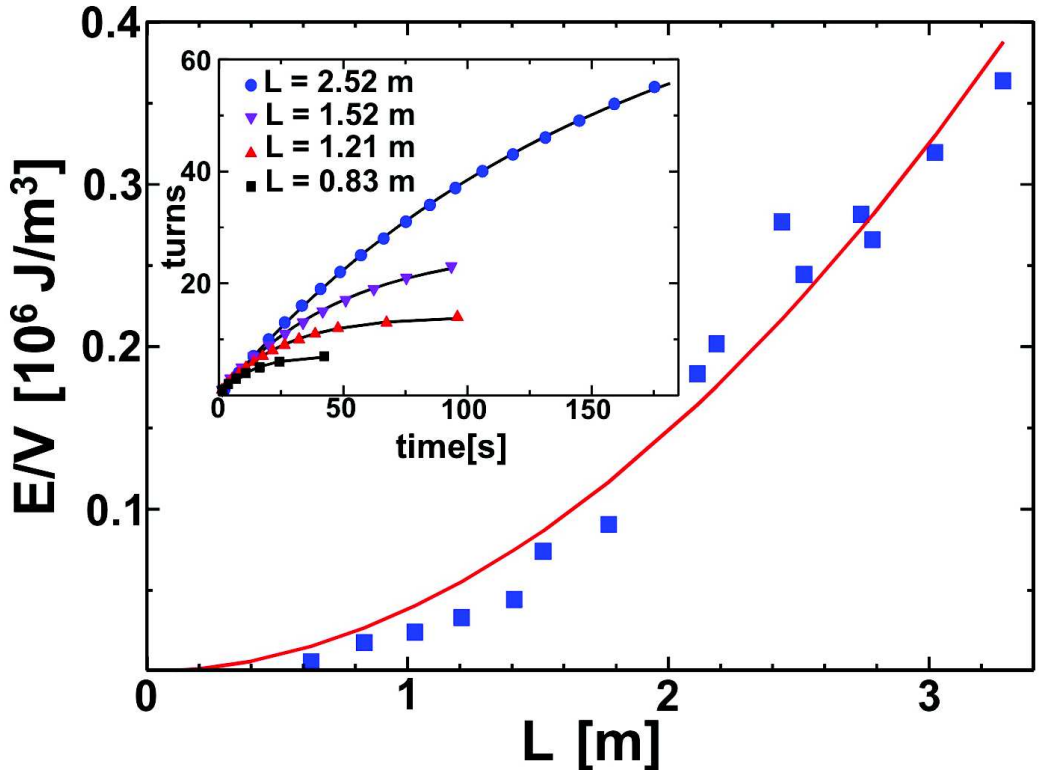

Figure 3.7: Charging of the 'spiral fiber battery'. Inset: number of turns as a function of time for spirals of various lengths that are rigidly blocked at one end. The lines are fits to the theory (subsection 2.2.4 and equation 2.36), which allows an estimate of the stored elastic-energy density, shown in the main panel as a function of spiral length. The red line is the predicted scaling with L^2.

With the thermal and elastic torques balanced, for a strong thermal pumping (see eq. (2.31)) the stalling torque scales as:

$$M_s \simeq Y R^3 \kappa \alpha_{\parallel} \Delta T_{ext} L, \tag{3.1}$$

and the stored torsional energy density of a blocked motor as :

$$\frac{E}{V} \simeq Y \kappa^2 (\alpha_{\parallel} \Delta T_{ext})^2 L^2, \tag{3.2}$$

where κ is the average curvature of the spiral, L its length, $\alpha_{\parallel}$ the linear thermal expansion coefficient, Y the Young's modulus and ΔT_{ext} the temperature gradient imposed by the heating plate. The linear increase of the torque and the quadratic increase of the

energy density with the length are signatures of the collective interplay of the spiral's gyres. The good match of the model with the experimental results (see Fig. 3.8 and 3.7) shows that the approximating the spiral by its average curvature is a viable simplification here. The rapidly growing energy-storage capacity of the device is only limited by the mechanical failure of the material or the holding device and can be greatly improved by scaling up the dimensions of the spiral fiberdrive. The efficiency of the motor can be estimated as :

$$\eta \simeq \frac{M_s \omega}{\mathring{Q}} \simeq 10^{-3}, \tag{3.3}$$

where $\mathring{Q} \simeq 2RLh\Delta T_{ext}$ is the heat current through the fiber per unit time, with h the heat transfer coefficient at the fiber-air interface, and $M_s\omega$ is the useful power output.

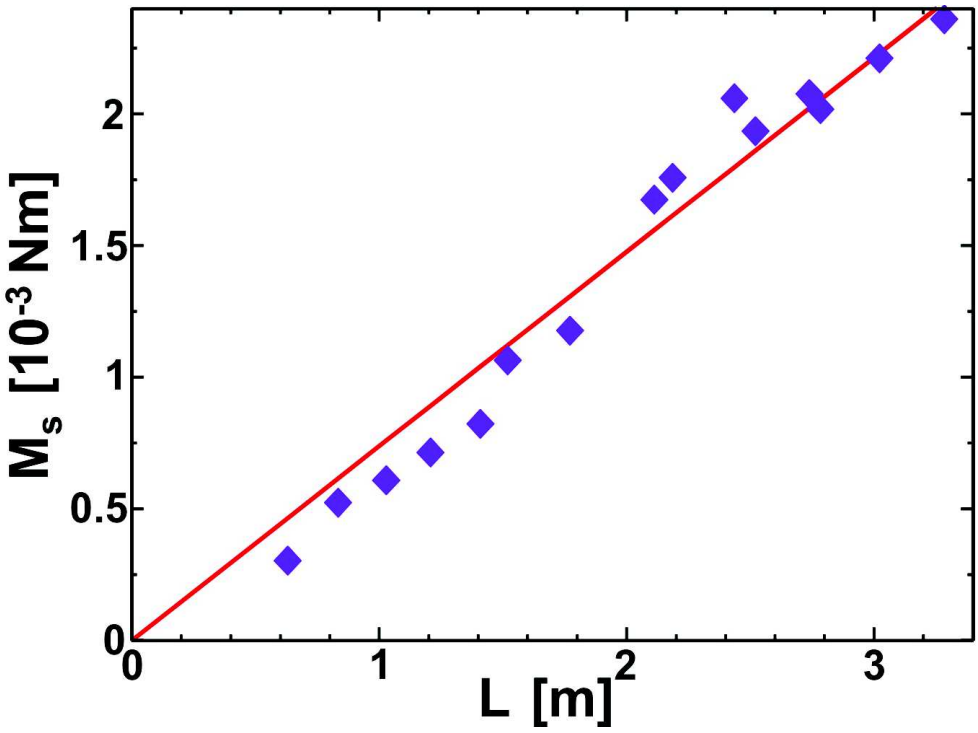

Figure 3.8: The stalling torque of the spirals studied in Fig. 3.7 as a function of spiral length, which displays a linear scaling (red line)

3.3 Fiberboids

For the toroidal fiberdrive, the ZEEM ensues from topological constraints while for the spiral fiber drive the mechanical holder maintains the shape. As discussed in chapter 2, even initially straight fibers (or spaghettis and sausages) can develop a self-organized ZEEM under the right conditions. In this section, fibers placed onto a hot substrate are shown to develop a self-propulsion in a bidirectional manner at typical speeds of centimeters per second. Sample preparation prior to running is slightly more delicate than for the fiberdrive

and the overall smoothness of the motion is very sensitive to the fiber's shape. The general behavior of the fiberboid is examined and compared to the theory for the self-induced curvature, the dependence of the rolling velocity as a function of temperature, its ability to perform work and the scaling effect of the fiber's diameter on the angular frequency ω.

3.3.1 Annealing of the Linear Fibers

Nylon-6 fibers with diameters ranging from 800 down to 120 μm are gently annealed by slowly heating the fiber on the heating plate from their onset temperature of rolling (around 100-110°C for the 600 and 800 μm diameter fiber) up to their optimal running temperatures of 180-185°C. In a typical annealing procedure, the temperature is gently raised over the course of several minutes so that the fiber gradually liberates defects and prestresses via the process of combined heating and their spontaneous rolling, cf. Fig. 3.10. All fibers that are subjected to even a single training run can in the following runs be directly exposed to the highest operation temperatures without damage and are immediately engaging in the rolling process (see Fig. 3.9). This memory effect of the first training run can be observed within a long period of up to several days after the training.

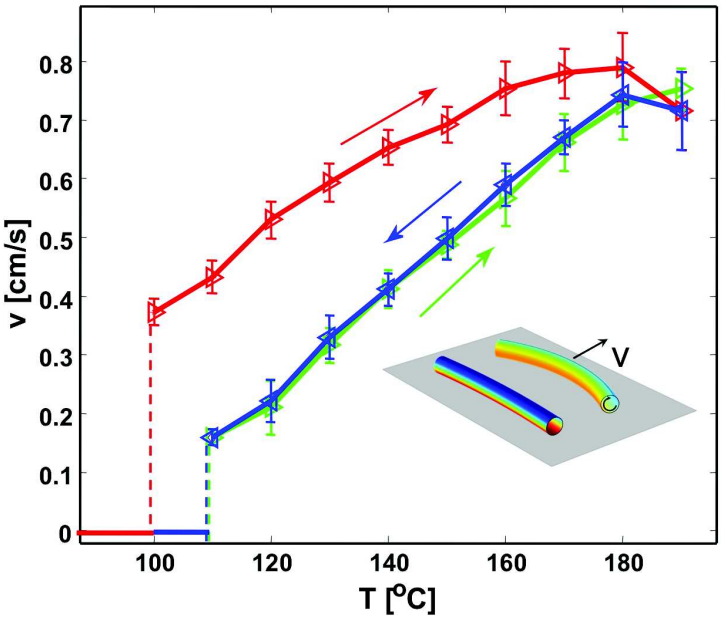

Figure 3.9: Rolling velocity (same fiber as in Fig. 3.13). During the first temperature cycle (red line), the fiber undergoes an annealing process and becomes conditioned ('trained'). In the subsequent cycles of decreasing/increasing temperature, the fiber attains a reproducible velocity (blue/green curves). The error bar are calculated from the standard deviation of three different specimen.

Skipping the first gradual training run and instead directly exposing the fibers to temperatures higher than their onset temperature (of 140°C-180°C) results in a rapid reshaping of the fiber and catastrophic deformations, see Fig. 3.11, despite the fact that the process

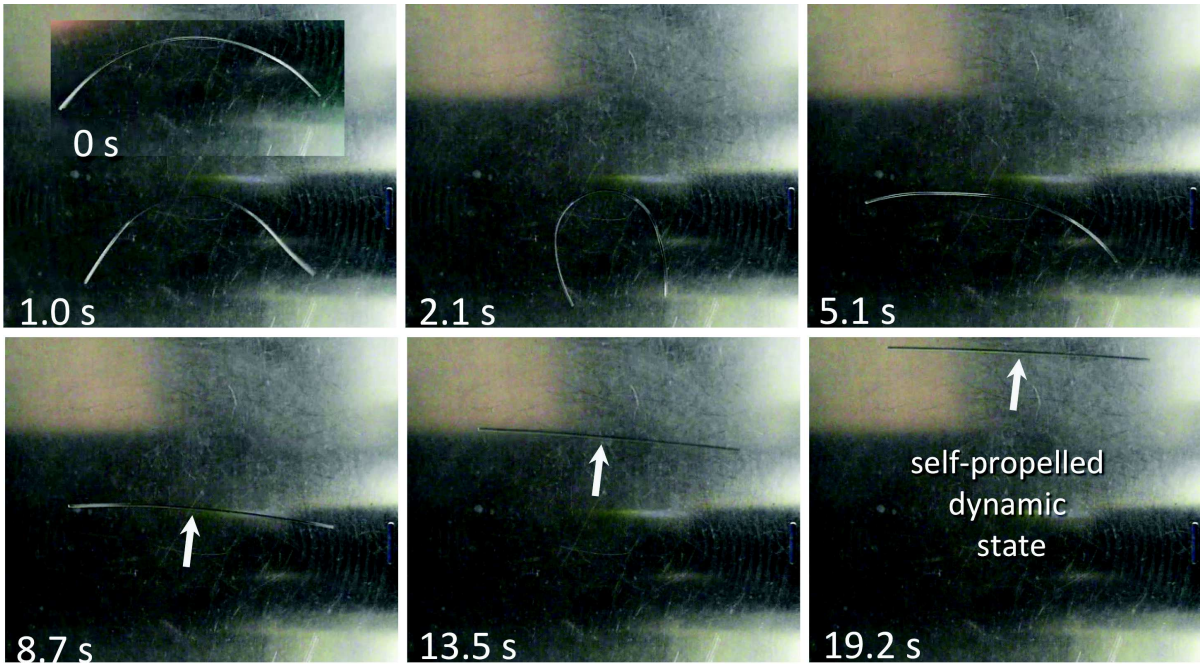

Figure 3.10: Slow annealing of a 800 μm nylon fiber at 110°C results in some transient reshaping and eventually within the time course of 10-20 seconds leads to an ideally straight and rolling fiber.

happens far below the melting temperature (T_{melt} = 215°C). This uncontrolled exposure process leads in most cases to very poorly mobile or completely immobile fibers. The final torturously deformed irregular fiber shape is irreversible and can not be reverted even up to the point of fiber melting. These tests underline the importance of a first gentle training run for reproducible rotation of linear, open fibers.

The annealing of thinner nylon-6 fibers, below 0.2 mm in radius, becomes increasingly delicate and structural defects (like bends, kinks and twisted helical sections) appear more often. Consequently, a reproducible annealing process of thinner samples requires a slower annealing procedure in comparison to thicker fibers. For consistency reasons, all nylon-6 fibers used for angular velocity measurements are annealed according to the same minimal protocol : Starting from 100°C, the temperature is raised to 160°C at a heating rate of 15 K/min followed by a gentler increase from 160°C to the highest temperature of 185°C at 7 K/min. Following this protocol leads to close to 100% functional fiber motor samples for all probed thicknesses.

For the PVDF fiber samples (”Phen-X-Fluorocarbone” fishing line fibers, supplier Decathlon, France; diameter 0.5 mm) the annealing is more delicate than for nylon-6. A modified annealing protocol respecting the lower PVDF melting temperature (T_{melt} = 177°C) is followed, with a temperature rise from 130°C up to 170°C at a slower heating rate of 1 K/min. After annealing PVDF fibers move with velocities comparable to their nylon-6 counterparts, (see Fig. 3.14 in comparison to Fig. 3.9). The PDMS fiber samples prepared in the way described in the materials section and do not need any annealing, probably

because their preparation process involves curing them at relatively high temperature for some time.

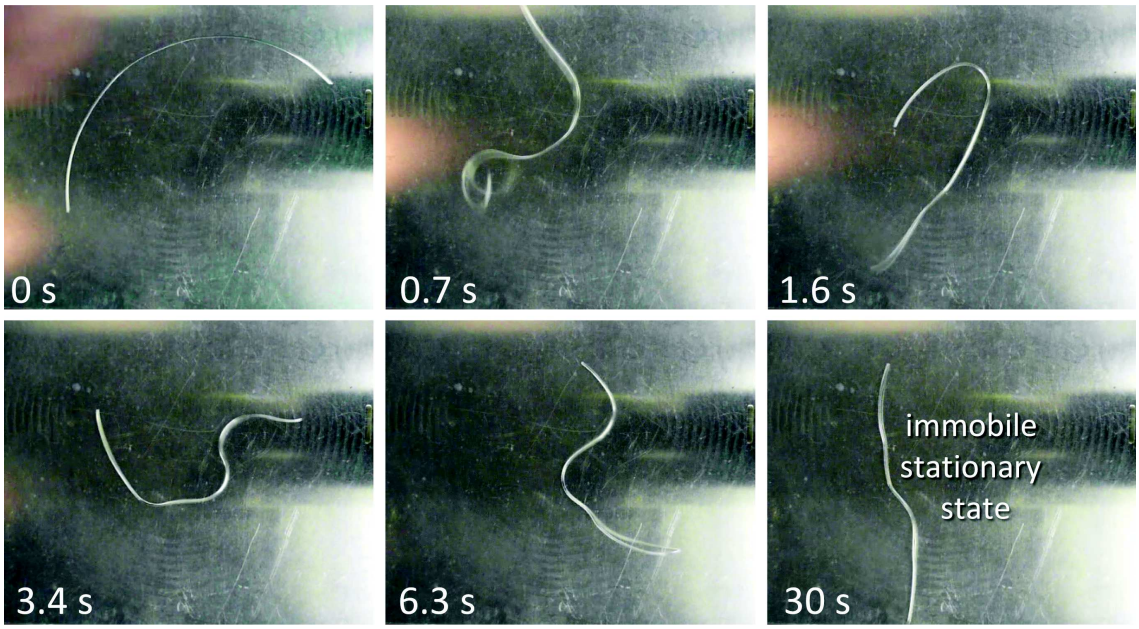

Figure 3.11: Exposing a nylon fiber (800 μm) directly to an elevated temperature (180°C) results in rapid uncontrolled reshaping. The final shape remains stationary and does not move or roll over the surface.

The total length of the fiber plays a certain role in their ability to roll smoothly and reproducibly. Occasionally, at temperature very close to the onset of rolling motion, shorter samples of PVDF and nylon-6 fibers (5 cm in length and below) become stuck in a metastable out-of plane deformation. They stay suspended above the surface with only two points of contact (their two ends) with the plate for a few seconds. The motion is then intermittent and prone to more frequent direction reversal. Although the pumping is in principle sufficient to drive the fibers, the fibers are not confined in the plane by gravity in this case. This behavior is never observed for the PDMS samples since their positive thermal expansion coefficient makes it so that only one point of contact with the plane remain upon deformation. This effect is also observed when attempting to run water-driven fiberboids (see Fig. 2.13) where the samples are much softer and the substrate is rougher. To avoid this problem with the thermal fiberboids, only heavier samples (ie. longer fibers $>$ 8 cm in length) are used. They run smoothly and permit the quantitative measurements.

3.3.2 Linear and Angular Velocities

Linear velocities are measured by tracing the fibers'positions from time-lapse and high speed recordings (for the thinnest diameters). The angular velocities are extracted by tracing color marks painted on fibers from high speed recordings of the rolling process on a Phantom MIRO LC 320S camera, at 300 frames per second.

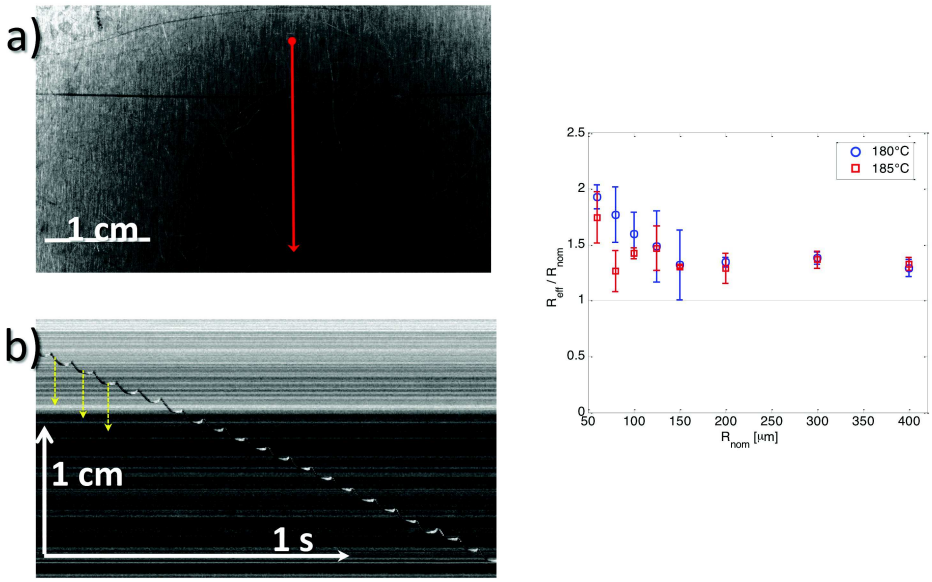

Figure 3.12: Measurement of linear and angular velocity. a) A nylon-6 fiber of radius 60 μm rolling at 185°C. b) Kymograph of the motion along the red line in a). In addition to a constant velocity linear motion, the fiber displays a velocity modulation (yellow arrows) in phase with its rotary motion. On the right, the effective radius of the fiber is shown, deduced from the ratio of linear and angular velocity.

The comparison of the linear and angular velocities of single fibers with a given radius R reveals measurable differences between the expected angular velocities $\omega_e = \frac{v}{R}$ and the directly measured ω_m with ω_m being consistently smaller than ω_e. This effect is especially pronounced for very thin fibers with the ratio $\frac{\omega_e}{\omega_m}$ approaching 2 for the thinnest samples. The discrepancy is resolved by carefully observing the dynamical shape evolution of the fibers. During the rolling process, the fibers seem to slightly but visibly fluctuate in shape in a periodic manner. This observation together with $\frac{\omega_e}{\omega_m}$ being different from unity implies that the fiber shape is slightly deviating from ideal and displays small amplitude, large wavelength bends. When rotating the bend defects give rise to an increase of the effective fiber diameter beyond the nominal fiber thickness. The ratio between the nominal and effective radius of fibers of different thickness is depicted in Fig. 3.12.

3.3.3 Thermally-Induced Curvature

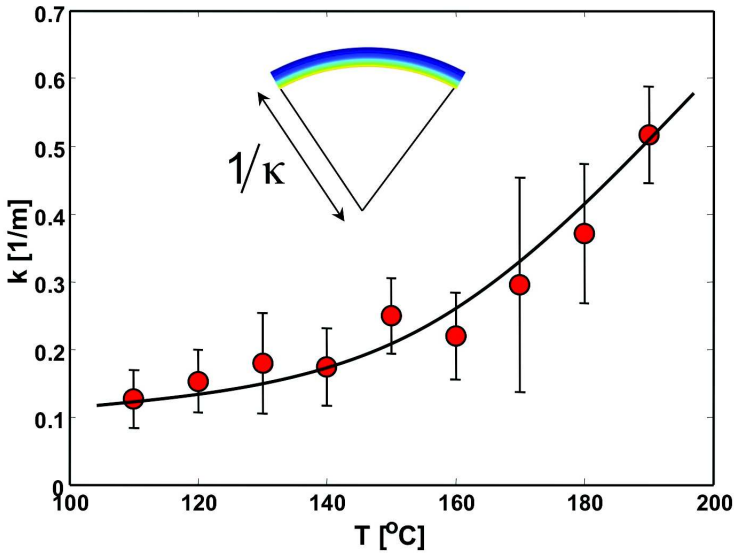

Figure 3.13: Thermally induced curvature as a function of temperature for a nylon-6 fiber of radius 0.3 mm. The errors bars are calculated from the standard deviation of three different specimen.

The motion of the fiberboid is governed by the same principle as for the fiberdrive. A ZEEM is actively driven by the thermal flux from the hot plate. The difference is that for the fiberboid, the ZEEM is self-organized within the first second after the fiber is placed on the surface. The fiber bends out of plane before collapsing back onto the surface by its own weight. The thermally-induced curvature $\kappa = \frac{x}{R}$ given by equation (2.10) comes from the rotational advection of the fiber. Fig. 3.13 shows experimental measures of the thermally induced curvature as a function of the temperature for a 0.3mm diameter nylon-6 fiber. The theoretical model matches the data. At the onset of motion, one of the possible in-plane curving directions is randomly chosen and the fibers are visibly curved during the motion (cf. Fig. 2.5). Fibers with a negative thermal expansion coefficient (nylon-6, PVDF) move in their opposite direction from their centre of curvature, whereas those with a positive thermal expansion (PDMS) move towards it.

3.3.4 Dynamics of the Fiberboids

Figures 3.9 and 3.14 represent measurements of the rolling velocity of nylon-6 and PVDF fiberboids as a function of temperature. Despite being made out of different materials, the general behavior of the system is similar. As opposed to the toroidal fiberdrive, the onset of motion of the fibers is discontinuous, setting-in with a finite velocity. The initial angular velocity ω_c depends on material properties and geometry ($\omega_c(R, k_{pol}, c_{pol})$, with k_{pol} the thermal conductivity and c_{pol} the specific heat per volume) and is hence different in both cases. The discontinuity can be understood by the fact that contrary to the fiberdrive, the symmetry breaking inducing the ZEEM is self-organized for the fiberboid. Fig. 3.9 also

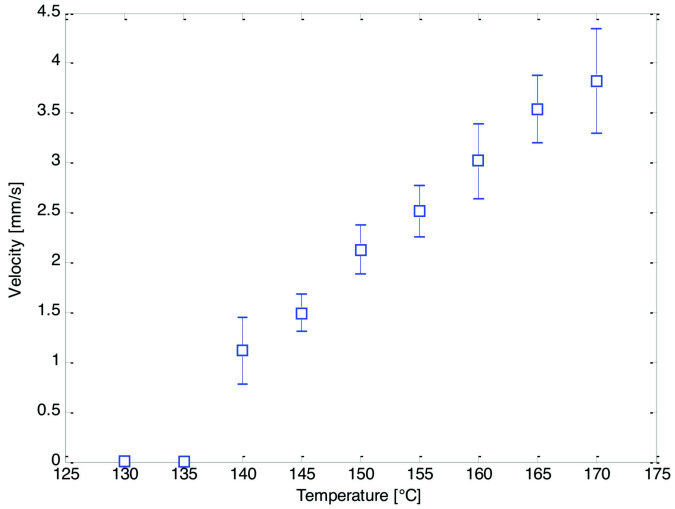

Figure 3.14: Rolling velocity as a function of the plate temperature for annealed PVDF fibers of diameter 0.5 mm. The errors bars are calculated from the standard deviations of ten measurements.

depicts a ”training” cycle of the fiber. The initial rolling velocity during the annealing of the fiber is slightly higher but doesn't display the linear relation of the rolling speed with temperature. The direction of rolling, spontaneously chosen at the onset can change due to collision with obstacles or defects on the surface. The higher melting temperature of nylon-6 ($T_{melt} = 215°\text{C}$) compared to PVDF ($T_{melt} = 177°\text{C}$) coupled with the fact that the onset temperature at a given radius is smaller for nylon-6 samples is the reason why nylon-6 is the main sample used in the experiments presented here.

The torques exerted by the thermal drive are sufficiently large to allow fibers to roll uphill on an inclined plane of slopes up to 15° against their own weight (see Fig. 3.15). These measures can be used to test the fidelity of the theoretical model by comparing the experimental data with the torque-velocity relation of eq. (2.29), it shows a good agreement with experiments.

Finally, an important property of the fiberboid and possibly the most important can be seen from Fig. 3.16, a quantitative study of the angular frequency ω as a function of the fiber thickness. The angular frequency strongly increases with decreasing fiber radius (this is true for both the fiberdrives and the fiberboids). This allows the fiberboids to reach rolling frequency up to 20 Hz for the thinnest samples measured (60μm radius). These high frequencies stand out from previously described thermally driven systems using the same material [14]. They are comparable to the beating frequency of the bacterium cilia [20] and the fastest light-driven azobenzene oscillators [28, 29]. The deformation flux through the material when driving the ZEEM share physical similarities with evaporating Leidenfrost droplets [49, 50, 51] but without the limitation of consuming the materials throughout the motion.

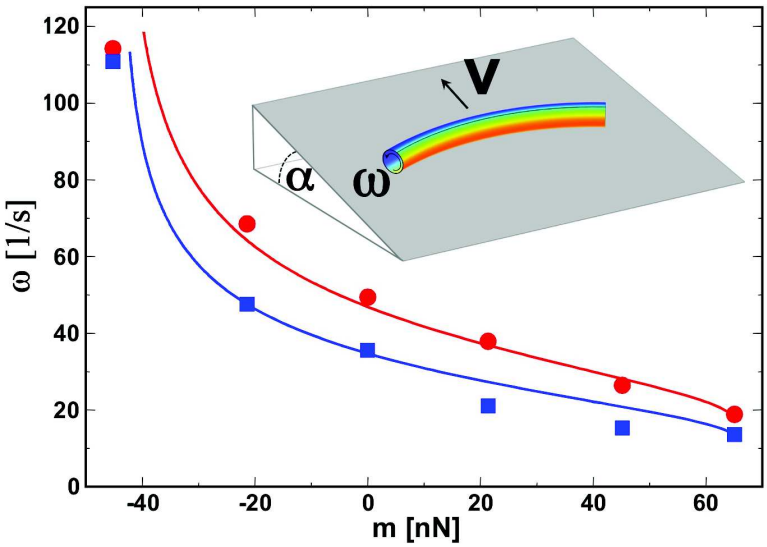

Figure 3.15: Single fibers are bidirectional motor units able to perform work, in the experiment shown here it is against their own weight on an inclined plane. Shown is the angular turning frequency of a nylon-6 fiber (0.2 mm radius) as a function of the axial torque per length at two different temperatures (red, 180°C; blue, 140°C). Solid lines are fits to the theoretically predicted torque-velocity relation of Eq. (B.60).

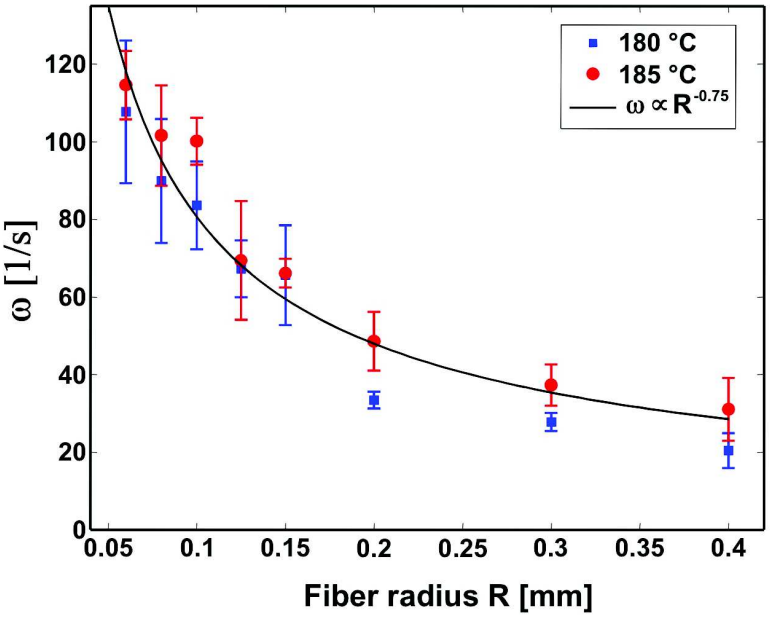

Figure 3.16: fibers with decreasing radii rotate with increasing angular frequencies: experimental data for two temperatures and a power-law fit $R^{-\gamma}$ with $\gamma = 0.75$. The errors bar are calculated from the standard deviation of three different specimen.

3.4 Conclusion

The experimental work presented in this chapter showed the practical feasibility of the "embedded wheel" described in the previous one, using simple, commercially available polymer fibers. toroidal and spiral fiberdrives as well as linear fiberboids consistitute one-piece soft motors that show uni-directional and bidirectional motion when driven out of equilibrium by a heat source. This shows that the abstract ZEEM concept can be utilized to generate real machines capable of performing work. The details of the model as well as some preliminary experiments imply that many other driving mechanisms can induce such rotation. The heat flux can be substituted with a humidity gradient, ions gradients or light illumination provided that they are elastically coupled to the material. The new paradigm of motion driven along ZEEMs calls for a revolution in the field of soft machines. The geometries investigated here are the simplest imaginable and only represent a proof of concept, the scaling properties of the speed of linear fiberboids point in the direction of miniaturizing such machines, perhaps taking advantage of their collective properties.

Chapter 4

A Rotary Motor Made out of DNA : the Hyperdrive

In the year of 1953, James Watson and Francis Crick forever changed the scientific landscape with their discovery of the molecular structure of DNA [58]. DNA is a polymer with a double-helical stucture, it is found in all living organisms and its main function is to carry genetic information. Given its major role in the reproduction process at the molecular level, it is no surprise that DNA was heavily studied by biologists, physicists and chemists alike. Following the initial discovery of the chemical structure, rapid progress in the field of biochemistry has been made. Not before long, man-made DNA structures were synthesized in the lab [59] in the form of branched structures made out of double-stranded DNA (dsDNA). This first step was followed in the next two decades by the report of increasingly complex realizations. It started from simple geometrical shapes such as cubes [60], dsDNA octahedrons [61] then single-stranded DNA (ssDNA) octahedrons [62], and culminating in the synthesis of complex 3D jigsaw puzzles made out of ribonucleic acid (RNA) [63]. The field of science concerned with building complex geometrical structures out of DNA-like biomolecules originated from the initial work of Seeman [59]. It later came to be named DNA nanotechnology [64, 65]. The progress in the field is exponential. In 2006, first reports of DNA origamis were made [66, 67]. By then, the degree of precision in self-assembly was such that it was possible to pattern a smiley face, 100nm in diameter on a surface. The challenge posed by Richard Feynman in 1959 to write the *Encyclopaedia Britannica* on the head of a pin [68] has been effectively conquered by DNA nanoscience. The extraordinary exploits of DNA origamis did not stop there [69, 70] and it is today possible to build complex switches and nanorobots [71] using this technique. The use of DNA as a building block is nowadays widespread and multiple companies around the world offer their service to provide customer-tailored solutions to design particular sequences of ssDNA with multiple modifications available at either end of the chain.

This chapter follows the main theme of the previous ones - "the material is the machine". A conceptual design for a DNA rotary nanomotor is presented. In the same way as for the fiberdrive, the rotary action of the engine stems from the geometry and topology of the DNA assembly. Before side-tracking on the journey towards the study of ZEEMs and soft machines, the initial goal of the PhD thesis was to study the statistical mechanics of confotronic biofilaments. The first part of this chapter is dedicated to the definition of the

global concept of confotronics, from a general conceptual perspective, to the description of a DNA-based confotronic fiber. The second part explains how the study of recent work about electrical switching of DNA assemblies grafted onto gold surfaces, coupled with previous expertise in the domain of molecular machines, shifted the project towards the making of a DNA-based nanomotor. Finally, the design and working principles of the motor are presented.

4.1 Confotronics

Confotronics is the study of large systems composed of individually soft switchable units, typically biomolecules. It typically follows the synergy concept of "the Whole is Greater than the Sum of its Parts". Through their interaction, the switchable units initiate complex, long-range phenomena that enable the formation of superstructures and biological tasks that a single unit cannot. The term confotronics was coined because similarly to their electronic counterparts, confotronic system are able to transmit conformation information along their elastic backbone across distances greater than the simple range of interaction of two neighbouring units.

A wide array of examples of natural confotronic systems can be found in the living cell where allosteric proteins and large assemblies such as filament lattices collectively switch states and shapes due to the complex interconnectivity and mechanical interaction of their constituting monomers. Classical examples include the hemoglobin molecule [72] whose conformational configuration is influenced by the concentration of oxygen molecules in the blood and can switch cooperatively between an oxy-conformation and a deoxy-conformation, or the DNA itself whose bases can flip, tilt and rotate around the main axis [73], see Fig. 4.1. For instance, when going from physiological conditions to high salt conditions, the switch of a basepair from the B to the Z conformation can cascade along the DNA backbone and collectively switch the whole molecule. Further examples are found in the cytoskeleton. Actin and microtubule biofilaments, on top of being tracks for the molecular motors myosin and kinesin, are confotronic biofilaments. The elementary units composing the microtubule - the tubulin dimers - act as a curvature switchable elements [43, 74, 75, 76]. When closed to a ring, photoinduced switching of the inter-unit twist of actin filaments leads to supercoiling of actin rings [77]. In these examples, the switchable character of the large assemblies finds its origin in the molecular complexity of their basic subunits (ie. the multiple conformations) coupled with their inter-neighbour interactions. The particularity of confotronic systems is that the multistability of the constitutive subunits is not averaged out on their biologically relevant lengthscales (of nanometers to microns) but instead gives rise to a collective behavior on a large scale. This means in turn that their "smart" features cannot be described by the classical models of semiflexible polymers such as the Worm-Like Chain [78].

Outside the cell, shape-memory alloys [79] can also be considered confotronic systems. Under the right loading conditions and temperature, their lattice can undergo strain-induced collective switching that reverts back to the original state when the stress is removed. Rigid bonds between neighbouring unit cells of the lattice make it energetically

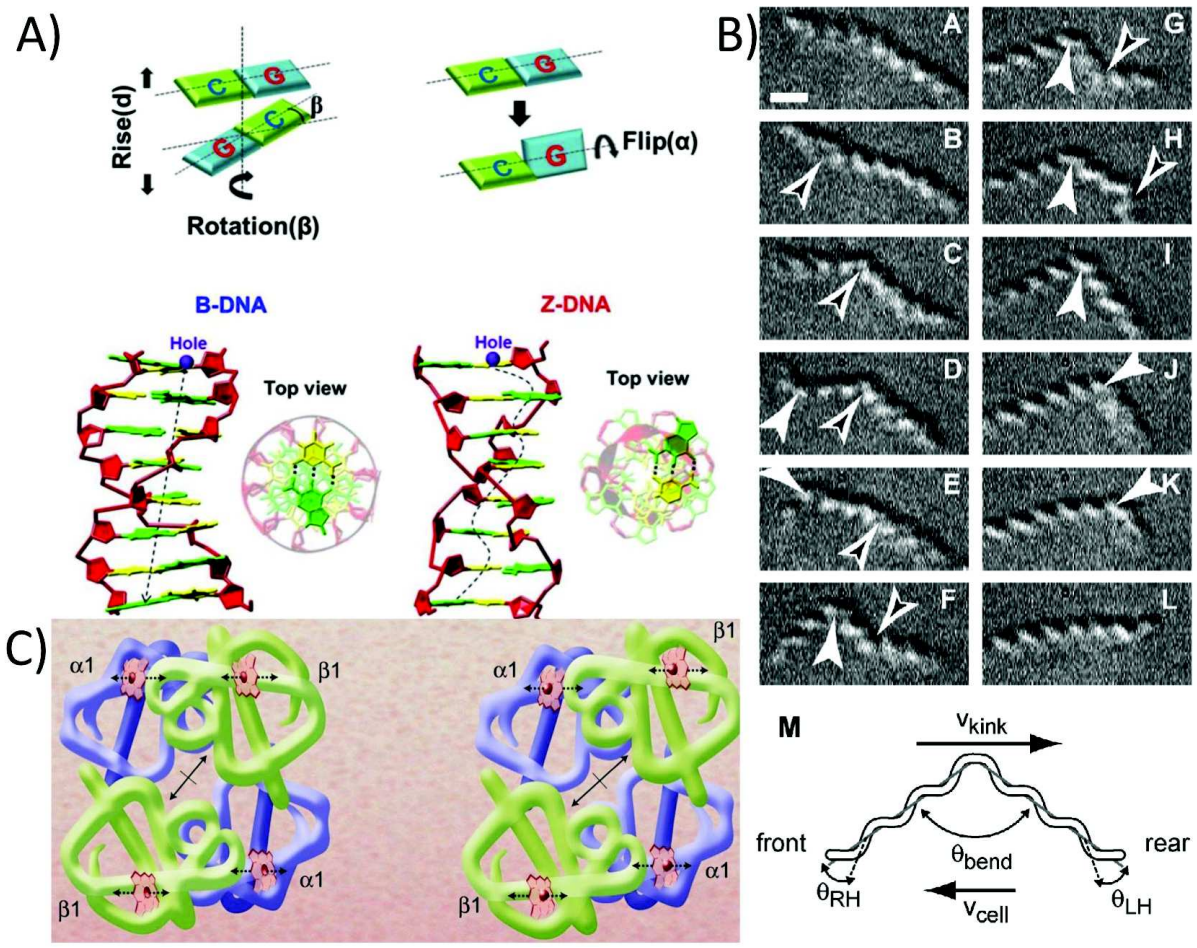

Figure 4.1: Natural confotronic systems in nature. A) At high salt, collective flipping and rotations of DNA basepairs induces a collective switch from the right-handed conformation of B-DNA to the left-handed conformation of the Z-DNA, from [73]. B) The bacteria spiroplasma undergo active conformational transitions of their cytoskeletal sheet (found on the inside of their membranes). By undergoing a yet unspecified lattice switch that induces a right-left-helical kink and actively propagates along their body they manage to rapidly swim, from [47]. C) The transition from the oxy-conformation (left) to the deoxy-conformation (right) in hemoglobin is correlated with the oxygen concentration in the blood, from [72].

favorable for the whole lattice to switch cooperatively. Finally, one of the most striking example of confotronics is found in the bacteria spiroplasma [44, 45, 46, 47, 48]. They move by propagating a conformational wave in the form a a kink along their backbone, see Fig. 4.1 B).

In 1965, Jacques Monod, Jeffries Wyman and Jean-Pierre Changeux exposed in their seminal paper [80] a theoretical model to explain the nature of allosteric transitions, known as the MWC model. It can be used successfully to describe the binding curve of oxygen on hemoglobin as a function of oxygen concentration. Its basic assumptions can give an insight at what are the minimal requirements for a confotronic system and help install a general framework for the conception of synthetic ones. All examples presented above share some common motifs,

- A confotronic system is an assembly composed of basic subunits. The subunits are mechanically and elastically coupled, there is a strong interaction between neighbours. This interaction couples any conformational change in a subunit to the contacting subunits in a positive or negative manner.

- The basic subunits of the system have a discrete number of conformations (cf. the oxy/deoxy-conformation in hemoglobin, or the two lattice arrangements of martensite and austenite for TiNi shape memory alloys). In general, bistability is prevalent and it is a sufficient condition for the presence of a global switching of the system.

- Anisotropy in the systems steers the switching process. It can be geometrical anisotropy (for instance the right-handed vs the left-handed conformation of the lattice of the spiroplasma on each side of the propagating kink). Or more generally, anisotropy in the energy landscape of the different conformations favors an equilibrium of the system in one particular conformation. External parameters (oxygen concentration for the hemoglobin, stress and temperature for shape-memory alloys or salt conditions for DNA) can shift the minimum of energy from one state to an other and thus induce a conformational switch.

- In some cases, global constraints can lead to the emergence of collective variables - the previously described ZEEMs (see section 2.1) - that even in the absence of geometrical anisotropy couple monomers together over a long range (for instance the curved state of the microtubule lattice [43]).

Figure 4.2 depicts a basic first approach of a synthetic confotronic fiber. The idea is to create polymer chain based on the motif of industrial scissor lifts. The basic subunit of the chain consist of two rigid polymer chains (of a length small compared to their persistence length) linked together in the middle by an axle of rotation. It is expected that akin to the macroscopic design it is based on, the state of the subunits along the chain are correlated to one another. For a perfectly rigid chain, this correlation is one and all ”scissor”-units share one common state of ”openess”. For a system based on semiflexible polymer chains, a perturbation opening one subunit at one end is transmitted along the chain but damped

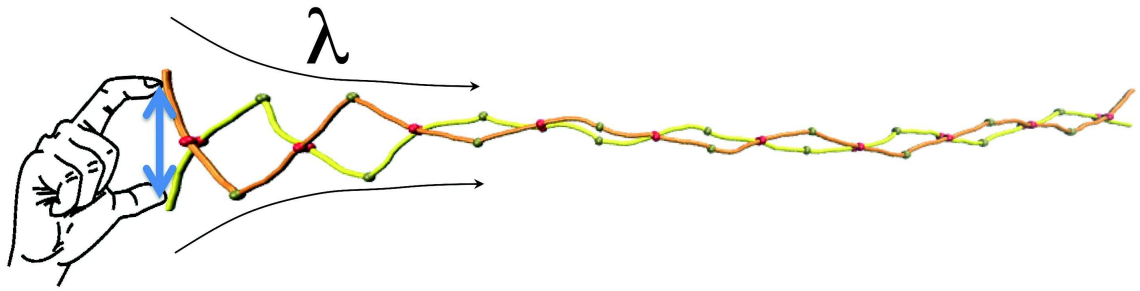

Figure 4.2: Propagation of a mechanical perturbation along the backbone of a model polymer - the scissor-foldamer. The connectivity between individual "scissor"-units allows for some cooperativity between neigbours.

over some distance λ by thermal fluctuations in the elastic medium.

Previous work done as part of a master thesis showed that in this simple design, the geometrical state of neighbouring subunits is indeed correlated. However this didn't go beyond qualitative observations within the frame of a simplified coarse-grained molecular dynamics simulation. These preliminary results were encouraging enough to motivate a more ambitious project - the design of a synthetic confotronic fiber made out of DNA.

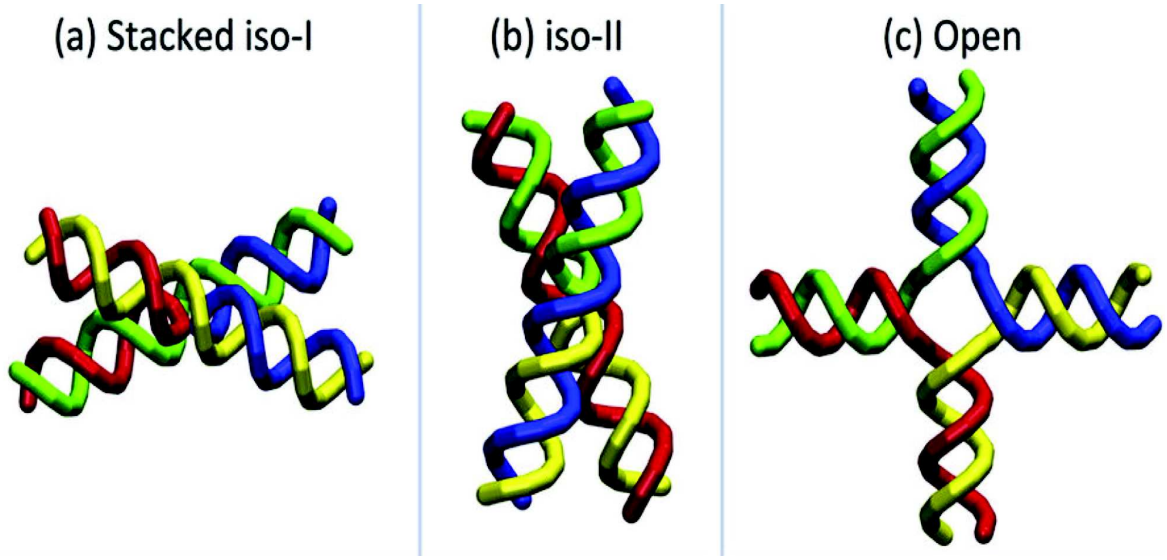

Figure 4.3: **Idealized schematic of the junction conformations.** The stacked (a) iso-I and (b) iso-II conformations predominate at moderate and high salt concentrations. (c) The open conformation is mainly observed at low salt concentration, and also potentially acts as an intermediary of conformational changes between iso-I and II, from [81].

The construct of Fig. 4.2 only presented one of the key aspects of contronics presented above, mechanical connectivity between subunits. A special branched structure of DNA can be added into the design to bring bistability into the mix. The Holliday junction [82], was proposed by Robin Holliday in 1964 [83]. It is a four-way branched structure of

dsDNA which is a key intermediate in many types of genetic recombinations as well as in double-strand break repair. For the purpose of building a confotronic fiber, it has a very interesting property, it exists in three different conformations [84, 85, 86, 87, 88, 89, 81], see Fig. 4.3.

DNA being negatively charged (2 negative charges carried by the phosphate groups on each side of a basepair), the natural state of the Holliday junction at low salt concentrations (below 0.1mM Mg^{2+} is the open one (cf. Fig. 4.3 (c)) where the four branches are as far away as possible from each other due to electrostatic repulsion. By increasing the salt concentration in solution, the screening of the DNA backbone by the salt ions in solution switches the conformation of the junction towards the more energetically favorable iso-I and iso-II states.

The idea behind the confotronic DNA fiber is to synthesize a polymer fiber constituted of Holliday junction-monomers. A coarse-grained representation of the dimer is depicted in Fig. 4.4. The expectation is that the transition from open to stacked conformation of the constituting subunits of the fiber as the salt concentration is raised can be accelerated with increasingly longer fiber. In order to probe the system, gel electrophoresis can be used to get an idea of the general conformation of the fiber. Some preliminary work presented in the next chapter has been done in this direction. On top of that, a magnetic tweezer setup will eventually be used to measure force-extension curves of the fiber at different salt concentrations.

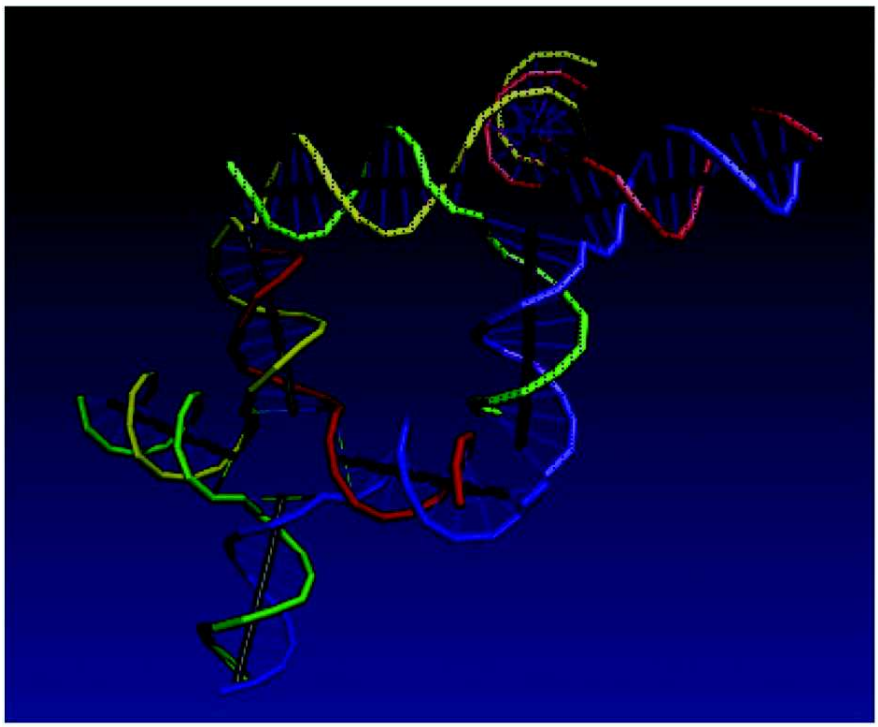

Figure 4.4: Coarsed-grained representation of confotronic dimer. It consists of two switchable Holliday Junction-units linked together.

4.2 The Hyperdrive design

This part expands on some of the concepts presented above, and presents some new ones in order to get the global framework in which the DNA motor Hyperdrive is set.

4.2.1 Motivation

The first ingredient of the nanomotor is its rotary nature. It is provided by the Holliday junction. On top of the properties of the Holliday junction presented in the previous section (bistability of conformations), an additional property of this construct is the ability to migrate. When the DNA sequence of a Holliday junction is palindromic (as is often the case in living systems), it can migrate along the dsDNA strand [90], effectively moving the center of the junction in a diffusive manner, see Fig. 4.5. A palindromic sequence is a sequence on dsDNA wherein reading 5' to 3' forward on one strand matches the sequence reading to 5' to 3' on the complementary strand with which it forms a double helix. Thus a palindromic sequence can form a hairpin (a ssDNA loop popping out of a linear dsDNA). The Holliday junction migration is accompanied by a rotational motion of the four branches constituting the junction at a rate equal to the pitch of dsDNA (10.5 base pairs per turn). Independently of the direction of migration, two opposite branches will turn clockwise while the other two turn anti-clockwise relative to the center of the junction.

A palindromic sequence is a nucleic acid sequence on double-stranded DNA or RNA wherein reading 5' (five-prime) to 3' (three prime) forward on one strand matches the sequence reading 5' to 3' on the complementary strand with which it forms a double helix. This definition of palindrome thus depends on complementary strands being palindromic of each other.

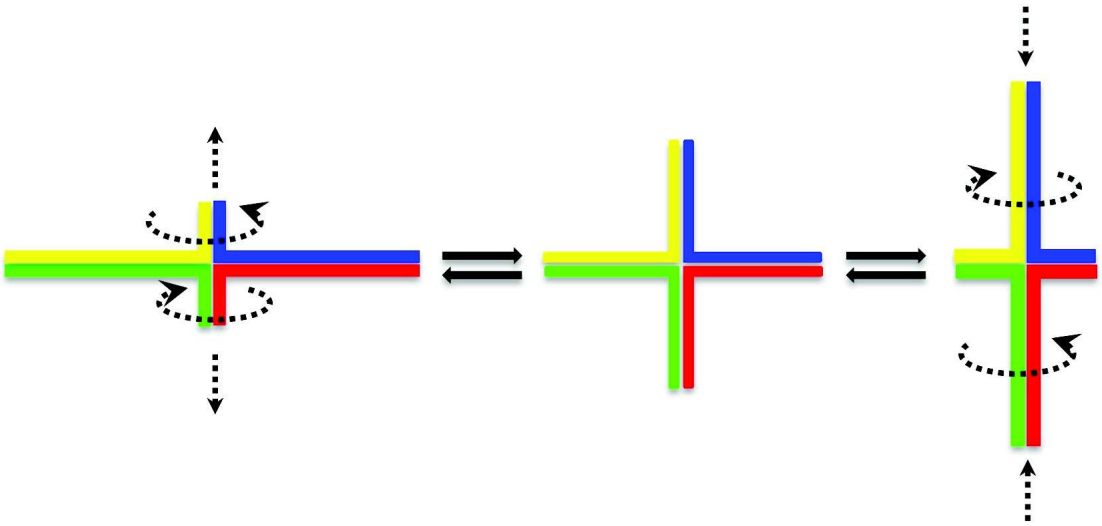

Figure 4.5: A Holliday junction with a palindromic sequence can undergo a branch migration in a diffusive manner. The process is accompanied with rotation of the four branches at a rate of 1 turn for every 10.5 basepairs migrated.

In a previous work realized in the group, a rotary motor called a tanglotron was studied theoretically [91] and realized experiementally [92]. A tanglotron is a cyborg-hybrid between an active rotary motor unit and a passive entanglement unit. The core of the motor is a functioning molecular motor like Feringa's rotary photo engine [93]. Due to the delicate structure of synthetic molecular motors, they tend to easily jam or break when rigidly coupled to anything bigger than them. The main idea in the conception of the tanglotron is to attach soft polymer chains to the device, in order to capture and conserve the rotations generated by the motor in the topology of the chains. Coupling the chains (acting as a buffer between the motor and the environment) to something else allows for the transmission of the motor's rotation. Potential applications of this engine are represented in Fig. 4.6. The parallelization of multiple tanglotron engines depicted in (a) has been realized experimentally [92] to create a dynamically entangling polymer gel. The idea presented in Fig. 4.6 (c) shows a combination of a migrating Holliday junction with a tanglotron in order to convert simple rotational motion to a combination of linear and rotary motion.

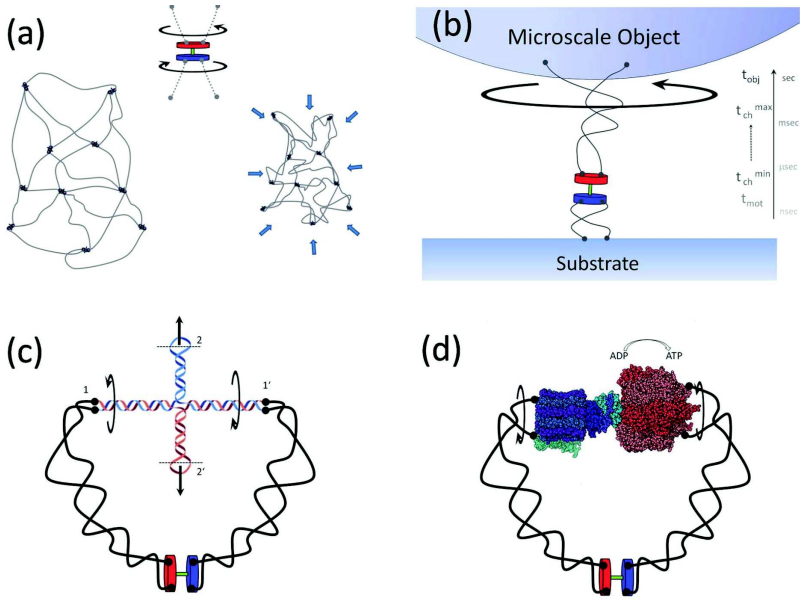

Figure 4.6: Applications of the tanglotron. (a) A "topo gel" consisting of reticulated tanglotrons acts as an artificial muscle. (b) The time-scale-bridging function of a tanglotron. It can easily move objects billion times heavier than itself via the trick of transient energy buffering in the chains. (c) The rotary motion can be transformed into linear actuation via a DNA cruciform structure (at positions 1 and 1'). The tanglotron device can now bridge to any DNA nano-assembly if we cut/open the end loops of the cruciform at connections 2 and 2'. The cruciform transmits both rotary to rotary motion and rotary to linear motion. (d) The motor unit can be directly coupled to distant catalytic centers that act as energy consumers, here an ATP-synthase. The (transmembrane) proton motive subunit of the ATP-synthase is replaced by the distant rotary motor, softly coupled by polymer chains. In reverse, supplying the synthase with excess ATP turns it itself a rotary motor unit, from [91].

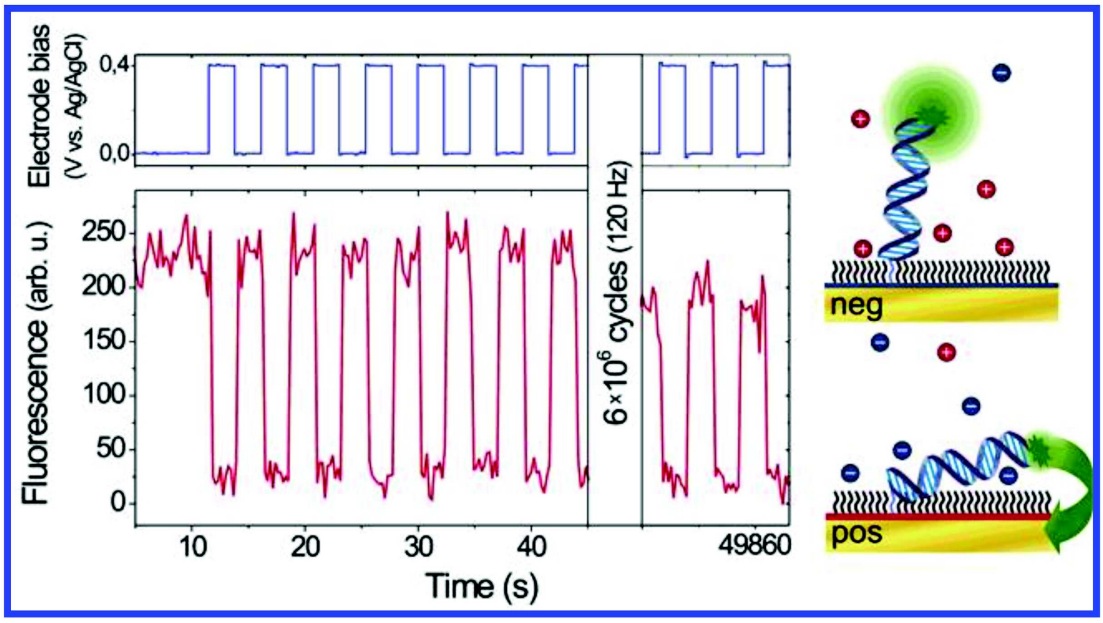

Figure 4.7: Electrically induced, persistent switching of a DNA layer on a Au surface. Left: The fluorescence intensity observed from the dye-labeled DNA layer alternates upon periodically reversing the electrode charge. Right: Negatively biased electrodes repel the likewise charged DNA strands, bright fluorescence is emitted from the dye attached to the DNA's top end. Positive surface charge attracts the strands and due to the close proximity to the metal efficient energy transfer from the excited dye to the Au results in a substantial quenching of fluorescence, from [103]

In the last 20 years, with the advent of DNA as a building block for complex assembly, a consequent amount of research has been done on assemblies of thiol-modified DNA on the surface of metals, especially on gold [94, 95, 96, 97, 98, 99, 100, 101]. In particular, the group of Ulrich Rant in Munich has done a lot of research on electrical switching of DNA monolayers on gold surfaces [102, 103, 104, 105, 106, 107, 108, 109, 110]. The basic idea behind their first papers is depicted in Fig. 4.7. DNA is fluorescently labeled on one end and modified with a thiol group on the other end. It is then grafted on a gold electrode. Given the negatively charged nature of DNA, the application of a positive potential at the electrode attracts the strands towards the surface. Due to the close proximity of the fluorescent dye to the gold surface, the fluorescence is quenched. Conversely, when a negative potential is applied at the electrode, the DNA is repelled from the surface and bright fluorescence is emitted from the dye. Dynamical switching back and forth between positive and negative potential at the electrode can be directly correlated with the fluorescence signal emitted by the dye. Following this proof of concept, Rant's group has been using increasingly complex DNA structures to build for instance bioassays for enzymatic activity. The probing of these systems always relies on the attraction and repulsion of DNA strands from the surface upon application of electrical potentials.

4.2.2 Conceptual Design

All the ideas and concepts presented in this chapter serve as a motivation for the design of nanomotor presented in the following section - the HyPERdrive, standing for Hybridization Pawled Electro Ratchet. It is a DNA based assembly grafted onto the surface of a gold electrode and driven by the application of electric field in order to rotate micrometric beads thousand of time bigger than itself. Electrically actuated DNA based machines have already been realised [111] but not with the goal of coupling objects with such a difference of size.

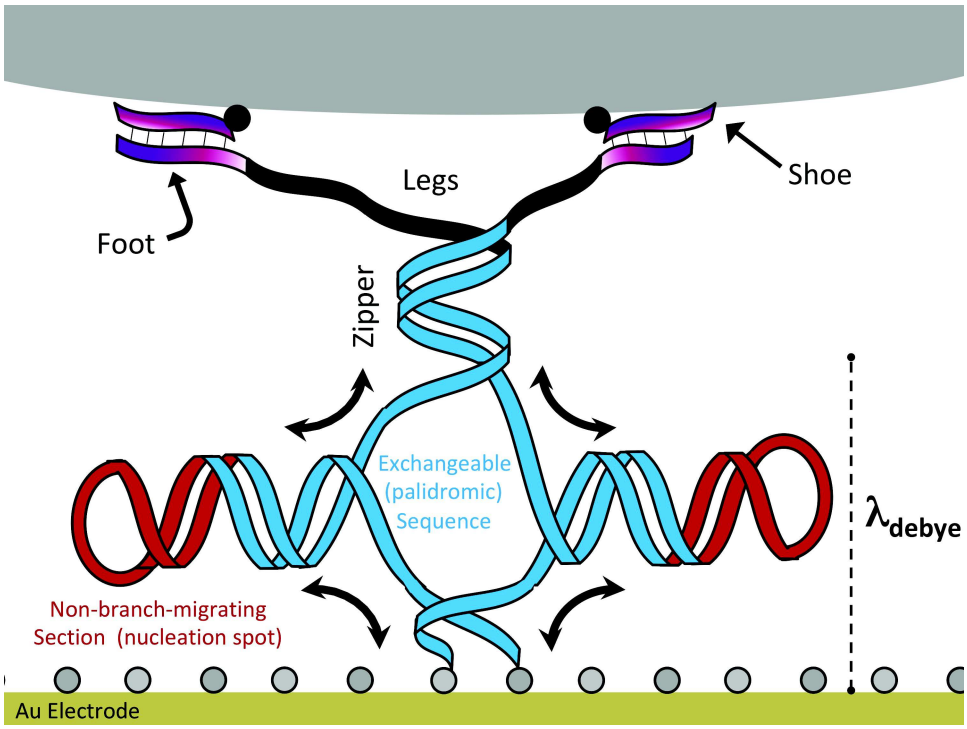

Figure 4.8: The design of the HyperDrive. The motor is grafted onto a gold electrode via thiol groups at the end of the two strands, the rest of the surface is covered by mercaptohexanol molecules. The part that can be actuated via an alternative potential is pictured in blue, it can migrate between two extreme positions thanks to it palindromic sequence. The "feet" are complementary to the "shoes" grafted on the micrometric bead and allow for the coupling between the motor and the bead, they can transmit the rotation caused by the migration of the junction to the bead.

The design is presented in Fig. 4.8. The bulk of the motor consists of a palindromic Holliday junction that can migrate to transmit rotational motion. It is build out of two ssDNAs that have been modified on one end with thiol groups in order to attach the construct onto a gold electrode. The migration of the junction is stopped at the extreme position of elongation of the motor by the non-palindromic stoppers represented in red. On top of the construct, the junction is linked with two ssDNA strands reminiscent of the polymer chains of the tanglotron motor. They store the rotation induced by the migration of the junction and couple it to the bead localized above the motor. The last part of

the design are the "feet" of the motor localized at the end of the two chains. The "feet" sequence is complementary to the one of the "shoes" (the hybridization part of the motor), short ssDNA sequences 10 base pairs in length. The "shoes" are modified at one end with a biotin molecule. This allows them to covalently bind to streptavidin molecule present at the surface of micron sized-bead. The surface of the gold electrode is covered with mercaptohexanol following the grafting of the DNA assembly to prevent non-specific interactions between the DNA and the gold surface (see the experimental part in the next chapter).

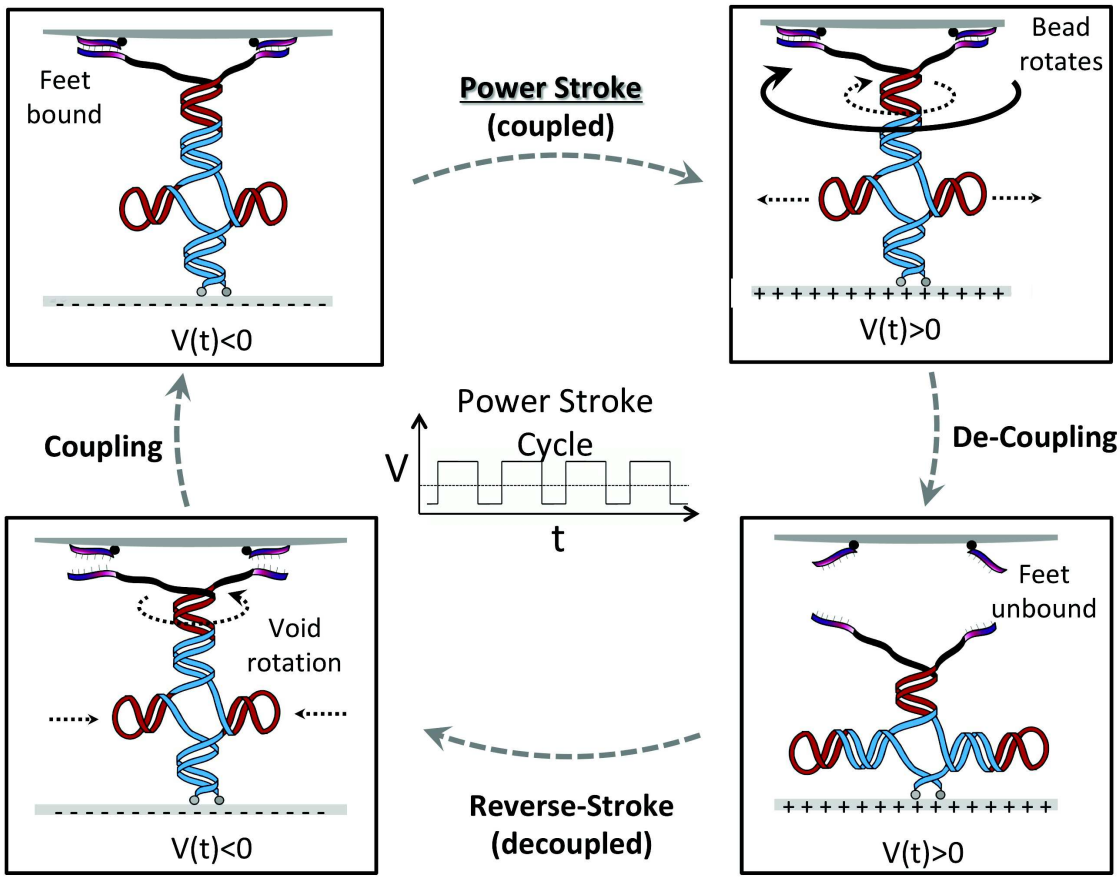

Figure 4.9: One powercycle of the HyperDrive. Starting on the top left with a negative potential, the construct is fully extended and bound to the bead. Upon switching to a positive potential, the junction starts to migrate, causing the rotation of the bead bound to the end strands. The rate of the branch migration added to the torque exerted by the Hyperdrive rips off the feet from the bead. Once it has reached the end of its course, the construct is flat on the surface and unbound from the bead. Switching back to a negative potential, the junction starts to migrate the other way around but the end strands undergo a void rotation since they are not bound to the bead. At the end of this step the junction is back to a fully extended state and bound to the bead, reaching the end of one cycle.

The motor is driven by an alternating electrical potential applied between the gold

electrode and a distant electrode. Contrary to the simple strands switching in the examples presented above (see Fig. 4.7), the DNA construct will not bend towards the surface upon the application of a positive potential. Instead, the migration of the Holliday junction in the construct towards a configuration where the whole construct is lying flat on the surface (see the bottom right pannel of Fig. 4.9 is energetically preferable. The figure presents one powercycle of the Hyperdrive. Starting with a fully extended configuration and a negative potential at the electrode, the switch is made to a positive potential. The junction starts to migrate towards the surface, causing the two ssDNA strands to rotate and the micrometric bead alongside them. The combination of the shrinking of the construct and the torque applied by the rotation eventually rips of the "feet" from the "shoes". When switching back to a negative potential, the system goes back to its initial configuration but without coupling the rotation of the strands to the bead. Given the chirality of DNA and the way this cycle is thought of, one can expect the bead to rotate in the same manner as a lightbulb is screwed. Repeating this cycle at a rate of 100Hz to 1kHz and considering that each bead will hover over hundreds to thousands of motors this should allow the bead to achieve several turns around its axis per second.

4.3 Conclusion

In this chapter, the concept of confotronics was described. It can be defined as the study of large systems composed of individually soft switchable units. Many examples can be found in nature and given the common denominators in these examples it is possible to design an idea of synthetic confotronic systems. Such a system is described in the form of a DNA-based confotronic fiber, taking advantage of the properties of the Holliday junction to embed collective features in a man-made polymer.

The previous work of this group on the tanglotron was briefly presented. This served, along with the migration feature of the Holliday junction and the work on electrically switchable DNA construct grafted onto gold surfaces, as a motivation for the design of a rotary nanomotor made out of DNA. This motor - the hyperdrive - combines all the previous ideas into one grand design. It is an electrically actuated DNA construct grafted onto a gold electrode that transmits the rotational motion of a construct based on a Holliday junction to a micrometer sized bead. It effectively couples nanometer lengthscales to micrometer sized objects.

The following chapter will be focused on the experimental developments that have been made on these ideas during the course of this PhD.

Chapter 5

Ongoing Experimental Endeavors

In this chapter, several ongoing experimental projects are discussed. For all of them, they started during the course of the PhD thesis with no prior knowledge in the field. The budget for these projects was very limited so the first steps (presented here) were all done in house or in the neighbouring institute (Institut de Physique et Chimie des Matériaux de Strasbourg or IPCMS). Given the very early state of development, most of the results are qualitative rather than quantitative and some lack a proper explanation. For the most part, the experiments are done in the field or molecular biology. They were performed in IPCMS under the guidance of a close biophysicist collaborator, Dr. Wilfried Grange. Some of the protocols originated with him and others were devised after studying the scientific literature. For the sake of brevity, only the "successful" attempts are reported here. The details of the experimental procedures are in Appendix C.

Two projects are presented here. The first is a brief excursion into the making of the confotronic fiber presented in section 4.1. The second is about the Hyperdrive nanomotor. Its design and construction is detailed and followed by the presentation of an interesting experimental setback. When trying to observe fluorescently labeled DNA grafted onto a gold surface, a fluorescent autowave forms. This wave is the consequence of convection flows believed to be induced by the heating of the gold surface by excitation light. This flow is described and possible leads towards its applications are explored.

5.1 Confotronic Fiber

The basic motif of the confotronic dimer presented in Fig. 4.4 is the imobile Holliday junction. In can be realized easily from four different oligonucleotides (ssDNA strands). Fig. 5.1 presents the sequences of 6 different oligonucleotides used to build two separate Holliday junctions. The idea behind this scheme is to reproducibly assemble confotronic dimers from these two junctions. The sequences are non-palindromic to prevent branch migration. Depending on the salt concentration (here of divalent ions Mg^{2+}), the junctions can exist in an open or a closed conformation.

HJ1 :

OLOO1	5’ATT CGG GAA GAT AGT ATC GCG ATG AGC AGG AGA GTT AGA GTA TCT TAA TCA TC ‘3
OLOO2	5’GCA TCG TAA TGC TTA TGG CTG TTC GGT CCT GCT CAT CGC GAT ACT ATC TTC C ’3
OLOO4	5’ATG CCA CAC GCT GCC ATA TCC AGA AGG CAT TCC GAA CAG CCA TAA GCA TTA CG ’3
OLOO7	5’CCG ATG ATT AAG ATA CTC TAA CTC AAT GCC TTC TGG ATA TGG CAG CGT GTG GCA TCC ‘3

HJ2 :

OLOO1	5’ATT CGG GAA GAT AGT ATC GCG ATG AGC AGG AGA GTT AGA GTA TCT TAA TCA TC ’3
OLOO3	5’GAA TGA TGA TTA AGA TAC TCT AAC TCA ATG CCT TCT GGA TAT GGC AGC GTG T ’3
OLOO4	5’ATG CCA CAC GCT GCC ATA TCC AGA AGG CAT TCC GAA CAG CCA TAA GCA TTA CG ‘3
OLOO8	5’CCC GTA ATG CTT ATG GCT GTT CGG TCC TGC TCA TCG CGA TAC TAT CTT CCC GAA TCC ‘3

Figure 5.1: Oligonucleotides used to from the two distinct Holliday junctions used as monomers for the confotronic fiber.

The junctions are build individually, following the protocol of section C.2.1. In order to form the dimers, the two junctions need to be assembled via an enzymatic reaction with the DNA T4 ligase, following the protocol of section C.2.1. The result of such an assembly is shown in Fig. 5.2. The two points where the junctions ”meet” is where the DNA T4 ligase links them together. Both the single junctions and the dimers can be synthesized in large quantity, reproducibly and stored in the fridge for months.

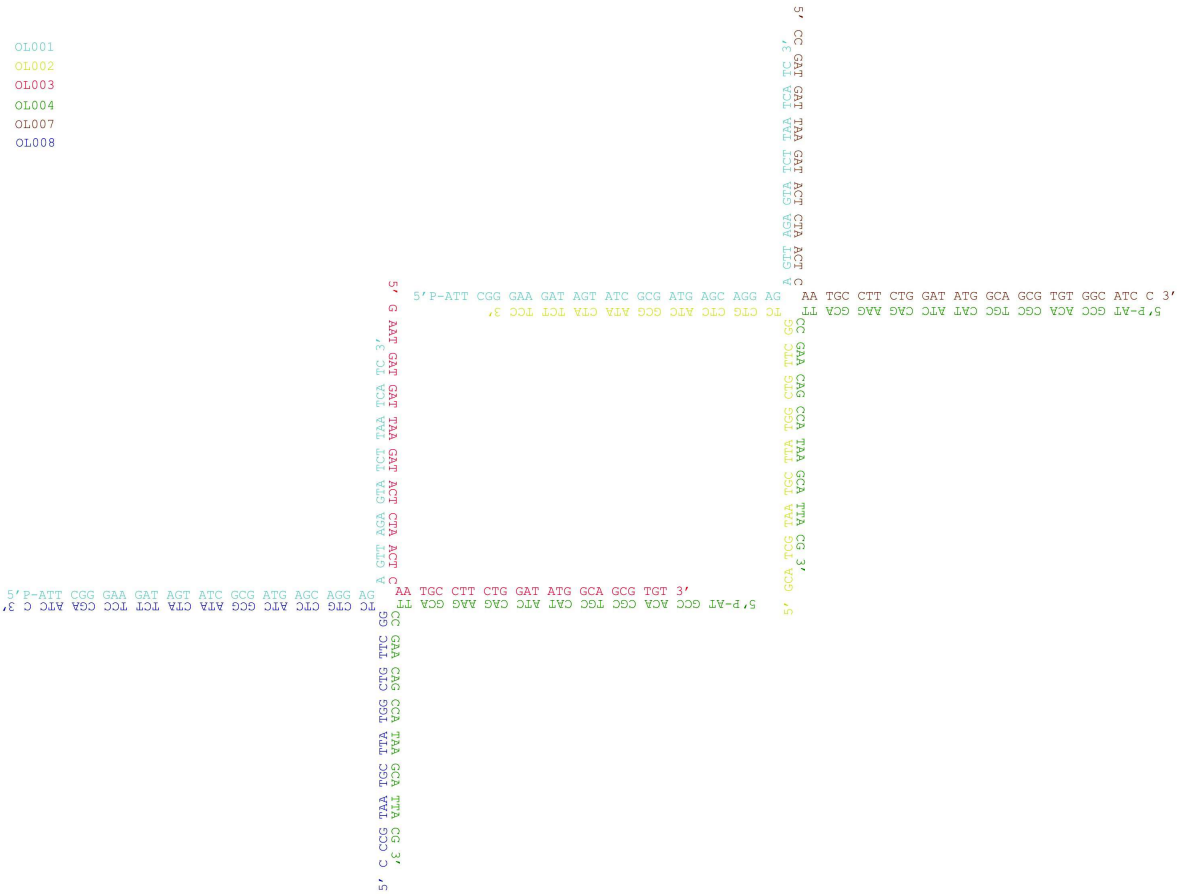

Figure 5.2: Schematic of the confotronic dimer showing the complementary sequences as well as the two points where the junctions are linked by the DNA T4 ligase.

This initial study focused on monomer and dimer only. The next step would be either to increase the degree of polymerization one by one by designing specific sequences allowing only the formation of 3-mers, 4mers, etc., or go towards the route of a more realistic polymer with a basic sub-unit, a single Holliday junction. While the latter method would have the advantage of being cheaper, the degree of polymerization would not be controlled, there would be a statistically distributed population of polymers going for monomers to n-mers (n being the highest degree of polymerization attained during the synthesis process).

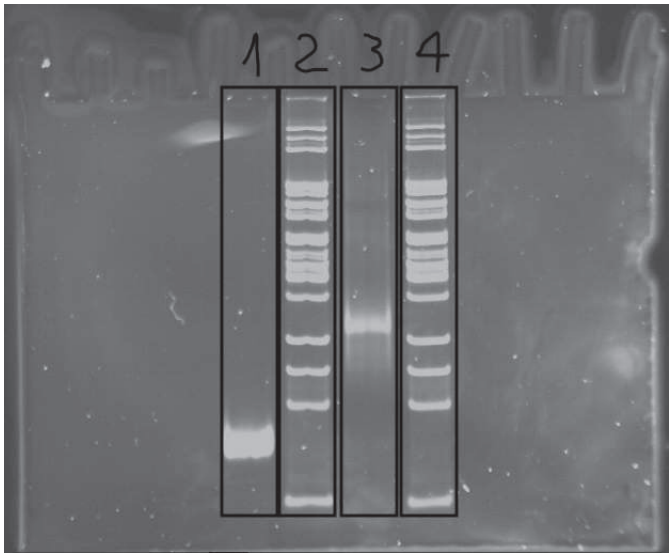

Figure 5.3: Example of a polyacrylamide gel run at 2mM Mg^{2+} concentration. Line 2 and 4 are the DNA ladder from Fig. C.1. Line 1 is a single Holliday junction and line 3 is the confotronic dimer.

Following the synthesis, the monomers and dimers are studied by gel electrophoresis under varying salt concentrations in solution. Gel electrophoresis is a method used for the separation and analysis of charged macromolecules (such as DNA, RNA and proteins), based on their size (geometrical shape, weight) and charge. Nucleic acids placed into a porous gel (agarose or polyacrylamide) are separated by applying an electric field to move the negatively charged molecules though the matrix. Depending on the type of gel used and its density, the mesh size varies and can select different sizes of molecules. Lighter and shorter molecules can migrate further through the gel than longer and bulkier ones. They are compared to a calibrated ladder consisting of dsDNA fragments of known size, see Fig. C.1. An example of a polyacrylamide gel for the single Holliday junction and the dimer is presented in Fig. 5.3.

The salt dependence of the Holliday junction and the confotronic dimer is studied by running dozens of such gels at different Mg^{2+} concentrations. The gels are prepared following the protocol of subsection C.2.2 except that the TBE buffer has been modified. The EDTA is removed given that its main role is to trap metal ions present in the solution, it is not compatible with the divalent Mg^{2+} ions. The necessary quantity of Mg^{2+} ions is added to the buffer to reach the desired salt concentration for each individual gel.

The result of the comparative study of the monomer and the dimer is presented in Fig. 5.4. The bp label on the Y-axis corresponds to the weight of the DNA ladder band that is at the same height as the migrated band. As both the single junction and the dimer are branched DNA structures, they do not migrate in the same manner as simple dsDNA strands and thus this bp "size" cannot be correlated with the actual weight of the constructs. An examination of Fig. 5.3 shows that, as expected, the single junction migrates further than the dimer, due to its reduced size. For both the single junction and the dimer, a change in mobility can be observed as the salt concentration is increased. The transition from high to low migration distance for both the monomer and the dimer is a clear indication that the conformational transition from the "open" to the "closed" state is occuring.

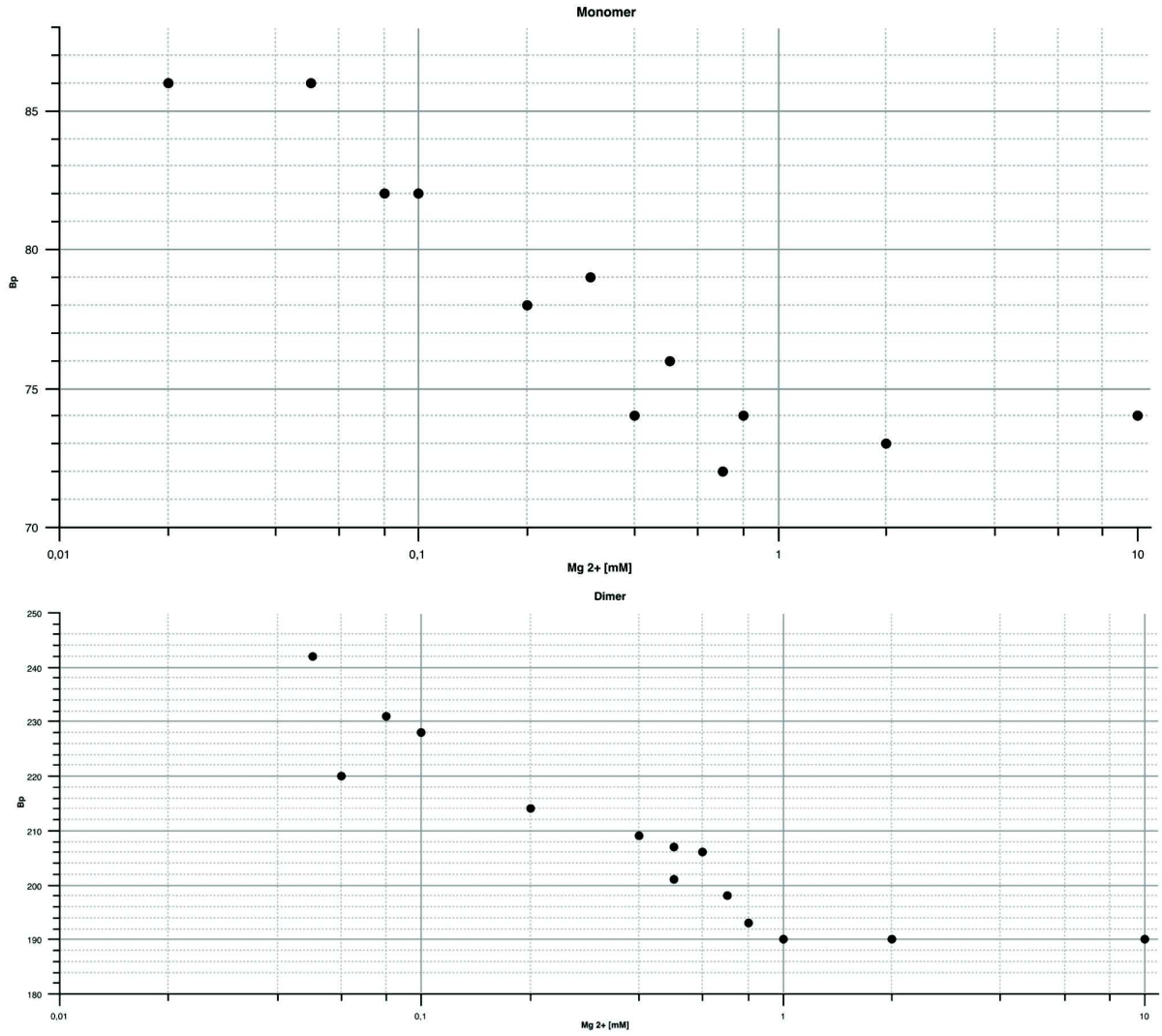

Figure 5.4: Comparison of the migration "speed" (the length in basepairs of a dsDNA migrating until the same height as indicated by the ladder lines) of the single Holliday junction and the confotronic dimer as a function of Mg^{2+} concentration.

However, it is not evident from Fig. 5.4 that there is a difference in the migrating behaviour of the single junctions and the dimers. The question remains as to wether or not the cooperativity between junctions in the dimer enhances the transition speed. In order to get a more precise idea, more gels are needed in the in-between missing points. Furthermore, what is expected is that the higher the degree of polymerization of the confotronic fiber, the more the migrating behaviour of the construct will deviate from the trend of the monomer. If there is a confotronic behaviour of the fiber, ie. a cooperativity between neighbouring units, the slope of the transition from low salt to high salt would become steeper, indicating a sharper transition and the establishment of a binary state of the fiber, open or closed.

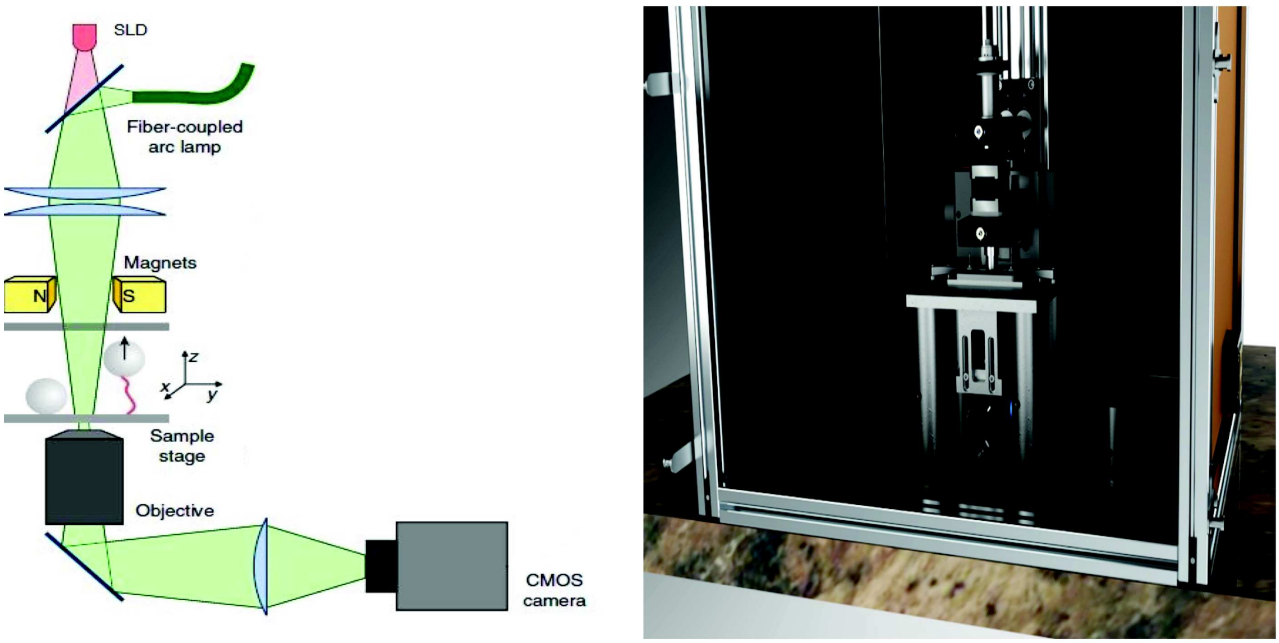

Figure 5.5: Left : scheme of a magnetic tweezer setup, from [112]. Right : 3D representation of the setup of Wilfried Grange in IPCMS on which the future confotronic fibers will be measured.

The next step envisioned in the project is the study of the confotronic fiber using the magnetic tweezer setup of Dr. Grange, see Fig. 5.5. This setup would enable the measure of force-extension data for a wide range of salt concentration fibers going from the monomer to the n-mer. Due to the use of the setup by successive master students, the collaboration is paused at the moment but it will hopefully resume shortly.

5.2 The Hyperdrive

The Hyperdrive design presented in Fig. 4.8 is synthesized in the laboratory using the oligonucleotides given in Figs. 5.6 and C.2. The assembly of the motor is made following the same protocol as for the Holliday junction of the previous section, see section C.2.1. However, given the complexity of the design, a few precautions and control experiments

have to be made to ensure that the final product is the one desired.

Figure 5.6: Full sequence of the four oligonucleotides constituting the Hyperdrive, see Fig. C.2 for more details.

Given the palindromic sequence of the Holliday junction at the core of the design, the construct can be in any conformation in between the two extremes presented in Fig. 5.7. The flat conformation correspond the the idealized case where the motor lies flat on the surface of the gold when a positive potential is applied between the electrodes. Conversely, when a negative potential is applied between the electrodes, the construct is expected to be fully extended away from the surface.

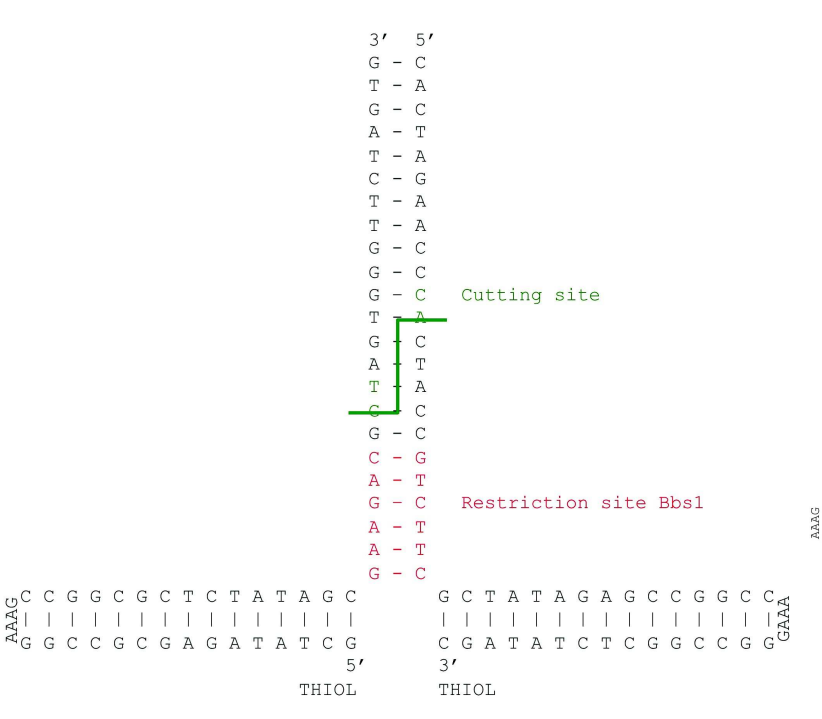

(a) Flat conformation.

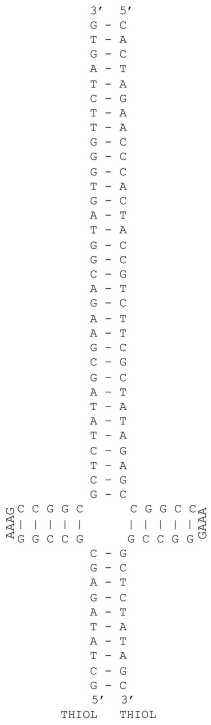

(b) Extended conformation.

Figure 5.7: The two extreme configurations of the Hyperdrive construct (without the ”legs”). The overhangs on the sides present both on the left and on the right are the non-palindromic ”stoppers”. When a positive potential is applied at the electrode, the construct lies flat on the surface. The red part is recognized by the enzyme BbsI that cuts the dsDNA strand in the location marked in green. When a negative potential is applied at the electrode, the construct is fully extended away from the surface.

Another structural property of the construct is highlighted in red and green in Fig. 5.7a. Its sequence includes a restriction site for the enzyme BbsI (in red). When the right conditions are met (see section C.2.1), the enzyme can cut the Hyperdrive in half at the site marked in green in the figure. The action of the enzyme is possible only when the construct is fully hybridized, hence successful cutting is a proof of an equally successful synthesis of the Hyperdrive.

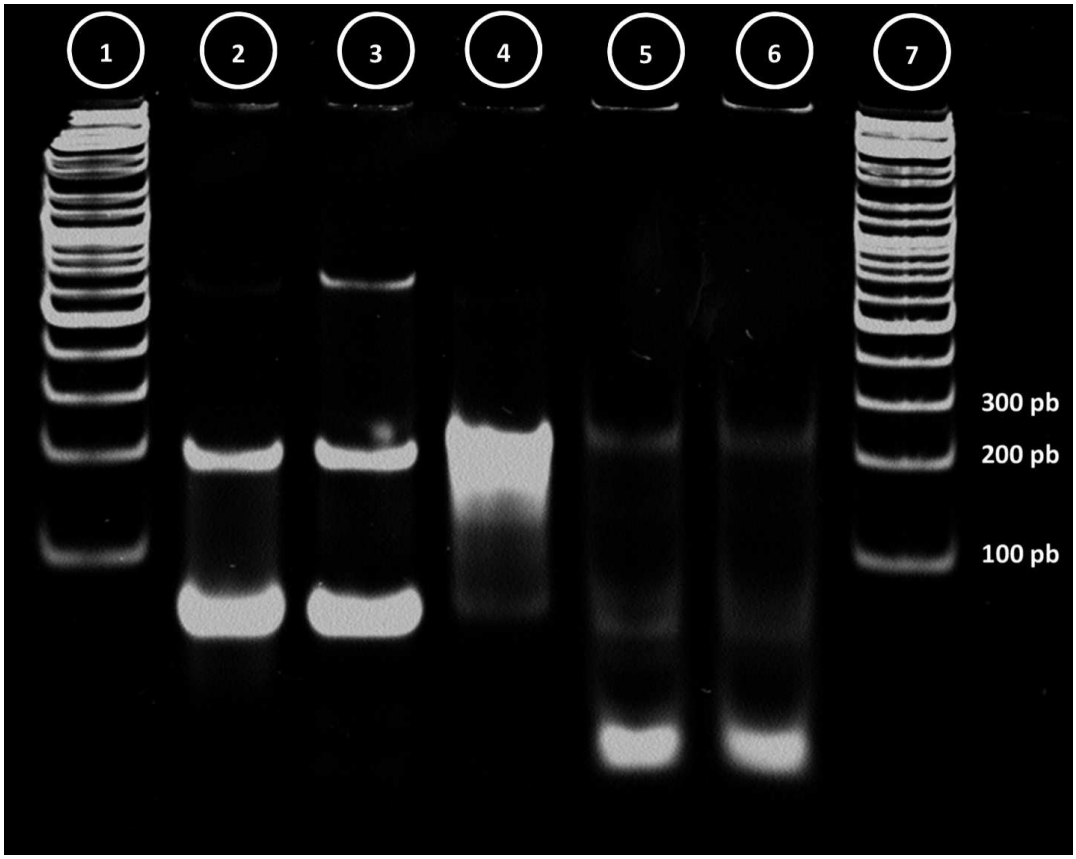

Figure 5.8: Polyacrylamide gel used to control the assembly of the Hyperdrive. Line 1 and 7 : DNA ladder of Fig. C.1 right. Line 2 and 3 : oligonucleotides constituting the motor, OL 64 and 65 respectively, see Fig. C.2. Line 4 : the fully assembled Hyperdrive. Line 5 and 6 : twice the same content, the assembled Hyperdrive digested by BbsI.

In order to test wether or not the assembly was successful a series of experiments, summarized in Fig. 5.8, was performed. The figure presents within one polyacrylamide gel control experiments that were repeated multiple times in isolation. It compares the migration of the oligonucleotides OL64 and OL65 composing the Hyperdrive with the full construct. Where the single oligonucleotides show multiple bands (corresponding to secondary structure, hairpins for example), the Hyperdrive presents only one smeared out band. In addition both single strands migrate further than the construct for their lower band which is to be expected considering their size. The smeared out band for the Hyperdrive can be explained by the coexistence of multiple similar conformations existing between the two extremes of Fig. 5.7. Finally, the last two wells show the same thing, the

result of the restriction of the Hyperdrive by the enzyme BbsI. While the interpretation of the different bands cannot be absolute, the fact that there is a structural difference between the full construct and the cut one is undeniable. The bright lower band might correspond to the section above or below the cutting site. In the latter case, it might be possible that the upper fragment simply escaped from the gel after running for too long.

Another test that is performed is the deposition of the construct onto a gold surface following the protocol given in section C.2.3, followed by the hybridization of the complementary strand OL57 (see Fig C.2. This strand is modified by the attachment of a fluorescent dye, atto 565, at the 5' end, see Fig. C.3. This dye can be excited on the fluorescence microscope, a signal indicating the presence of DNA on the surface. As the next section will explain in detail, observation of fluorescence signal is not done without some surprise in this case. However a signal can be seen nonetheless. Repeating the ligation of the Hyperdrive by the enzyme BbsI in situ (meaning with the construct bonded to the gold) sees this fluorescence signal disappear. This is further proof that the assembly of the Hyperdrive is successful with the protocols given in Appendix C.

5.3 Microscopy Measurements

The gold samples used in all the experiments consist of microscope coverslips cleaned following the procedure of section C.2.3. They are then covered with a 5nm layer of Titanium and a 15nm layer of gold by molecular beam epitaxy. This is done by the STnano Platform of IPCMS. The thin metal layer (20nm) doesn't completely absorb the light and the samples can be observed using an inverted microscope setup. Observation are made using the material of the microscopy platform of ICS. The microscope used is Nikon Eclipse TE200 coupled with Nikon HB-10101AF super high pressure Mercury Lamp. The excitation of the atto 565 dye used in the experiments is made with the use of a filter between 559 and 630 nm coupled with a dichroic mirror at 594nm. The effective excitation band is between 559 and 594nm.

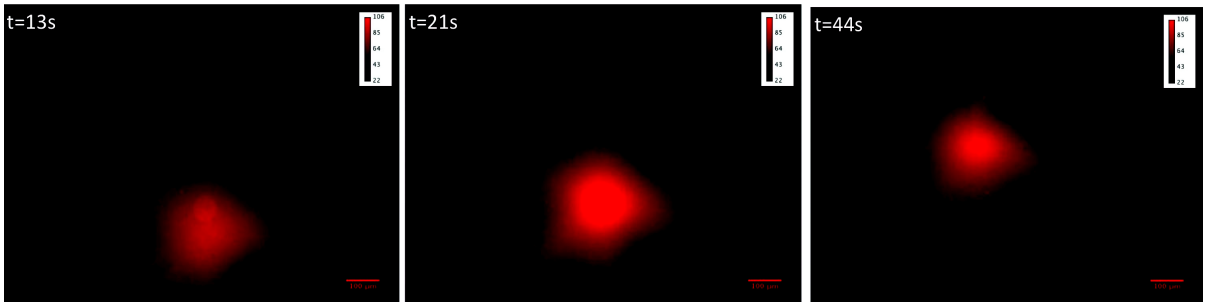

Figure 5.9: A gold surface coated with florescently labeled DNA strands shows a moving "blob" of fluorescence upon first illumination.

As mentioned in the previous section, the observation of a fluorescence signal on the surface is not without any difficulty. The main one is the phenomenon shown in Fig. 5.9. When a surface covered with fluorescently labeled DNA is illuminated by the excitation

light, a fluorescent "blob" appears. In most of the cases, it slowly decays in intensity while moving across the surface of the field of view. It is known that the fluorescence signal of dyes can be quenched in the vicinity of metal surfaces [115, 116, 114, 117, 113] but such a behaviour has never been reported in the scientific literature read on the subject. The signal rises in intensity over 1 to a few seconds and then slowly decays while moving like some sort of DNA fluorescence autowave. The response of the atto 565 dye should be instantaneous (see C.2) compared to the sampling frequency of the camera used and yet the rise of the signal is observed. Moreover, the movement of the "blob" is not consistent, sometimes going left, sometimes right or up or down.

This phenomenon resisted multiple changes of experimental protocol. Among them was the replacement of the Hyperdrive construct for a simple ssDNA modified with a thiol group - still complementary to OL57, the change of fluorescent dye for one of the same family, atto 488. This dye was excited with another filter of the microscope (with an excitation band between 450 and 490nm). In these case, no signal at all was initially observed. Pushing the sensitivity of the camera to its limit, a very weak signal showing a considerably weaker "blob" was observed.

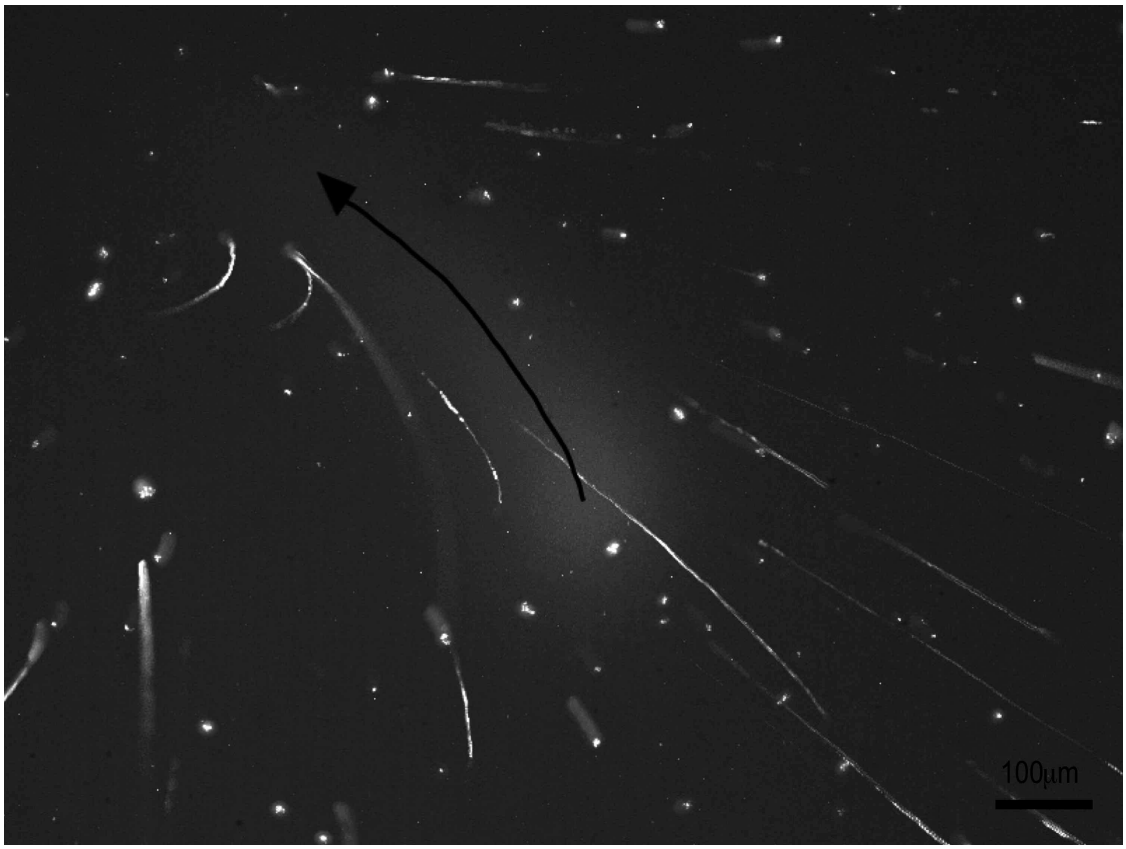

Figure 5.10: A fluorescent "blob" moving on the surface attracts fluorescent particles suspended in solution along its path. Image obtained through summation of multiple successive frames of a recording.

A hint towards an explanation of the problem is shown in Fig. 5.10. In this experiment, the protocol of section C.2.3 is used to graft ssDNA on the surface, followed by the original atto 565 dye. Fluorescent tracers (Spherotech Fluorescent yellow particles, 1μm in diameter) are suspended in the solution. Their absorption spectra are not optimal for the excitation range provided by the filter but they can be seen at the same time as the "blob" is triggered. Fig. 5.10 shows the sum of multiple frames of a short movie in which a "blob" is triggered. The black arrow follows the trajectory of the "blob". Summing the images shows clearly the trajectory of the tracer particles over time. They seem to follow the same trajectory as the "blob" as if both the particles in the fluid and the DNA wave on the surface are attracted by a common object. The extension of the effect of the illumination to the liquid above the gold points toward hydrodynamic effects.

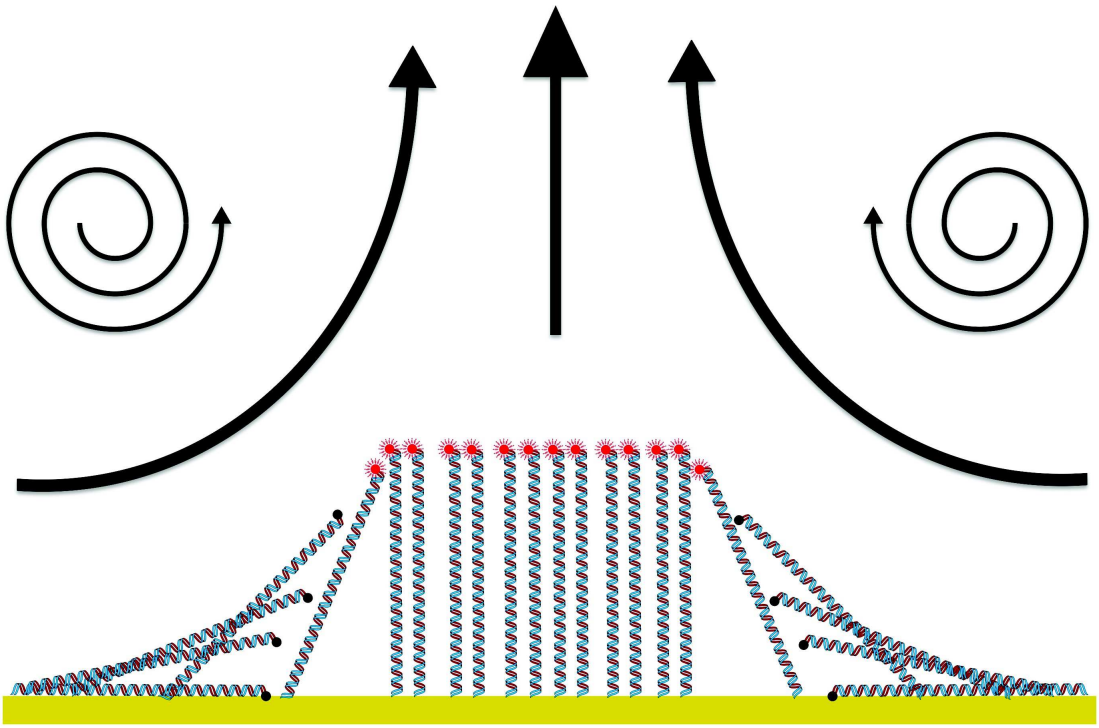

Figure 5.11: The heating of the gold surface by the illumination induces convection cells in the fluid above. The DNA strands initially lying on the surface whose fluorescence is quenched are lifted by the resulting flow and thus emit a fluorescence signal.

A possible explanation of the "blob" phenomenon is depicted in the cartoon of Fig. 5.11. The heating of the gold surface caused by the absorption of the excitation light causes convection flows in the fluid above, in a manner typical of Rayleigh-Bénard cells [122, 121, 123]. The DNA strands that are initially randomly distributed are generally lying on the surface are lifted upward from the flow and the previously quenched dye can emit a fluorescence signal. The erratic behaviour of the "blob" can be attributed to the boundary conditions of the observation chamber. Unless the field of view is exactly in the center of the chamber, the push from the liquid coming towards the center of the convection cell is different from all side and thus pushes the "blob" in a given direction. This

also explains the fact that the effect is less pronounced with the atto 488 dye. The gold absorbs more energy in the range 559-594nm than in the range 450-490nm and so the heat generated by the illuminated is greater in the former case.

Knowing that the effect is probably only due to the gold can be checked by removing the DNA entirely. The fluorescent particles used previously are opaque enough to be seen in white light and are perfect tracers. Using two consecutive images of an acquisition of the flow and using the particles as tracers, a particle image velocimetry (PIV) analysis of the flow can be made. It is done using the PIV analysis plugin of ImageJ. The result is shown in Fig. 5.12.

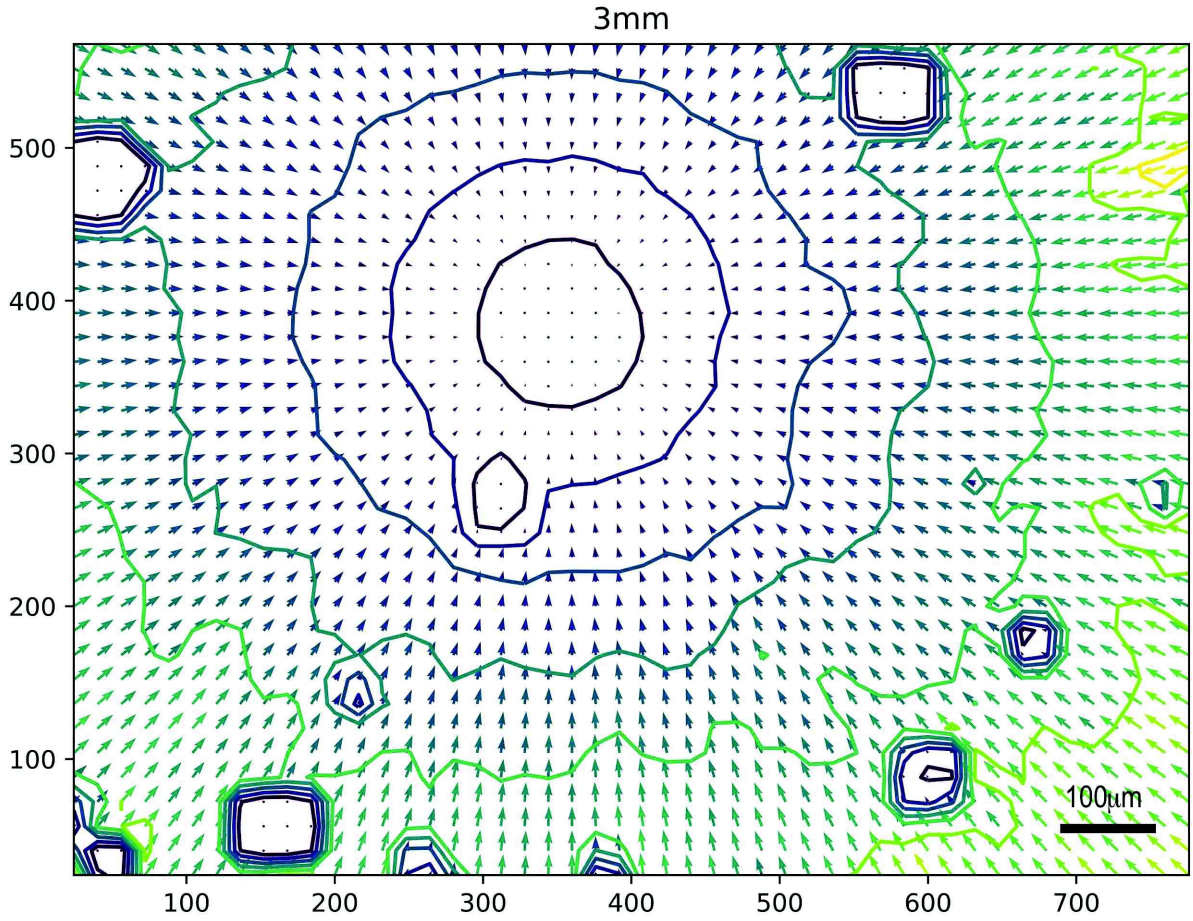

Figure 5.12: PIV analysis of the convection flow triggered by the illumination from two subsequent frames of an acquisition, 3mm above the gold surface. The solid lines are constant velocities, the histogram of the velocities is given in Fig. 5.13. The ”eye of the storm” shows the center of the illumination spot.

In this figure, the sample consists of a freshly cleaned gold slide on top of which an observation chamber filled with water is placed. PIV analysis is used to obtain instantaneous velocity measurements of tracer particles in a fluid. It is done by assuming that for sufficiently small particles and for a small interval between the two pictures, the particles follow

the dynamics of the whole flow being studied. The velocity of the particles starts from zero at the level of the surface and rises the higher they are observed. The figure presents data for an altitude of 3mm above the surface, this is the maximum that could still be traced accurately with the available objectives. The particles are all clearly converging towards an unique point at which they shoot upward, exiting the observation plane. This point is assumed to be the center of the illumination spot. Typical velocities of the flow are given in the histogram of Fig. 5.13. These velocities reach up to 80 μm per second in some spots of the field of view. This is the same order of magnitude as plasmon-induced flows reported in some studies [118, 120] (in the recent fields of "plasmofluidics" and "thermoplasmonics"). In the case of the present observations, the conditions to produce plasmons at the surface of the gold are not met since the illumination comes at 90° to the surface. To explain the high velocities, the hypothesis is made that the very thin metal layer allows for a very high volumic heat transfer that can in turn heat the liquid locally and generate strong flows.

Looking at some examples of "thermoplasmonics" [119], it is interesting to see if the flows observed here can be directed by controlling the geometry of the gold deposits. This is done in early steps by patterning two disks (500μm in diameter and 1mm appart edge to edge) on the surface of a microscope coverslip as shown in Fig. 5.14. This figure depicts the initial and final state of the surface between a 28 minutes long illumination of the gold. This example is enough to show that even with this simple geometry, an interesting effect is obtained. During the course of the illumination, some tracer particles are "trapped" on the line linking the disk at the surface level.

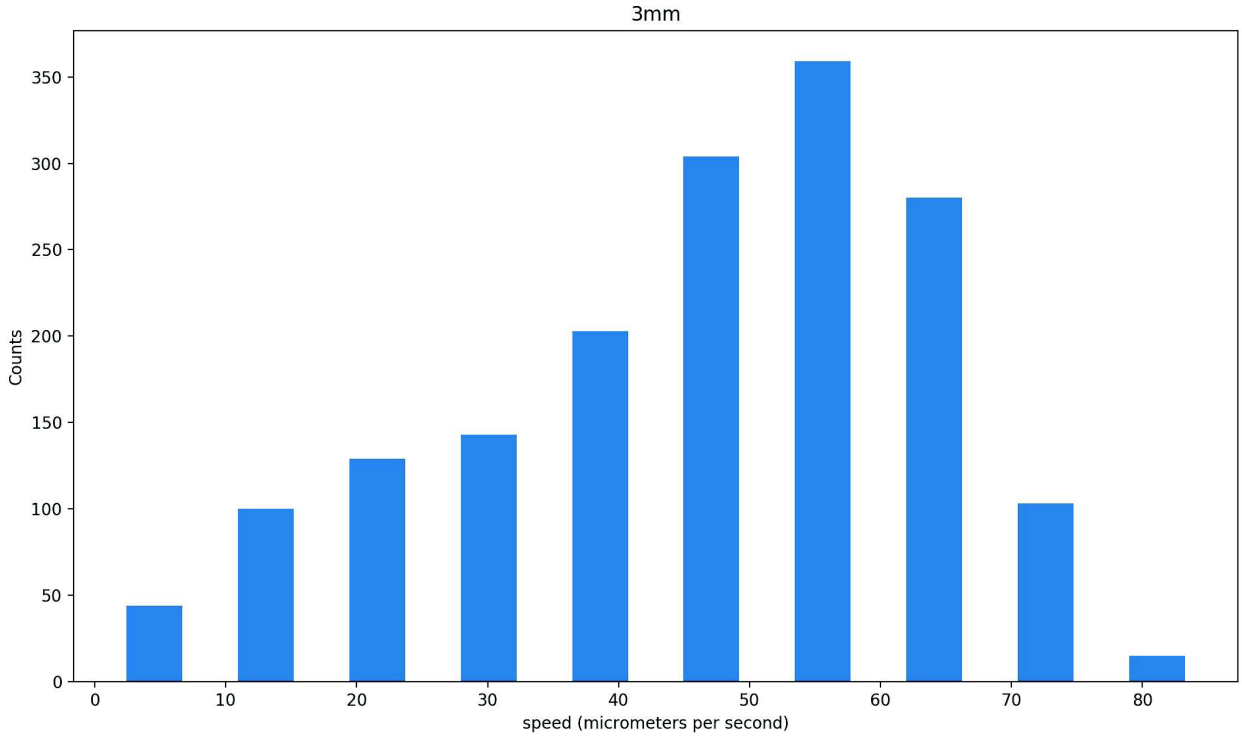

Figure 5.13: Histogram of the velocities represented in Fig. 5.12. Starting from zero velocity at the surface, the flow goes up to dozens of μm/s at 3mm above the surface.

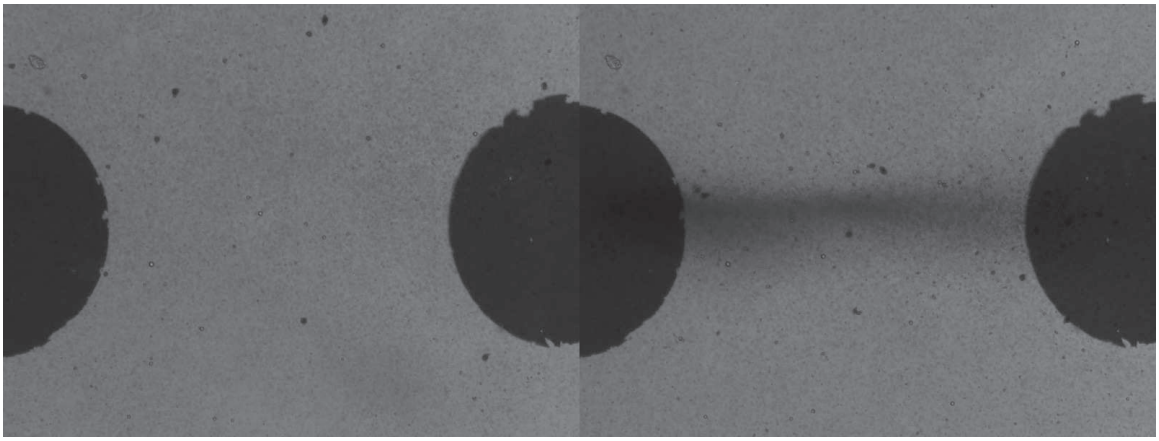

Figure 5.14: Glass slide with two disks of gold (500μm in diameter, 1mm apart edge to edge). Left : at the start of the illumination. Right : after 26 minutes of continuous illumination. The convection flow induced by the two disks gathers the tracer particles on the line linking them.

It is possible to perform another PIV analysis on this system, see Fig. 5.15. This shows a different behavior than for the infinite gold surface (relative to the size of the illumination spot. The upward lift of the convection cell is no longer localized in a spot but in the line linking the two disks. The flow is also weaker and the height of the convection cell can be estimated at around 1mm in height. Measures have been done with incremental steps of 100μm for the surface to a height of 1.5mm. Fig. 5.15 shows the altitude of 200μm and 1mm that seem to be equidistant from the inversion height. On the left side, the tracer particles are attracted toward the center while on the right side they are moving away from it.

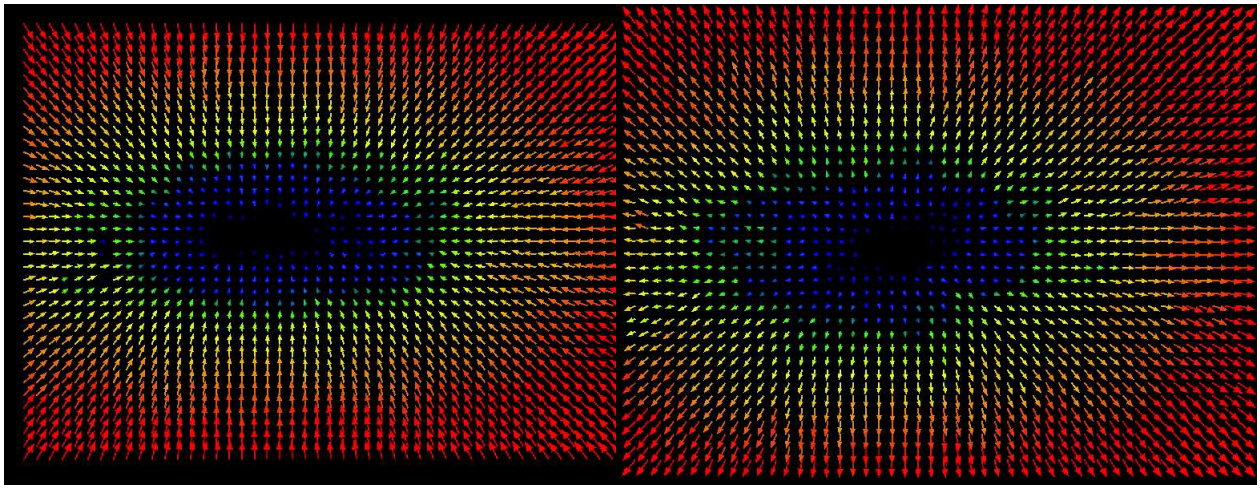

(a) 200 μm above the surface. (b) 1mm above the surface.

Figure 5.15: PIV analysis of the flow induced by the two gold disks (calculated by the ImageJ pluggin). They show an inversion of the flow between 0.2 and 1mm above the surface.

The success achieved with the first simple pattern hints towards interesting developments. Many different shapes and patterns can be explored but perhaps the most interesting ones are those that present some chirality. One can hope to actually drive the flow in a precise manner and one day create vortexes with this simple effect.

5.4 Conclusion

This chapter presented the experimental developments made on three different projects : the confotronic fiber, the Hyperdrive nanomotor and the accidental light-induced convection flow. The short presentation made here hid away all the setbacks encountered on the way to present only the final results and protocols. Starting from zero without any prior knowledge in the fields of molecular biology and microscopy was certainly a difficult task but it made for a wonderful journey full of interesting discovery.

A more seasoned experimentalist might not have spent so much time on this bizarre "blob" phenomenon, missing out on the light-induced flows. In the present state, these projects are only awaiting manpower to be directed in new directions. The confotronic fiber might soon be an artificial axon while gold patterning on surfaces might be the key to easy, externally driven, precise flow in solutions. As for the Hyperdrive which was the key project of this part, the tanglotron [91, 92] already showed that the coupling of the nanometer and the micrometer scale is possible, it is only a matter of time before more complex nanomachines are realized.

Chapter 6

Conclusion and Perspectives

This manuscript is all about movement and how smart materials and designs can be used to build new types of machines. By proposing a new paradigm of motion, motorizing soft materials with zero elastic-energy modes (ZEEMs), this work succeeds in reinventing the "wheel within the material".

In chapter 2, the general concept of a ZEEM is proposed and explored through several examples. A ZEEM is a fluid-like, hydrodynamic mode of deformation that can appear in an elastic material when the symmetry of the system is broken. This mode can then actively be driven out-of-equilibrium by an external source of energy to produce a new kind of motion that leaves the shape and the elastic energy of the system unchanged. ZEEMs are ubiquitous in nature and can be observed in the universal joint reshaping of the bacterial flagellum hook, the wobbling motion of microtubules and in the propulsion of the bacterium spiroplasma. Macroscopic examples are the sliding of the kink in a Möbius strip, the orientation of plants towards the brightest light source and the simple rolling-like motion of a spaghetti in contact with a hot pan. In order for an elastic object to display a ZEEM, it must bear internal prestrains that lead to a symmetry breaking. To generate active motion along the ZEEM, a flux of energy is needed to drive the system. This represents a new class of motion involving continuum material deformations that can be actively driven by dissipative self-organization.

These new soft machines are then exemplified with the case of the toroidal fiberdrive and the linear fiberboid, two systems driven by ZEEMs that exhibit unidirectional and bidirectional motion respectively. The fiberdrive consists of a single piece of polymer fiber closed into a ring. From its topology, the torus bears geometrical prestrains that lead to the emergence of a ZEEM, the "embedded wheel". For the fiberboid in contrast, the ZEEM is self-organized through the coupling with the external driving force. A theoretical model using simple physical considerations explains the phenomenon by the elastic properties of the material as well as dissipation mechanism and the response to a heat stimulus.

Chapter 3 is focused on the experimental demonstration of the ZEEMs-driven soft motors. Using mundane and commercially available polymers such as fishing lines and spaghettis, working examples of both the fiberdrive and the fiberboid are studied. Using the right preparation method and experimental conditions, toroidal fiberdrive can be

shown to turn in one way or the other depending on the material used. Spiral fiberdrives capable of performing work and storing residual thermal energy in the form of torsional elastic energy are built. Finally, linear fiberboids capable of turning at angular frequencies up to 20 Hz are studied.

Both from the theoretical description and ongoing experiments, it is clear that fiberdrives and fiberboids can be driven by other source of energy than thermal gradients. Some slow working examples of fiberboids driven by water gradients are already available and the synthesis of light-sensitive fibers is ongoing. The interesting collective behavior of bundles of fiberboids is still to be studied in depth and the examples studied in this thesis are simply the simplest ZEEM-embedded geometries. This paves the pay for the conception of more complex ZEEM-driven soft machines in the near future.

Chapter 4 introduces the idea of confotronics that can be viewed in parallel with the concept of ZEEMS as general concept of nature. It can be summarized as the study of large systems composed of individually switchable units that cooperate to create collective behaviour on a large scale. The basic motifs of confotronics are defined through the study of natural examples such as DNA and biofilaments in the cell. They are then expanded with the design of a synthetic confotronic fiber made out of interconnected Holliday junctions.

Previous works in the field of DNA nanotechnology and electrically-actuated DNA layers on gold surfaces as well as the example of the tanglotron nanomotor studied in the group before this PhD thesis serve as a motivation and an inspiration for the main experimental project - a DNA-based rotary nanomotor, the Hyperdrive. It combines all the precedent ideas in one. The core of the design is a Holliday junction, whose migration is directed through the application of a potential between two electrodes. The motor is linked to a microscopic structure to transmit the rotation for the nanoscale to the microscale in the same manner as the tanglotron.

Finally, the last chapter describes the current state of progress of the ideas presented in chapter 4. A confotronic dimer is synthesized and studied with molecular biology techniques. In the same way, the Hyperdrive is constructed and analyzed, it is confirmed that it can be assembled and successfully grafted onto a gold surface. The most interesting discovery is the generation of convection flow within the observation cell in the present experimental conditions. The combination of a very thin metal layer with the right range of excitation creates flow with velocities of dozens of micrometers per second.

Although the actual results are not numerous, each individual project is now ready for the next stage of development. The know-how acquired for the synthesis and assembly of DNA structures will make the transition from the dimer to the n-mer confotronic fiber much easier, with the prospect to study it in the new scope of magnetic tweezer measurements. Given the successful assembly of the Hyperdrive, the next step is to start the electrical characterization, in conditions where the ”blob” phenomenon is avoided. For the latter, the prospect of patterning the surface to create directed flow is very interesting and opens

up ideas for an entire project dedicated to the study of light-induced convection flows.

Appendix A

Characterization of the Nylon Fibers

A.1 Mechanical Characterization of Nylon Fibers

Dynamic mechanical thermal analysis (DMTA) tests were carried out with an Instron E3000 dynamic tensile machine by Leandro Jacomine in the mechanics lab of Institut Charles Sadron. Cylindrical filament samples of nylon-6 of 0.8 mm diameter were clamped into the sample holder. The temperature was varied from 30 to 190°C in steps of 20°C. During the DMTA tests, twenty-seven logarithmically spaced sinusoidal waves were employed at frequencies between 0.1 and 8.93 Hz. A strain control was used during tests with minimum and maximum strain levels of 3.10^{-3} and 5.10^{-3}, respectively.

Fig. A.1 shows the storage modulus, E', and the loss modulus, E", for the used nylon- 6 as a function of frequency for different temperatures. In the relevant temperature range for the elasto-rotation experiments (130-190°C), both moduli are almost frequency-independent, implying a constant loss tangent.

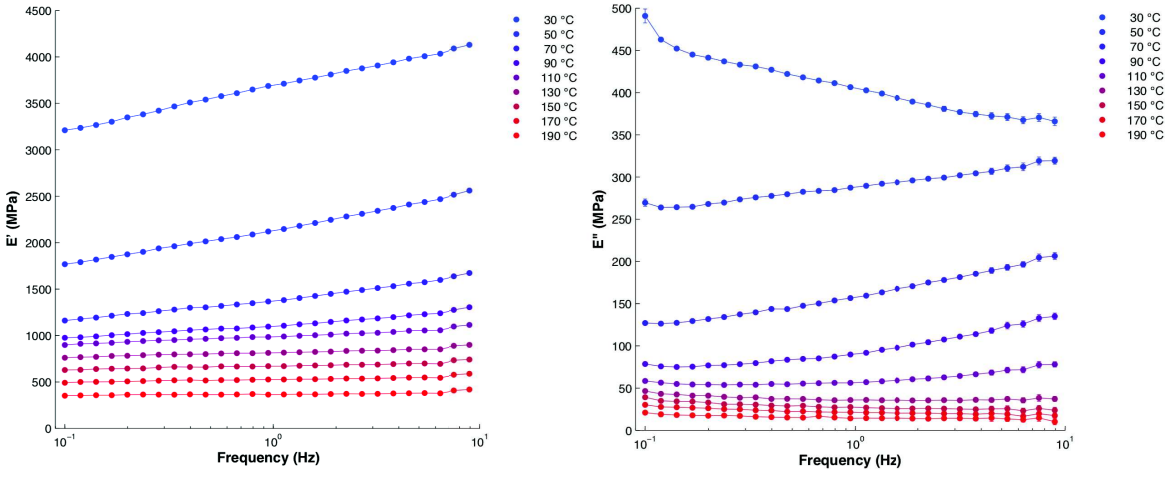

Figure A.1: Mechanical characterization of nylon-6 fibers. Left: The storage modulus vs. frequency for temperatures from 30 to 190°C. Right: The loss modulus vs. frequency for the same temperature range.

A.2 Structural Characterization of the Nylon Fibers

The structural characterization of the samples was carried out by Antoni Sánchez-Ferrer from ETH Zürich. In order to analyze the structural features of the fibers, their crystallinity and anisotropy, wide-angle X-ray scattering (WAXS) experiments were performed using a Rigaku S-MAX3000 equipped with a Rigaku MicroMax-007HF copper rotating anode generator (12 kW, 40 kV, 300 mA) with radiation of wavelength $\lambda_{CuK\alpha} = 0.15418$ nm. The scattering intensities were collected by a Fujifilm BAS-MS 2025 imaging plate system (20 cm x 25 cm, 50 μm resolution) and a 2D Triton-200 X-ray gas-filled multi-wire detector (120 mm diameter, 100 μm resolution). An effective scattering vector range of $0.1\ \text{nm}^{-1} < q < 25\ \text{nm}^{-1}$ was obtained, where q is the scattering wave vector defined as $\text{q} = 4\pi sin\frac{\theta}{\lambda CuK\alpha}$ with a scattering angle of 2θ. Samples were placed in a self-constructed holder controlled by a Haake-F3 thermostat.

The 2D WAXS intensity profile of the annealed nylon-6 fiber shows the semicrystalline and anisotropic pattern of the sample at 120 and 185°C (Fig. A.2 a) and b), respectively), while isotropic and amorphous at 240°C due to the melting of the sample as visualized by the isotropic halo in Fig. A.2 c). At 120°C, the sample presents two equatorial (red section), two meridional (green section), and one reflection at 45 degrees (blue section). The same sample at 185°C only shows one equatorial reflection (red section), two meridional (green section), and one reflection at 45 degrees (blue section). At temperatures above 220°C, nylon-6 melts and scatters isotropically.

Nylon-6 is a semicrystalline polymer with a degree of crystallinity of $\chi = 40 - 50\%$ and has three thermal transitions: a transition corresponding to the glass transition of the amorphous domains at $\text{T}_g \simeq 50$°C, and two first-order transitions attributed to an order-to-order transition of the crystals within the sample at $T_{\alpha\gamma} = 175 - 195$°C and to the melting of the crystalline domains at $\text{T}_m = 210 - 220$°C, respectively [124].

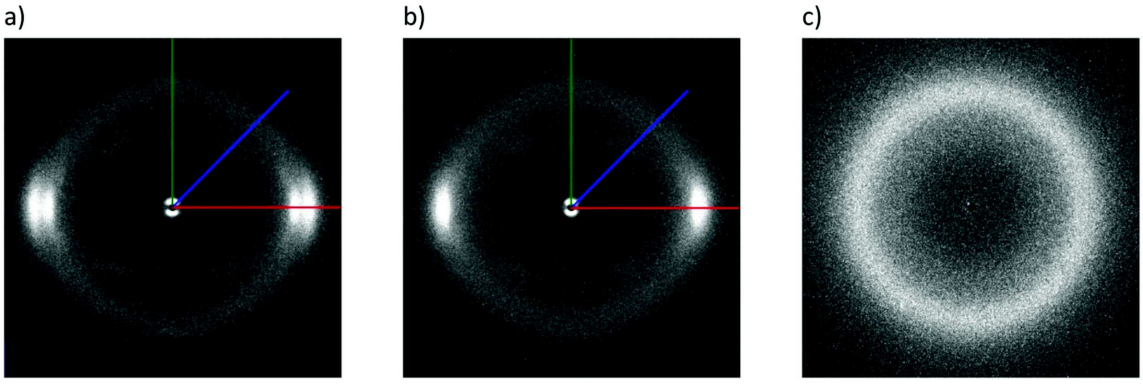

Figure A.2: 2D WAXS intensity profile for the annealed nylon-6 fiber at a) 120°C, b) 185°C, and c) 240°C showing the anisotropy of the signals before melting above 220°C. Note: The fiber axis lies in the vertical direction.

In Fig. A.3, the 1D WAXS intensity profile for the annealed nylon-6 fiber at 120, 185, and 240°C is shown. The sample has different sets of peaks at the three temperatures, i.e.,

$q(120°C) = 7.2, 9.7, 13.5, 14.5, 16.0, 19.1\ nm^{-1}$, $q(180°C) = 7.4, 9.7, 13.2, 15.0, 18.8\ nm^{-1}$, and $q(240°C) = 8.8, 13.5, 17.9\ nm^{-1}$. At 120°C, the two equatorial peaks at $q = 14.5$ and $16.0\ nm^{-1}$ merge together into a single peak at $q = 15.0\ nm^{-1}$ when heated at 185°C, and this peak vanishes when the sample is a melt at 240°C. This change in the WAXS pattern from 120 to 185°C is attributed to a polymorphic transformation from the α-phase to the γ-phase of nylon-6 [125].

The α-polymorphism of nylon-6 [126] corresponds to the monoclinic system ($a = 4.82\mathring{A}$, $b = 4.28\mathring{A}$, $c = 17.45\mathring{A}$, $\gamma = 62.50°$) [127] with the polymer chains interacting in an antiparallel fashion by means of hydrogen bonds [128]. Thus, the average lateral distances between the nylon-6 chains is $d = 4.55\mathring{A}$, while the length of the repeat unit in the polymer backbone is $l = 8.72\mathring{A}$ ($q = 7.2nm^{-1}$). The γ-polymorphism of nylon-6 [126] belongs to the orthorhombic system ($a = 4.86\mathring{A}$, $b = 4.59\mathring{A}$, $c = 16.98\mathring{A}$, $\gamma = 60.38°$), where the interchain average distance is $d = 4.72\mathring{A}$ and the repeat unit length decreases to a value of $I = 8.49\mathring{A}$ ($q = 7.4nm^{-1}$). At temperatures above the melting point, e.g., 240°, nylon-6 has an average polymer-polymer distance of $d = 4.66\mathring{A}$.

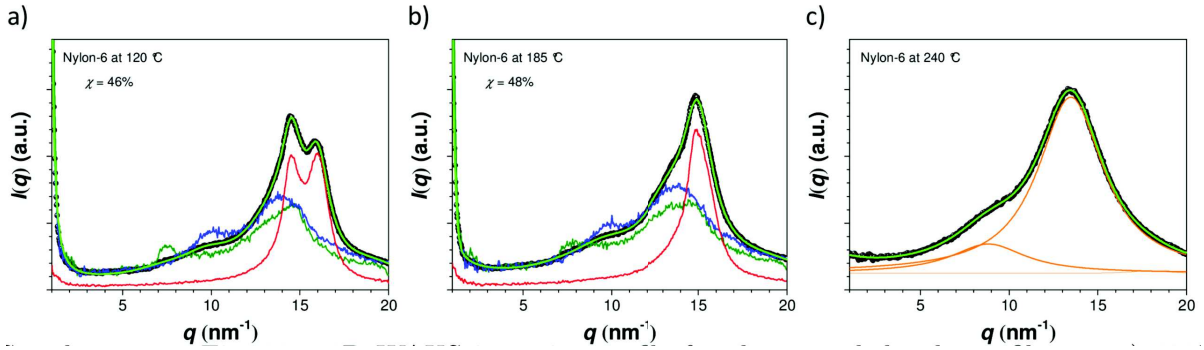

Figure A.3: 1D WAXS intensity profile for the annealed nylon-6 fiber at a) 120°C, b) 185°C, and c) 240°C and the corresponding fitting curve (light green curve). The red (equatorial), blue (45 degrees oblique) and dark green (meridional) curves correspond to the scattering profiles from the sections in Fig. A.2. The orange curves in c) are the amorphous peaks contributing to the signal for the polymer melt.

From the values of the lattice parameters for each polymorphism, both the linear thermal expansion coefficient along the fiber axis, $\alpha_{\parallel}$, and in the cross-section of the fiber, $\alpha_{\perp}$, were calculated. Nylon-6 has a positive value for $\alpha_{\perp} = 4.5 \cdot 10^{-4} K^{-1}$ (expansion factor $1.92 \cdot 10^{-3} \mathring{A} K^{-1}$ and corresponding thermal strain 2.92%) from 120 to 185°C and a negative value for $\alpha_{\parallel} = -4.1 \cdot 10^{-4} K^{-1}$ ($-7.20 \cdot 10^{-3} \mathring{A} K^{-1}$ and -2.68%) from 120 to 185°C. Thus, nylon-6 fibers expand radially while contract longitudinally with an estimated volumetric expansion of $V = 3.03 \cdot 10^{-1} \mathring{A}^3 K^{-1}$ ($4.8 \cdot 10^{-4} K^{-1}$ or 3.09%).

Accounting for the fact that the degree of crystallinity is $\chi = 46 - 48\%$, cf. Fig. A.3, this amounts to an effective thermal expansion coefficient of the nylon-6 fibers along the fiber axis of $\alpha_{\parallel} = -1.93 \cdot 10^{-4} K^{-1}$ and a corresponding strain $\Delta\epsilon = -1.26\%$. To cross check this value, derived from structural data, the longitudinal strain was measured directly (by

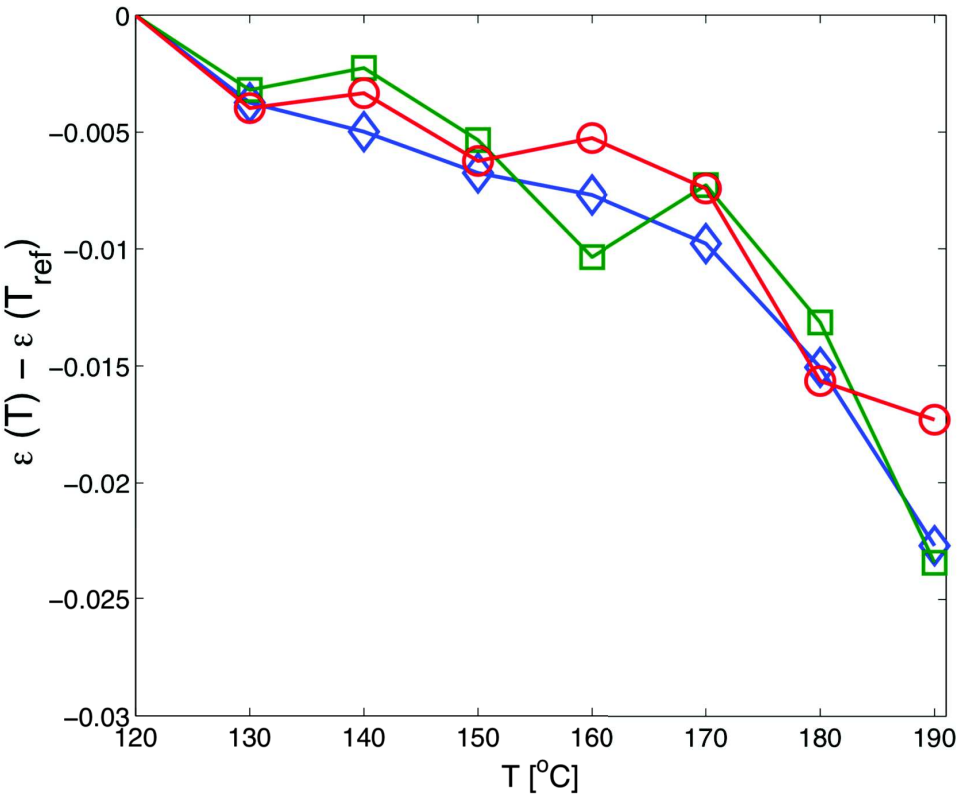

Figure A.4: Relative longitudinal strain of rolling fiber samples with diameters 0.6 mm and lengths between 10 and 12 cm.

video analysis of the fiber's contour length) from rolling fiber experiments, cf. Fig. A.4. In the temperature range from 120 to 180°C, the total strain is about $\Delta\epsilon = -1.5\%$, in rather good agreement with the one found from structural data. Note, however, that the strain (and hence thermal expansion) deviates from linearity.

Both the DMATA analysis and the structural characterization of the samples used in the experimental part of this work were crucial to make the connection between theory and experiments. They permitted to confirm the validity of some of the assumptions made to simplify the calculations, for example the independence of the viscous internal dissipation on the angular frequency in eq. 2.11.

Appendix B

Theoretical Description

In this part, the theoretical considerations that permit the description of the fiberDrive are discussed. It is first shown how temperature gradients in the cross-section of the fiber lead to torque creation if symmetry is broken (i.e. a zero elastic energy mode exists) by the presence of an in-plane curvature. The discussion also brings about self-induced fiber curving as well as the balance of the acting torques. Starting from the thermal diffusion equation with angular advection, the dynamics equations for the temperature gradients are derived. This completes the reduced description, summarized by three equations : the torque balance and the two equations for the thermal gradients/strains in-plane and normal to the plane. Consequently, the stationary rotating solutions of these equations, both for a fiber closed into a circle and for a straight fiber are investigated. Finally, a simple description of the torque creation and energy storage of a fiber forced into a spiral path is discussed.

B.1 Torque Creation, Torque Balance and Thermally -Induced Curvature

The heating plate defines the X-Y plane. When considering a cross section of the fiber, its axis can be laid along the Y direction without any restriction. Hence the fiber's curvature is along the X direction, $\vec{\kappa}.e_x = \kappa_x = \kappa$, defining the laboratory frame

The angle Φ (with respect to the X-axis, cf. Fig. B.1) describes a rotation of the fiber's cross-section around the Y-axis and introduces the co-rotating frame with the internal coordinate system

$$e_1 = (cos\Phi, sin\Phi), e_2 = (-sin\Phi, cos\Phi), \tag{B.1}$$

and the internal coordinates (X',Z') or in polar form $\vec{r}(\rho,\phi)$. Written with respect to these internal coordinates, the curvature is $\vec{\kappa} = \kappa_1 e_1 + \kappa_2 e_2$ and the axial strain in the cross-section (the ϵ_{YY} component of the strain tensor) is

$$\epsilon(\rho, \phi) = -\rho(\kappa_1 cos\phi + \kappa_2 sin\phi) + \bar{\epsilon} - \epsilon_T(\rho, \phi). \tag{B.2}$$

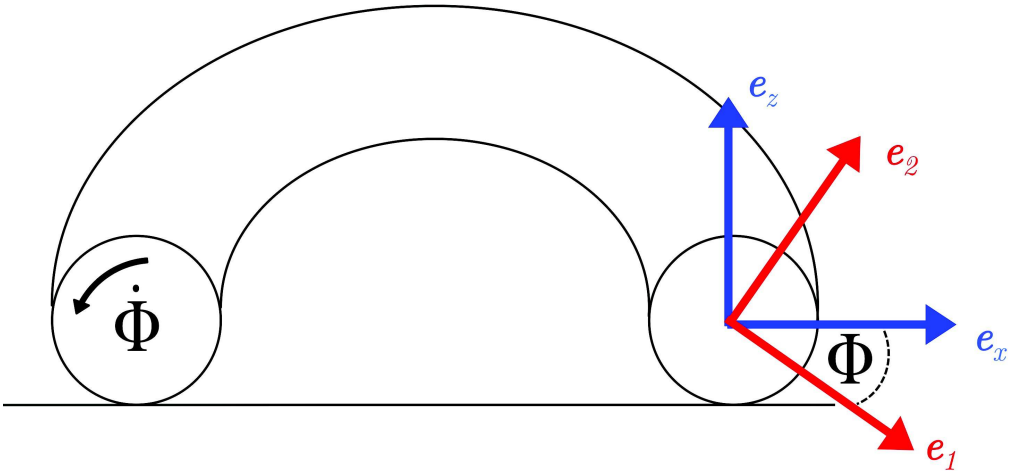

Figure B.1: A fiber confined by its own weight in the X-Y plane. When considering a cross section in the X-Z plane, the curvature can be assumed along the X direction. The co-rotating frame is spanned by the vectors e_1 and e_2, with the angle Φ between e_1 and e_2

The first contribution $-\vec{\kappa}.\vec{r}$ is due to bending, the negative sign indicates compression at the inwards curved side of the cross-section. The second term $\bar{\epsilon}$ is the axial tensile/compressive strain and finally $\epsilon_T(\rho,\phi)$ is the thermal prestrain due to axial thermal expansion/compression. Using $\kappa_1 = \vec{\kappa}.e_1 = \kappa cos\Phi$ and $\kappa_2 = \vec{\kappa}.e_2 = -\kappa sin\Phi$ the strain as a function of the curvature in the laboratory frame κ is

$$\epsilon(\rho,\phi) = -\rho\kappa cos(\phi+\Phi) + \bar{\epsilon} - \epsilon_T(\rho,\phi). \tag{B.3}$$

The elastic energy of the cross-section [37] (that is the energy per length for the fiber) can then be written as

$$E(\kappa,\bar{\epsilon},\Phi) = \frac{Y}{2}\int(-\rho\kappa cos(\phi+\Phi) + \bar{\epsilon} - \epsilon_T(\rho,\phi))^2\rho d\rho d\phi \tag{B.4}$$

$$= \frac{1}{2}B\kappa^2 + \frac{Y}{2}\int(\bar{\epsilon} - \epsilon_T(\rho,\phi))^2\rho d\rho d\phi + Y\kappa\int cos(\phi+\Phi)\epsilon_T(\rho,\phi)\rho^2 d\rho d\phi, \tag{B.5}$$

where Y is the Young's modulus of the fiber and $B = \frac{\pi}{4}YR^4$ is the bending stiffness. The thermal axial prestrain is given by

$$\epsilon_T(\rho,\phi) = \alpha_{\parallel}\Delta T(\rho,\phi), \tag{B.6}$$

with $\alpha_{\parallel}$ the linear thermal expansion coefficient along the fiber axis. With this approximation, the shear in the cross-section as well as the torsional contributions are neglected. For the temperature distribution in the cross-section the following ansatz is made,

$$\Delta T(\rho,\phi) = \Delta T_c\frac{\rho}{R}cos\phi + \Delta T_s\frac{\rho}{R}sin\phi + \Delta T_0, \tag{B.7}$$

introducing the two principal temperature differences or modes ΔT_c and ΔT_s in the rotating frame, and a homogeneous offset ΔT_0. The minimization of the elastic energy in (B.5) with respect to $\bar{\epsilon}$ gives the following relation between the compressive/elongational and the thermal strain

$$\bar{\epsilon} = \frac{1}{\pi R^2} \int \epsilon_T(\rho, \phi) \rho d\rho d\phi. \tag{B.8}$$

This yields $\bar{\epsilon} = \alpha_\parallel \Delta T_0$ upon insertion of (B.6) and (B.7) that is the homogeneous part of the thermal stress is compensated. Inserting everything into the elastic energy and performing the integrals gives

$$E(\kappa, \phi) = B \left\{ \frac{1}{2}\kappa^2 + \alpha_\parallel \frac{\kappa}{R}(\Delta T_c cos\Phi - \Delta T_s sin\Phi) + \frac{\alpha_\parallel^2}{2R^2}(\Delta T_c^2 + \Delta T_s^2) \right\}, \tag{B.9}$$

where the last term has no consequence for the dynamics of κ and Φ.

From there, the driving torque, responsible for generating the motion if it overcomes the prevalent dissipation mechanisms, is then given by $m = -\frac{\partial E}{\partial \Phi}$, i.e.

$$m = B\alpha_\parallel \frac{\kappa}{R}(\Delta T_c sin\Phi + \Delta T_s cos\Phi), \tag{B.10}$$

where $\kappa = \kappa_{ext} = \frac{1}{R_{ext}}$ is the externally imposed curvature of the ring. In the case of an initially straight, linear and open fiber, (B.9) also yields the thermally induced curvature. That is the stationary curvature κ_s entering the driving torque expression in (B.10), neglecting the initial transient reshaping events of the linear fiber. It can be obtained via minimization of the elastic energy with respect to κ, $0 = -\frac{\partial E}{\partial \kappa}$,

$$0 = B\left(-\kappa - \frac{\alpha_\parallel}{R}(\Delta T_c cos\Phi - \Delta T_s sin\Phi)\right) \tag{B.11}$$

$$\rightarrow \kappa_s = -\frac{\alpha_\parallel}{R}(\Delta T_c cos\Phi - \Delta T_s sin\Phi). \tag{B.12}$$

These main results can be simplified by transforming back to the laboratory frame. Since

$$\begin{pmatrix} X' \\ Z' \end{pmatrix} = \begin{pmatrix} cos\Phi & sin\Phi \\ -sin\Phi & cos\Phi \end{pmatrix} \begin{pmatrix} X \\ Z \end{pmatrix}, \tag{B.13}$$

Eq.B.7 can be rewritten as

$$\Delta T(\rho, \phi) - \Delta T_0 = (\Delta T_c cos\Phi - \Delta T_s sin\Phi)\frac{X}{R} + (\Delta T_c sin\Phi + \Delta T_s cos\Phi)\frac{Z}{R} \tag{B.14}$$

$$= \Delta T_x \frac{X}{R} + \Delta T_z \frac{Z}{R}, \tag{B.15}$$

identifying the two main temperature differences or modes ΔT_x and ΔT_z in the laboratory frame. Finally, introducing the thermal strain differences

$$x = \alpha_{\parallel}\Delta T_x, \text{ and } z = \alpha_{\parallel}\Delta T_z, \tag{B.16}$$

the driving torque and the stationary thermally-induced curvature can be written in their most compact form

$$m = B\frac{\kappa}{R}\alpha_{\parallel}\Delta T_z = \frac{\pi}{4}YR^3\kappa z, \tag{B.17}$$

$$\kappa_s = -\frac{\alpha_{\parallel}\Delta T_x}{R} = -\frac{x}{R}. \tag{B.18}$$

In order to write down the balance of torques, the dominant dissipation mechanisms have to be taken into account, and they are different in the case of the closed ring or the open linear filament.

In the case of a closed fiber ring that is forced into a circle of radius R_{ext}, the typical strain is $\epsilon \simeq \kappa_{ext}R = \frac{R}{R_{ext}} \simeq \frac{0.2mm}{2cm} = 10^{-2}$. The mechanical characterization of nylon-6, see (insert relevant figure) is giving in the relevant range of temperature involved in the experiments a storage modulus of $E' = Y = 500 - 800$ MPa and a loss modulus of $E'' = 10 - 30$ MPa. Hence the stress induced by the externally imposed curvature is of the order of $\sigma = E'\epsilon \simeq 5 - 8$ MPa, comparable to the loss modulus, and so internal (viscoelastic) dissipation must be taken into account. The associated dissipative torque can be estimated to be of the order of $m_{dissip} = E''(|\kappa_{ext}|R)R^2$, with E'' the loss modulus, $\kappa_{ext}R$ the strain and an additional R^2 factor coming for the cross-section. It is to be noted that in the relevant temperature range, the loss modulus E'' is independent of the angular velocity and so is the dissipation by extension (cf Fig. A.1).

For the case of the initially straight filament, the thermally induced curving strain cf. (B.16) is very small : $\epsilon \simeq \kappa R = x = \alpha_{\parallel}\Delta T_x \simeq 10^{-4}$. Hence in this scenario, dissipation in the material due to curving in negligible compared to the dominating dissipation mechanism : rolling friction. The dissipative torque due to rolling friction is given by $m_{fric} = C_r\pi R^2\bar{\rho}gR$, where C_r is the coefficient of rolling friction, $\pi R^2\bar{\rho}g$ is the gravitational normal force per length (with $\bar{\rho}$ the density and g the gravitational acceleration) and R is the lever arm. Once again, the dissipation is independent of angular velocity.

Including the driving torque from (B.18) as well as a possible external torque m_{ext}, the general torque balance reads

$$m = m_{fric} - m_{ext}, \tag{B.19}$$

and can be developed into

$$\frac{\pi}{4}YR^3\kappa_{ext}z = E''|\kappa_{ext}|R^3 - m_{ext}, \tag{B.20}$$

for a filament closed into a ring, and

$$\frac{\pi}{4} Y R^3 \kappa_s z = C_r \bar{\rho} g \pi R^3 - m_{ext}, \tag{B.21}$$

for the case of the linear fiber. In the case where rolling is absent, contributions on the right hand side of (B.20) and (B.21) vanish. An interesting observation is that in the absence of external torques acting on the system, the dependence on the radius cancels out in both cases. The main difference that manifests itself more clearly in the dynamic description is that the curvature $\kappa_{ext} = \frac{1}{R_{ext}}$ is imposed by the topology in the case of the ring, while for the straight filament the thermally-induced curvature κ_s is self-organized.

B.2 Dynamics of the Temperature Distribution

In order to close the discussion, dynamic equations for the thermal strain differences as defined in (B.16), that is for the principal temperature differences or modes in the system ΔT_x, ΔT_z are needed. They can be derived from the thermal diffusion equation [129] for the cross-section that is turning with - in the stationary case - constant angular frequency ω,

$$\partial_t T = \frac{D}{R^2} \nabla^2 T + \omega \partial_\varphi T. \tag{B.22}$$

This equation is in the laboratory frame (with (r, φ) the respective polar coordinates, with $\varphi = 0$ at the contact with the plate, i.e. φ is the angle with respect to the Z-axis) and the length is scaled by the cross-section radius R (hence $r \in [0, 1]$). D is the thermal diffusivity of the polymeric material, given by the ratio of thermal conductivity over the specific heat per unit volume, $D = \frac{k_{pol}}{C_{pol}}$. (B.22) has to be considered with the following boundary condition :

$$\frac{l(\varphi)}{R} \partial_r T + (T - T_{ext}(\varphi)) = 0 \text{ at } r = 1, \tag{B.23}$$

where $l(\varphi)$ is a thermal length scale, given by the ration of the thermal conductivity of the material and the heat transfer coefficient, and $T_{ext}(\varphi)$ is the externally imposed temperature.

Perfect thermal contact is assumed at the bottom (contact with the heating plate) and hence $T_{ext} = T_s$ and $l(\varphi = 0) = 0$.

At the top (contact to air), heat transfer to a fluid has to be accounted for and one has $T_{ext} = T_{air}$ and $l(\varphi = \pi) = l_{th} = \frac{k_{pol}}{h}$, where $h = \frac{k_{air}}{d} f(Ra, Pr)$ scales with the diameter $d = 2R$ of the fiber in a complicated fashion involving the Rayleigh number $Ra(d)$ (and Prandtl number Pr) - already for a stationary, non-rotating cylinder. In the present system, the estimation gives $l_{th} \simeq R$.

To capture the main physics, only the dominant modes of the temperature distribution are needed. Therefore a symmetry adapted version of the boundary conditions (at $r = 1$) can be assumed :

$$l(\varphi) = (1 - cos\varphi)\frac{l_{th}}{2}, \tag{B.24}$$

$$T_{ext}(\varphi) = \frac{T_s - T_{air}}{2}cos\varphi + \frac{T_s + T_{air}}{2}, \tag{B.25}$$

This way, one has indeed $l = 0$ and $T = T_s$ at the bottom ($\varphi = 0$) and $l = l_{th}$ and $T = T_{air}$ at the top ($\varphi = \pi$). For brevity, T_{ext} is rewritten as $T_{ext}(\varphi) = T^- cos\varphi + T^+$, where $2T^- = T_s - T_{air} = \Delta T_{ext}$ is the externally applied temperature difference.

A general solution of (B.22) has the form

$$T = C(r)cos\varphi + S(r)sin\varphi + T_0. \tag{B.26}$$

To proceed it is convenient to use a symmetry-adapted polynomial system, namely Zernique-polynomials, which are defined [130] as

$$Z_n^m = R_n^m(r)cos(m\varphi),\ Z_n^{-m} = R_n^m(r)sin(m\varphi), \tag{B.27}$$

with the radial polynomials R_n^m, or explicitely as

$$Z_0^0 = 1, \tag{B.28}$$

$$Z_1^1 = 2rcos\varphi,\ Z_1^{-1} = 2rsin\varphi, \tag{B.29}$$

$$Z_3^1 = \sqrt{8}(3r^3 - 2r)cos\varphi,\ Z_3^{-1} = \sqrt{8}(3r^3 - 2r)sin\varphi. \tag{B.30}$$

The following properties of the Zernique polynomials must be noted (with ∇^2 the Laplacian) :

$$\nabla^2 Z_0^0 = 0,\ \nabla^2 Z_1^{\pm 1} = 0,\ \nabla^2 Z_3^{\pm 1} = 24 Z_1^1. \tag{B.31}$$

By inspection of the ansatz (B.26), one could think that it is sufficient to use only the modes $\propto Z_1^{\pm 1}$. However, to be able to fulfill the boundary conditions, one also needs to account for those $\propto Z_3^{\pm 1}$, hence

$$C(r)cos\varphi = c_1 Z_1^1 + c_2 Z_3^1,\ S(r)sin\varphi = s_1 Z_1^{-1} + s_2 Z_3^{-1}. \tag{B.32}$$

Insertion of (B.32) into the boundary condition of (B.25), using $cos\varphi sin\varphi = \frac{1}{2}sin(2\varphi)$ and $cos^2\varphi = \frac{1}{2}(1 + cos(2\varphi))$, sorting for modes and neglecting modes $m \geq 2$ yields three equations for the unknowns c_2, s_2 and T_0 :

$$0 = \frac{l_{th}}{2R}C'(1) + (C(1) - T^{-}), \tag{B.33}$$

$$0 = \frac{l_{th}}{2R}S'(1) + S(1), \tag{B.34}$$

$$0 = -\frac{l_{th}}{4R}C'(1) + T_0 - T^{+}. \tag{B.35}$$

(B.35) yields

$$T_0 = \frac{l_{th}}{4R}C'(1) + T^{+}. \tag{B.36}$$

(B.34) relates s_2 to s_1, and hence implies that the mode $\propto Z_3^{-1}$ is slaved to the mode $\propto Z_1^{-1}$,

$$s_2 = -gs_1 \text{ with } g = \frac{2\left(\frac{l_{th}}{R} + 2\right)}{\sqrt{8}\left(7\frac{l_{th}}{R} + 2\right)} \tag{B.37}$$

As will be seen shortly, c_{stat} which is proportional to the thermal drive, describes the stationary temperature distribution.

The next step is to insert the ansatz (B.26) and (B.32), with c_2, s_2 and T_0 from above into the thermal diffusion equation (B.22). Then, projecting on the mode Z_1^{-1} by performing $\int_0^1 ...Z_1^{-1}rdr$ of the resulting equation, and analogously by projecting on Z_1^1, one gets equations for s_1 and c_1 as follows :

$$\dot{s}_1 = -\frac{24D}{R^2}gs_1 - \omega c_1, \tag{B.38}$$

$$\dot{c}_1 = -\frac{24D}{R^2}gc_1 + \frac{24D}{R^2}gc_{stat} + \omega s_1. \tag{B.39}$$

Inspecting the ansatz Eq.B.26 and the definition of φ, c_1 corresponds to ΔT_z and s_1 to ΔT_x and hence the dynamics of the temperature field can be written in the following simple form :

$$\frac{d}{dt}\Delta T_x = -\frac{\Delta T_x}{\tau} - \omega \Delta T_z, \tag{B.40}$$

$$\frac{d}{dt}\Delta T_z = q - \frac{\Delta T_z}{\tau} + \omega \Delta T_x. \tag{B.41}$$

Here τ is the characteristic time scale of the thermal relaxation. The mode ΔT_z is in addition driven by the thermal pumping, with q the pumping rate. Explicitely they are given by

$$\tau = \frac{R^2}{24Dg} = \frac{R^2}{24D}\frac{\sqrt{8}\left(7\frac{l_{th}}{R}+2\right)}{2\left(\frac{l_{th}}{R}+2\right)}, \tag{B.42}$$

$$q = \frac{24D}{R^2}gc_{stat} = \frac{24D}{R^2}\frac{\Delta T_{ext}}{\sqrt{8}\left(7\frac{l_{th}}{R}+2\right)} \tag{B.43}$$

Considering (B.40) and (B.41) for the case without rotation ($\omega = 0$), one gets for long times $\Delta T_x = 0$ and $\Delta T_z = q\tau = c_{stat} = \frac{\Delta T_{ext}}{2\left(\frac{l_{th}}{R}+2\right)}$, which is the expected solution in this case.

To sum it up, introducing the thermal strains $x = \alpha_{\parallel}\Delta T_x$ and $z = \alpha_{\parallel}\Delta T_z$, and the effective thermal drive $p = \alpha_{\parallel}q$ gives the following equations :

$$\dot{x} = -\frac{x}{\tau} - \omega z, \tag{B.44}$$

$$\dot{z} = p - \frac{z}{\tau} + \omega x. \tag{B.45}$$

Together with the torque balance, in case of a rotating circular fiber given by (B.20),

$$\frac{\pi}{4}YR^3\kappa_{ext}z = E''|\kappa_{ext}|R^3 - m_{ext}, \tag{B.46}$$

and in the case of a rolling straight fiber, (B.21) with κ_s given by (B.18),

$$\frac{\pi}{4}YR^3\kappa_s z = C_r\bar{\rho}g\pi R^3 - m_{ext},\ \kappa_s = -\frac{x}{R}, \tag{B.47}$$

the dynamics is completely determined.

B.3 Onset of Motion

B.3.1 Fiber Closed to a Circle

In this case, one looks for solutions to the steady-state equations

$$\frac{\pi}{4}YR^3\frac{z}{R_{ext}} = m_{dissip}(\omega) - m_{ext}, \tag{B.48}$$

$$0 = -\frac{x}{\tau} + \omega z, \tag{B.49}$$

$$0 = p - \frac{z}{\tau} + \omega x, \tag{B.50}$$

where the externally prescribed curvature $\kappa_{ext} = \frac{1}{R_{ext}}$ is inserted and where the dissipative torque is given by $m_{dissip}(\omega = 0) = 0$ and $m_{dissip}(\omega \neq 0) = \frac{E''R^3}{R_{ext}}$ for internal

viscoelastic dissipation. The trivial solution (for $m_{ext} = 0$) is given by $\omega = 0$, $x = 0$ and $z = p\tau$. It is important to note that the left hand side of the torque balance is finite, indicating that a fiber closed to a ring is under prestrain.

For $m_{ext} = 0$, the torque balance gives a stationary value for the strain difference normal to the plane, $z_s = \frac{4}{\pi}\frac{E''}{Y}$, which is essentially the ratio of the loss modulus with the storage modulus $\frac{E''}{E'}$. In this leading order theory, the dependence on the externally imposed curvature vanishes. The nontrivial solution for ω then reads

$$\bar{\omega} = \sqrt{\frac{\bar{p}}{z_s} - 1} = \sqrt{\frac{\pi}{4}\frac{E'}{E''}\bar{p} - 1}, \tag{B.51}$$

where the frequency and the thermal pumping are scaled by the thermal relaxation time, $\bar{\omega} = \omega\tau$ and $\bar{p} = p\tau$. This set of solutions for ω exists when the argument of the square root becomes positive, i.e. for $\bar{p} > \bar{p}_c = z_s = \frac{4}{\pi}\frac{E''}{E'}$ or

$$(\alpha_{\parallel}\Delta T_{ext})_c \simeq \frac{l_{th}}{R}\frac{E''}{E'} = \frac{k}{hR}\frac{E''}{E'}. \tag{B.52}$$

The onset of motion is hence supercritical (continuous or second order) cf. Fig. 2.9, in agreement with the experimental measurements cf. Fig. 3.3 in the main text.

The torque-velocity relation for a fiber closed to a ring can also be obtained from (B.48) to (B.50) by solving for m_{ext} and reads

$$m_{ext} = \frac{\pi}{4}Y\frac{R^3}{R_{ext}}\left(z_s - \frac{\bar{p}}{1+\bar{\omega}^2}\right). \tag{B.53}$$

The torque is proportional to the imposed curvature $m_{ext} \propto \kappa_{ext} = \frac{1}{R_{ext}}$, which hence also holds for the stalling torque.

For the special case of a fiber whose path is constrained into a spiral, the description is conceptually the same as for the closed circle, except that the imposed curvature varies along the arc length ($\kappa_{ext}(s) = \frac{1}{R_{ext}(s)}$), which makes a closed description difficult. For the spirals investigated in this thesis, the curvature does not vary much so a superposition of closed rings is used to describe the system in first approximation, using the mean curvature of the spiral.

B.3.2 Straight Fiber

In the case of the linear fibers, one has to look for nontrivial solutions to the steady-state equations

$$-bxz = m_{fric}(\omega) - m_{ext}, \tag{B.54}$$

$$0 = -\frac{x}{\tau} - \omega z, \tag{B.55}$$

$$0 = p - \frac{z}{\tau} + \omega x. \tag{B.56}$$

where the thermally induced curvature $\kappa_s = -\frac{x}{R}$ is inserted, $b = \frac{B}{R^2} = \frac{\pi}{4} Y R^2$ and the dissipative torque is given by $m_{fric}(\omega = 0) = 0$ and $m_{fric}(\omega \neq 0) = c = C_r \pi R^3 \bar{\rho} g$ for rolling friction. the trivial solution (for $m_{ext} = 0$) is again given by $\omega = 0$, $x = 0$ and $z = p\tau$. As the torque balance is fulfilled identically, the open filament is torque free.

It can be shown that for $m_{ext} = 0$ nontrivial solutions exist if

$$\bar{\omega}^2 - \sqrt{\frac{b}{c}} \bar{p} \sqrt{\bar{\omega}} + 1 = 0, \tag{B.57}$$

where the frequency and the thermal pumping are gain scaled by the thermal relaxation time scale, $\bar{\omega} = \omega\tau$ and $\bar{p} = p\tau$. For sufficiently large drive (precisely for $\bar{p} > \bar{p}_c = \frac{4}{3} 3^{\frac{1}{4}} \sqrt{\frac{c}{b}} \simeq 1.755 \sqrt{\frac{c}{b}}$), two branches of finite ω-solutions emerge, one stable and one unstable. The frequency at threshold is finite, $\omega_c = \frac{1}{\sqrt{3}}$. Hence the onset of motion is subcritical (i.e. discontinuous or first order), cf. Fig. 2.11, again in agreement with the experiments cf. Fig. 3.9 and Fig. 3.14. The difference in the characteristics of the onset of rolling motion for a fiber closed in a circle (continuous) as opposed to a straight fiber (discontinuous) lies in the fact that in former case, the symmetry is already broken by the externally imposed curvature, while in the latter this is achieved via transient thermal curving. Omitting numerical factors, the following scalings for the self-propelled rolling motion can be concluded, the frequency at onset scales as

$$\omega_c \simeq \frac{D}{R^2}. \tag{B.58}$$

It can be shown that for large driving, the scaling is even $\omega_c \simeq \frac{1}{R^{\frac{7}{3}}}$. This is stronger than the experimentally measured dependence of the frequencies (cf. Fig. 3.16) which yields $\omega \simeq R^{-n}$ with $n = 0.75$. This discrepancy can be explained by the deviations from the perfect fiber shape leading to slower angular velocities (see subsection 3.3.2). For the effective thermal drive at onset, $p_c = \frac{1}{\tau} \sqrt{\frac{c}{b}} = \frac{D}{R^2} \sqrt{\frac{\sigma_d}{Y}}$, where the dissipative stress associated with rolling friction $\sigma_d = 4 C_r \rho g R$ is introduced. The thermal strain at onset is hence

$$(\alpha_{\parallel} \Delta T_{ext})_c \simeq \frac{l_{th}}{R} \sqrt{\frac{\sigma_d}{Y}} = \frac{k}{hR} \sqrt{\frac{\sigma_d}{Y}}, \tag{B.59}$$

with the heat conductivity $k = k_{pol}$ and the heat transfer coefficient h.

Finally, solving (B.54) to (B.56) for the external torque gives the torque-velocity relation

$$m_{ext} = c - b\bar{p}^2 \frac{\bar{\omega}}{(1 + \bar{\omega}^2)^2}. \tag{B.60}$$

This formula can be used to fit the experimental data of fibers rolling on an inclined plane (cf. subsection 3.3.4 and Fig. 3.15).

Appendix C

Molecular Biology

C.1 List of Reagents and Compounds

C.1.1 List of Reagents

All bioreagents and compounds are purchased from Merck (previously Sigma-Aldrich) unless otherwise specified. They are named and briefly described in Table C.1.

Name	**Description**
1X T4 DNA Ligase Reaction Buffer (from New England Biolabs)	Buffer for the activation of the DNA T4 ligase (50mM TrisHCl, 10mM $MgCl^2$, 1mM ATP, 10mM DTT, pH 7.5 at 25°C).
Acrylamide:N,N'-Methylenebisacrylamide 29:1 solution	Main polymeric components of polyacrylamide gels.
Agarose	Agarose is a neutral polymer component of agar. Heating of agarose gives rise to solution form which on cooling sets into gel form.
APS 25% (Ammonium persulfate)	Widely used reagent in biochemistry and molecular biology for the preparation of polyacrylamide gels. APS forms oxygen free radicals in aqueous solution by a base-catalyzed mechanism.
BbsI-HF® (from New England Biolabs)	Restriction enzyme used to cut dsDNA at a specific sequence.
EDTA (Ethylenediaminetetraacetic acid)	Used for scavenging metal ions in solution and deactivate metal-dependent enzymes.

ETB (Ethidium Bromide)	DNA intercalating agent used for gel visualization.
GeneRuler 1 kb Plus DNA Ladder (from ThermoFisher Scientific)	DNA Ladder recommended for sizing and approximate quantification of a double-stranded DNA in the range of 75 bp to 20,000 bp on agarose gels, see Fig. C.1.
Mercapto-hexanol (MCH) - 6-Mercapto-1-hexanol	Short thiolated carbon chain used to cover gold surfaces.
NaCl (Sodium Chloride)	Monovalent salt used in the preparation of buffers.
NEBuffer^{TM} 2.1 (from New England Biolabs)	Working buffer for the activity of the enzyme BbsI. Components : 50mM NaCl, 10mM Tris-hCl, 10mM $MgCl_2$, 100μg/ml BSA, pH 7.9@25°C
T4 DNA ligase (from New England Biolabs)	Enzyme used to link DNA constructs together.
TAE 10X (Tris/Acetic acid/EDTA)	Buffer solution effective under slightly basic conditions, typically used for gel electrophoresis with agarose gels.
TBE 10X (Tris/Borate/EDTA)	Buffer solution effective under slightly basic conditions, which keeps DNA deprotonated , water-soluble, and protected from degradation.
TCEP (Tris(2-carboxyethyl)phosphine hydrochloride)	Chemical used to break disulfide bonds.
(TEMED) N,N,N',N'-Tetramethylethylenediamine	Used for the preparation of acrylamide hydrogels and sodium dodecyl sulfate-polyacrylamide gels.
Trizma® base	Used for the preparation of Tris-HCl buffer for pH controlled conditions.

Table C.1: List of reagents used in the experiments.

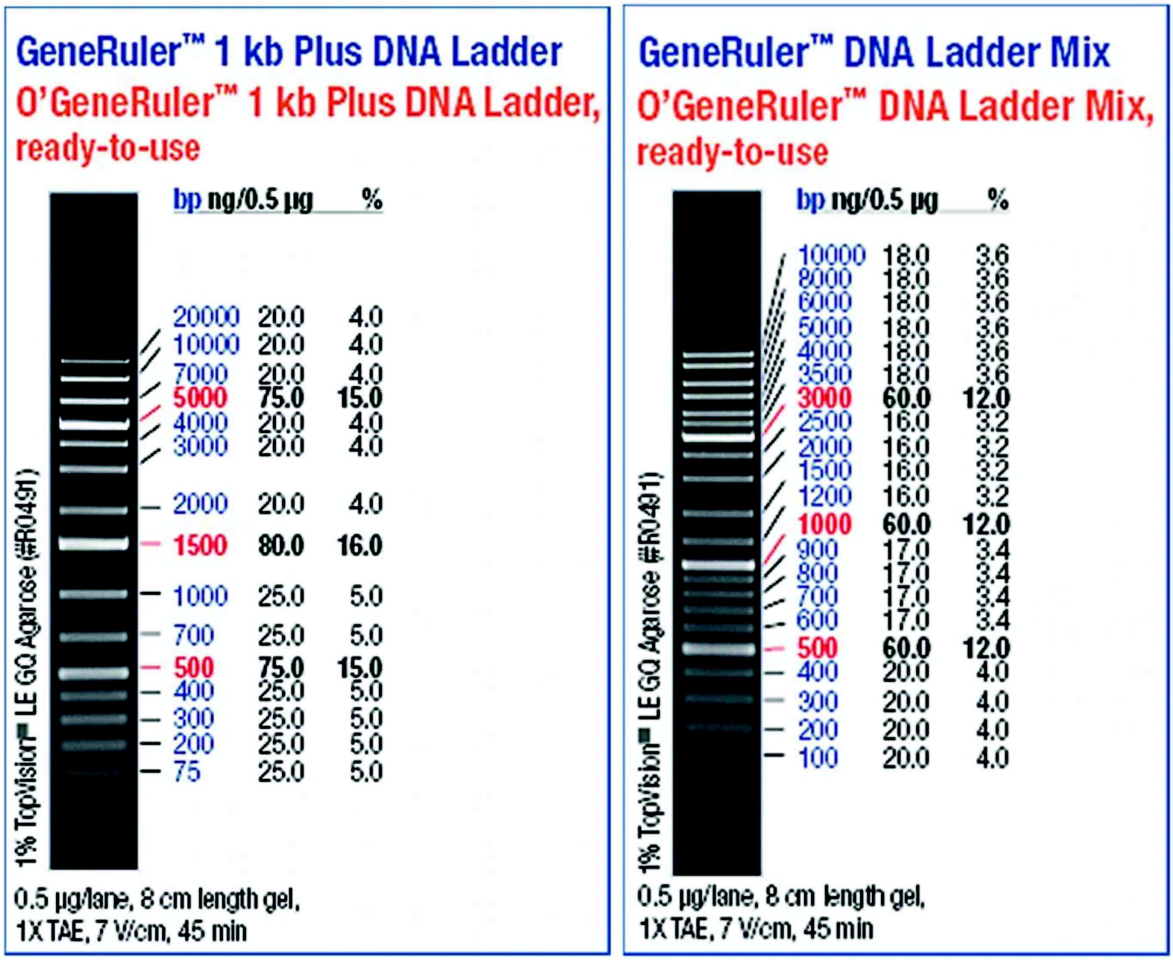

Figure C.1: Description of the bands and fragment sizes for the Gene Ruler DNA ladder, provided by the supplier. Left: Ladder used for the agarose gels. Right : Ladder used for the polyacrylamide gels.

C.1.2 List of Oligonucleotides

The SsDNA strands (oligonucleotides) used in this work are purchased from Microsynth. They are listed in Fig. C.2. The BIO modification refers to a biotin molecule attached at the specified end of the nucleotide. The THIO modification stands for a thiol modification used to link the oligonucleotide to gold. Finally the AT565 modification stands for an Atto 565 molecule, a fluorescent molecule widely used for high sensitivity applications, including single-molecule detection. Information about the dye are given in Fig. C.3 and table C.2.

The oligonucleotides are delivered in a powdered form. They are resuspended in MilliQ water (with the volume specified by the supplier). DNA concentration of the resuspended samples is measured on a Nanovue Plus spectrophotometer from Dutscher and compared with the information given by the supplier.

OL057		Type	DNA	Oligo ID # 2920660		Date	20.06.2017
Purification	HPLC	Length	19	Scale 0.04 umol		Molecular weight	6429.1 g/mol
5' Modification	AT565	3' Modification	NONE	No internal modifications			
Melting Point*	48.9	NNM-Method	45.6	*based on a [Na+] of 50 mM		Millimolar ext. coeff.	190.8
Amount	5.76 OD	Amount	194.1 µg	Amount	30.2 nmol	Volume for 100 µM:	301.9 µl
5'-CGC CTG AGT TTT TTT TTT T-3'							

OL62		Type	DNA	Oligo ID # 3038272		Date	15.11.2017
Purification	HPLC	Length	19	Scale 0.2 µmol		Molecular weight	6051.9 g/mol
5' Modification	THI	3' Modification	NONE	No internal modifications			
Melting Point*	48.9	NNM-Method	45.6	*based on a [Na+] of 50 mM		Millimolar ext. coeff.	225.5
Amount	8.36 OD	Amount	224.2 µg	Amount	37.1 nmol	Volume for 100 µM:	370.5 µl
5'-AAA AAA AAA AAC TCA GGC G-3'							

OL065		Type	DNA	Oligo ID # 3155105		Date	12.04.2018
Purification	PAGE	Length	82	Scale 0.2 µmol		Molecular weight	25400.2 g/mol
5' Modification	NONE	3' Modification	THI	No internal modifications			
Melting Point*	89.8	NNM-Method	79.0	*based on a [Na+] of 50 mM		Millimolar ext. coeff.	822.4
Amount	5.08 OD	Amount	156.8 µg	Amount	6.2 nmol	Volume for 100 µM:	61.7 µl
5'-GAA ACG CTT GCG GAG ATA TAA AAA ACA CTA GAA CCC ACT ACC GTC TTC GCT ATA GAG CCG GCC AAA GGG CCG GCT CTA TAG C-3'							

0L064		Type	DNA	Oligo ID # 3155106		Date	12.04.2018
Purification	PAGE	Length	82	Scale 0.2 µmol		Molecular weight	25706.3 g/mol
5' Modification	THI	3' Modification	NONE	No internal modifications			
Melting Point*	91.9	NNM-Method	81.7	*based on a [Na+] of 50 mM		Millimolar ext. coeff.	828.9
Amount	2.44 OD	Amount	75.6 µg	Amount	2.9 nmol	Volume for 100 µM:	29.4 µl
5'-GCT ATA GAG CGC CGG AAA GCC GGC GCT CTA TAG CGA AGA CGG TAG TGG GTT CTA GTG AAA AAC TCA GGC GGC GTT CGC AAA G-3'							

OL066		Type	DNA	Oligo ID # 3155107		Date	12.04.2018
Purification	HPLC	Length	20	Scale 0.2 µmol		Molecular weight	6663.9 g/mol
5' Modification	NONE	3' Modification	BIO	No internal modifications			
Melting Point*	64.5	NNM-Method	60.3	*based on a [Na+] of 50 mM		Millimolar ext. coeff.	182.4
Amount	17.70 OD	Amount	646.6 µg	Amount	97.0 nmol	Volume for 100 µM:	970.3 µl
5'-CTT TGC GAA CGC CGC CTG AG-3'							

0L067		Type	DNA	Oligo ID # 3155108		Date	12.04.2018
Purification	HPLC	Length	20	Scale 0.2 µmol		Molecular weight	6238.9 g/mol
5' Modification	THI	3' Modification	NONE	No internal modifications			
Melting Point*	56.4	NNM-Method	51.6	*based on a [Na+] of 50 mM		Millimolar ext. coeff.	181.9
Amount	15.08 OD	Amount	517.3 µg	Amount	82.9 nmol	Volume for 100 µM:	829.1 µl
5'-TAT ATC TCC GCA AGC GTT TC-3'							

Figure C.2: Detailed informations about the oligonucleotides used for the Hyperdrive project, bought from Microsynth, provided by the company.

λ_{abs}	564 nm
ϵ_{max}	$1.2 \cdot 10^5$ I/mol.cm
λ_{fl}	590 nm
η_{fl}	90 %
T_{fl}	4.0 ns
$\mathrm{CF}_{260} = \epsilon_{260}/\epsilon_{max}$	0.27
$\mathrm{CF}_{280} = \epsilon_{280}/\epsilon_{max}$	0.12

Table C.2: Optical properties of atto 565

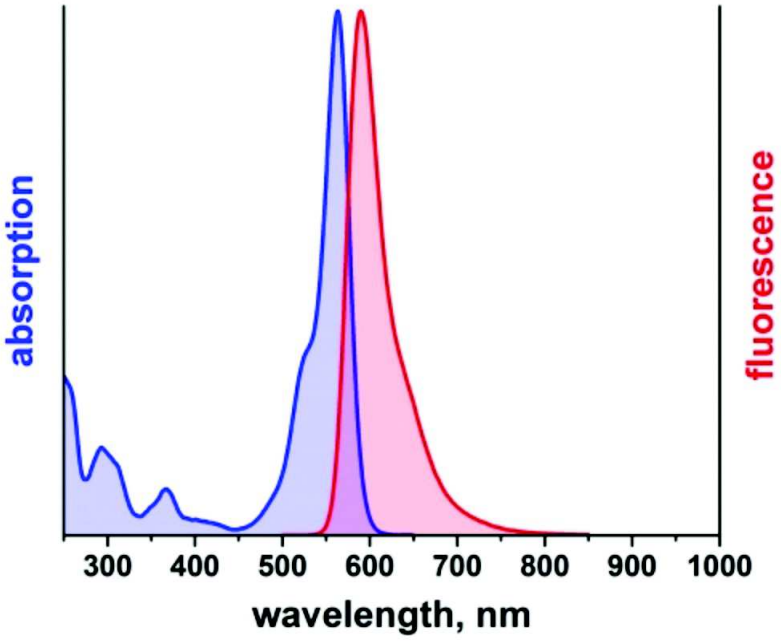

Figure C.3: Emission and absorption spectra of the fluorescent dye atto 565.

C.2 Experimental Protocols

C.2.1 Preparation of DNA samples

Protocol for Annealing Oligonucleotides

Annealing oligonucleotides refers to the process of pairing two ssDNA strands to form a dsDNA complex via pairwise interactions. It is used to form the Hyperdrive construct

starting from the oligonucleotides ordered from Microsynth. The protocol is as follows :

- Mix both ssDNA strands in equimolar quantity in annealing buffer ([TrisHCl]=10mM, [NaCl]=50mM, [EDTA]=1mM, pH=7.3) and heat the resulting solution at 95°C and maintain the temperature for 5 minutes
- Slowly cool down the solution (placing it between the two heating blocks and switching off the heat) to room temperature, at 25?∘C.
- Store the solution in the fridge at 4°C.

Ligation of DNA constructs

For the synthesis of the confotronic fiber (see section 5.1), two individual Holliday junction are linked together via an enzymatic reaction following this protocol :

- Mix the two junctions in equimolar concentration ([HJ1]=[HJ2]=10μM) in the ligation buffer T4 DNA Ligase Reaction Buffer and add 1μl of DNA T4 ligase for every 20μl of total reaction volume. Incubate at room temperature (25°C) for two hours.
- Heat inactivate at 65°C for 10 minutes.

Digestion of DNA constructs

The sequence of the Hyperdrive includes a restriction site for the enzyme BbsI. The digestion of the construct by the enzyme, cutting it in two can be done with the following protocol :

Reagents	Volumes
BbsI 10 Units/μl	1μl
Hyperdrive construct 0.25μg/μl	4 μl
NEB 2.1 10X	5 μl
H_2O	40 μl

- Place the above solution at 37°C for 1 hour for the ligation.
- Heat inactivate at 65°C for 20 minutes.

The final solution is directly run in a gel, see Fig. 5.8.

C.2.2 Gels Preparation

Once prepared, gels are run with one or two wells containing the DNA ladder shown in Fig. C.1. This allows estimate the size of dsDNA that are run. In the case of complex 3D structure such as Holliday junctions or the Hyperdrive construct, these bands cannot give quantitative informations but serve as a guide for the eye.

Agarose Gel

The agarose gels used in this work are all prepared at 0.8% (0.8g of agarose per 100mL of solvent).

They are prepared in the same solvent used for the gel electrophoresis, in this case TAE buffer 1X. 100 ml is a sufficient volume to mold a big enough gel, the recipe for an agarose gel at 0.8% is :

100 ml TAE buffer 1X mixed with 0.8g of agarose. The mixture is heated in the microwave oven until all the agarose is dissolved and let to cool down before casting in a holder. A calibrated comb is used to prepare 5μl wells into the gel. The migration of the gels is done at 130V for 2h.

Polyacrylamide Gel

Polyacrylamide gels are casted and run with a Mini-PROTEAN® Tetra Handcast Systems. The migration of the gels is done at 200V for 50 minutes The gels are prepared at 6% acrylamide content, this is the optimal concentration for the typical length of the oligonucleotides or 3D DNA constructs that are run. The components need to prepare a 10 ml gel are listed in the table below.

Reagents	Volumes
Acrylamide 40% 29:1	1.5 ml
TBE 10X	1.0 ml
TEMED	10 μl
APS 25%	10 μl
H_2O	7.5 ml
Total	10 ml

Both TEMED and APS 25% are put last as they are the catalysts agents for the gel polymerization. The mixing is done under the hood, the gel is inert once the polymerization process is done.

C.2.3 Surface Preparation

Cleaning Protocol

The initial cleaning protocol is the same for both the glass slide prior to gold deposition and the gold surface :

- Pass them shortly on the flame of a Bunsen burner.
- Place them in ethanol for 10 min in an ultrasonic bath at 30°C.
- Rinse the slides with ethanol and dry them with nitrogen.
- Place them in isopropanol for 10 min in an ultrasonic bath at 30°C.

- Rinse the slides with ethanol and dry them with nitrogen.
- Place them in MilliQ water for 10 min in an ultrasonic bath at 30°C.
- Rinse the slides with ethanol and dry them with nitrogen.

Additionally, following the procedure of [131], the gold slide are placed under UV/ozone for 10 min before a final rinse with MilliQ water prior to modification of the gold surface.

Protocol for Monolayer Desposition on Gold

In order to create a well-defined monolayer on the gold surface, DNA is first attached and then followed by mercapto-hexanol to fill in the gaps. The carbon tail of mercapto-hexanol has the same length as the thiol modification on the DNA strands. Thus, the base of the ssDNA are directly above the surface, hovering above a "carpet" made out of mercapto-hexanol. No bare gold is left after the process.

The procedure is as follows :

- Under an inert atmosphere (without oxygen), put the surface in contact with the DNA in the immobilization buffer ([Tris-HCl]=10mM, [EDTA]=1mM [NaCl]=500mM, [TCEP]=1mM -freshly prepared-, pH=7.3) for 60 minutes.
- Rinse the surface with working buffer ([TrisHCl]=10mM, [NaCl]=50mM, pH=7.3).
- Still under an inert atmosphere, put the surface in contact with mercapto-hexanol in working buffer ([MCH]=1mM, [TrisHCl]=10mM, [NaCl]=50mM, pH=7.3).
- Rinse the surface with working buffer.
- Put the surface in contact with a solution containing the complementary DNA strand in hybridization buffer ([TrisHCl]=10mM, [EDTA]=1mM, [NaCl]=500mM, pH=7.3) for 60 minutes.
- Rinse the surface with working buffer and keep it submerged with it.

The TCEP is used to break disulfide bonds and make sure that the sulfur atoms of the thiol groups are available to make a bond with the gold surface. It is especially important to use it when attaching the Hyperdrive construct on the surface since it has to modified strands with thiol groups in close proximity. The construct is prepared in advance and stored in the fridge so it is likely that some of it will see its two ends form a disulfide bond. This protocol is adapted from Rant's group papers as well as additional bibliography [132, 133, 134, 135, 136].

Bibliography

[1] A. Fall, B. Weber, M. Pakpour, N. Lenoir, N. Shahidzadeh, J. Fiscina, C. Wagner, and D. Bonn, "Sliding friction on wet and dry sand," *Physical Review Letters*, vol. 112, no. 17, pp. 3–6, 2014.

[2] M. Burrows and G. Sutton, "Interacting gears synchronize propulsive leg movements in a jumping insect," *Science*, vol. 341, no. 6151, pp. 1254–1256, 2013.

[3] M. Piccolino, "Biological machines: from mills to molecules," *Nature Reviews Molecular Cell Biology*, vol. 1, no. 2, pp. 149–152, 2000.

[4] M. Schliwa and G. Woehlke, "Molecular motors," 2003.

[5] B. Alberts, "The cell as a collection of protein machines: Preparing the next generation of molecular biologists," *Cell*, vol. 92, no. 3, pp. 291–294, 1998.

[6] A. Baumann, A. Sánchez-Ferrer, L. Jacomine, P. Martinoty, V. Le Houerou, F. Ziebert, and I. M. Kulić, "Motorizing fibres with geometric zero-energy modes," *Nature Materials*, vol. 17, no. 6, pp. 523–527, 2018.

[7] P.-G. de Gennes, "Reflexions sur un type de polymères nematiques," *Comptes Rendus de l'Académie des Sciences de Paris B*, vol. 281, pp. 101–103, 1975.

[8] J. Küpfer and H. Finkelmann, "Nematic liquid single crystal elastomers," *Makromol. Chem., Rapid Commun.*, vol. 12, pp. 717–726, 1991.

[9] T. Tanaka, I. Nishio, S. T. Sun, and S. Ueno-Nishio, "Collapse of gels in an electric field," *Science*, vol. 218, no. 4571, pp. 467–469, 1982.

[10] Y. Klein, E. Efrati, and E. Sharon, "Shaping of elastic sheets by prescription of non-Euclidean metrics," *Science*, vol. 315, no. 5815, pp. 1116–1120, 2007.

[11] J. Kim, J. A. Hanna, M. Byun, C. D. Santangelo, and R. C. Hayward, "Designing responsive buckled surfaces by halftone gel lithography," *Science*, vol. 335, no. 6073, pp. 1201–1205, 2012.

[12] M. Pezzulla, S. a. Shillig, P. Nardinocchi, and D. P. Holmes, "Morphing of geometric composites via residual swelling," *Soft Matter*, vol. 11, no. 29, pp. 5812–5820, 2015.

[13] R. Pelrine, R. Kornbluh, Q. Pei, and J. Joseph, "High-speed electrically actuated elastomers with strain greater than 100%," *Science*, vol. 287, no. 5454, pp. 836–839, 2000.

[14] C. S. Haines, M. D. Lima, N. Li, G. M. Spinks, J. Foroughi, J. D. Madden, S. H. Kim, S. Fang, M. J. De Andrade, F. Göktepe, O. Göktepe, S. M. Mirvakili, S. Naficy, X. Lepró, J. Oh, M. E. Kozlov, S. J. Kim, X. Xu, B. J. Swedlove, G. G. Wallace, and R. H. Baughman, "Artificial muscles from fishing line and sewing thread," *Science*, vol. 343, no. 6173, pp. 868–872, 2014.

[15] T. Mirfakhrai, J. D. W. Madden, and R. H. Baughman, "Polymer artificial muscles," *Materials Today*, vol. 10, no. 4, pp. 30–38, 2007.

[16] R. Dreyfus, J. Baudry, M. L. Roper, M. Fermigier, H. a. Stone, and J. Bibette, "Microscopic artificial swimmers," *Nature*, vol. 437, no. 7060, pp. 862–865, 2005.

[17] M. Camacho-Lopez, H. Finkelmann, P. Palffy-Muhoray, and M. Shelley, "Fast liquid-crystal elastomer swims into the dark," *Nature Materials*, vol. 3, no. 5, pp. 307–310, 2004.

[18] A. Mourran, H. Zhang, R. Vinokur, and M. Möller, "Soft Microrobots Employing Nonequilibrium Actuation via Plasmonic Heating," *Advanced Materials*, vol. 29, no. 2, 2017.

[19] S. Palagi, A. G. Mark, S. Y. Reigh, K. Melde, T. Qiu, H. Zeng, C. Parmeggiani, D. Martella, A. Sanchez-Castillo, N. Kapernaum, F. Giesselmann, D. S. Wiersma, E. Lauga, and P. Fischer, "Structured light enables biomimetic swimming and versatile locomotion of photoresponsive soft microrobots," *Nature Materials*, vol. 15, no. 6, pp. 647–653, 2016.

[20] P. Satir, "STUDIES ON CILIA," *The Journal of Cell Biology*, vol. 39, no. 1, pp. 77–94, 1968.

[21] M. Abercrombie, "The Croonian Lecture, 1978: The Crawling Movement of Metazoan Cells," *Proceedings of the Royal Society B: Biological Sciences*, vol. 207, no. 1167, pp. 129–147, 1980.

[22] B. Alberts, A. Johnson, J. Lewis, D. Morgan, M. Raff, K. Roberts, and P. Walter, *Molecular Biology of the Cell, 6th edition*. Garland New York, 2014.

[23] J. R. Howse, R. a.L. Jones, A. J. Ryan, T. Gough, R. Vafabakhsh, and R. Golestanian, "Self-Motile Colloidal Particles: From Directed Propulsion to Random Walk," *Physical Review Letters*, vol. 99, no. 4, pp. 8–11, 2007.

[24] A. Bricard, J. B. Caussin, N. Desreumaux, O. Dauchot, and D. Bartolo, "Emergence of macroscopic directed motion in populations of motile colloids," *Nature*, vol. 503, no. 7474, pp. 95–98, 2013.

[25] M. Yamada, M. Kondo, J. I. Mamiya, Y. Yu, M. Kinoshita, C. J. Barrett, and T. Ikeda, "Photomobile polymer materials: Towards light-driven plastic motors," *Angewandte Chemie - International Edition*, vol. 47, no. 27, pp. 4986–4988, 2008.

[26] T. Ikegami, Y. Kageyama, K. Obara, and S. Takeda, "Dissipative and Autonomous Square-Wave Self-Oscillation of a Macroscopic Hybrid Self-Assembly under Continuous Light Irradiation," *Angewandte Chemie - International Edition*, vol. 55, no. 29, pp. 8239–8243, 2016.

[27] T. J. White, N. V. Tabiryan, S. V. Serak, U. a. Hrozhyk, V. P. Tondiglia, H. Koerner, R. a. Vaia, and T. J. Bunning, "A high frequency photodriven polymer oscillator," *Soft Matter*, vol. 4, no. 9, pp. 1796–1798, 2008.

[28] X. Zhang, Z. Yu, C. Wang, D. Zarrouk, J. W. T. Seo, J. C. Cheng, A. D. Buchan, K. Takei, Y. Zhao, J. W. Ager, J. Zhang, M. Hettick, M. C. Hersam, A. P. Pisano, R. S. Fearing, and A. Javey, "Photoactuators and motors based on carbon nanotubes with selective chirality distributions," *Nature Communications*, vol. 5, pp. 1–8, 2014.

[29] L. Ionov, "Hydrogel-based actuators: Possibilities and limitations," *Materials Today*, vol. 17, no. 10, pp. 494–503, 2014.

[30] P. C. Martin, O. Parodi, and P. S. Pershan, "Unified hydrodynamic theory for crystals, liquid crystals, and normal fluids," *Physical Review A*, vol. 6, no. 6, pp. 2401–2420, 1972.

[31] M. Ma, L. Guo, D. G. Anderson, and R. Langer, "Bio-inspired polymer composite actuator and generator driven by water gradients," *Science*, vol. 339, no. 6116, pp. 186–189, 2013.

[32] J. Goldstone, A. Salam, S. Weinberg, and B. Symmetries, "Broken Symmetries," *Physical Review*, vol. 127, no. 3, pp. 965–970, 1962.

[33] D. Forster, *Hydrodynamic Fluctuations, Broken Symmetry, and Correlation Functions, Advanced Book Classics*. Addison Wesley, 1990.

[34] P. Chaikin and T. Lubensky, *Principles of Condensed Matter Physics*. Cambridge University Press, Cambridge, 1995.

[35] I. M. Kulić, R. Thaokar, and H. Schiessel, "Twirling DNA rings - Swimming nanomotors ready for a kickstart," *Europhysics Letters*, vol. 72, no. 4, pp. 527–533, 2005.

[36] K. Bhattacharya and R. D. James, "The material is the machine," *Science*, vol. 307, no. 5706, pp. 53–54, 2005.

[37] B. Audoly and Y. Pomeau, *Elasticity and Geometry*. Oxford University Press, Oxford, 2010.

[38] M. M. Müller, M. B. Amar, and J. Guven, "Conical defects in growing sheets," *Physical Review Letters*, vol. 101, no. 15, pp. 1–4, 2008.

[39] E. L. Starostin and G. H. Van Der Heijden, "The shape of a Möbius strip," *Nature Materials*, vol. 6, no. 8, pp. 563–567, 2007.

[40] J. F. Marko, "The internal 'slithering' dynamics of supercoiled DNA," *Physica A: Statistical Mechanics and its Applications*, vol. 244, no. 1-4, pp. 263–277, 1997.

[41] H. C. Berg and R. A. Anderson, "Bacteria swim by rotating their flagellar filaments," *Nature*, vol. 245, no. 5425, pp. 380–382, 1973.

[42] F. A. Samatey, H. Matsunami, K. Imada, S. Nagashima, T. R. Shaikh, D. R. Thomas, J. Z. Chen, D. J. DeRosier, A. Kitao, and K. Namba, "Structure of the bacterial flagellar hook and implication for the molecular universal joint mechanism," 2004.

[43] H. Mohrbach, A. Johner, and I. M. Kulić, "Tubulin bistability and polymorphic dynamics of microtubules," *Physical Review Letters*, vol. 105, no. 26, pp. 1–4, 2010.

[44] S. Trachtenberg, "Shaping and moving a Spiroplasma," *Journal of Molecular Microbiology and Biotechnology*, vol. 7, no. 1-2, pp. 78–87, 2004.

[45] S. Trachtenberg, "The cytoskeleton of spiroplasma: A complex linear motor," *Journal of Molecular Microbiology and Biotechnology*, vol. 11, no. 3-5, pp. 265–283, 2006.

[46] J. Kürner, A. S. Frangakis, and W. Baumeister, "Cryo – Electron Tomography Reveals the Cytoskeletal Structure of Spiroplasma melliferum," *Science*, vol. 436, no. 2005, pp. 436–439, 2005.

[47] J. W. Shaevitz, J. Y. Lee, and D. a. Fletcher, "Spiroplasma swim by a processive change in body helicity," *Cell*, vol. 122, no. 6, pp. 941–945, 2005.

[48] H. Wada and R. R. Netz, "Model for self-propulsive helical filaments: Kink-pair propagation," *Physical Review Letters*, vol. 99, no. 10, pp. 5–8, 2007.

[49] S. Daniel, M. K. Chaudhury, and J. C. Chen, "Fast drop movements resulting from the phase change on a gradient surface," *Science*, vol. 291, no. 5504, pp. 633–636, 2001.

[50] H. Linke, B. J. Alemán, L. D. Melling, M. J. Taormina, M. J. Francis, C. C. Dow-Hygelund, V. Narayanan, R. P. Taylor, and a. Stout, "Self-propelled leidenfrost droplets," *Physical Review Letters*, vol. 96, no. 15, pp. 2–5, 2006.

[51] E. Bormashenko, Y. Bormashenko, R. Grynyov, H. Aharoni, G. Whyman, and B. P. Binks, "Self-propulsion of liquid marbles: Leidenfrost-like levitation driven by marangoni flow," *Journal of Physical Chemistry C*, vol. 119, no. 18, pp. 9910–9915, 2015.

[52] GingerCat, "Rolling sausage (official video)." `https://www.youtube.com/watch?v=3hNTAr56n3Q`, October 2014.

[53] E. Liscum, S. K. Askinosie, D. L. Leuchtman, J. Morrow, K. T. Willenburg, and D. R. Coats, "Phototropism: Growing towards an Understanding of Plant Movement," *The Plant Cell*, vol. 26, no. 1, pp. 38–55, 2014.

[54] C. Darwin and F. Darwin, *The Power of Movement in Plants*. (London: John Murray Publishers, 1880.

[55] H. Zeng, P. Wasylczyk, C. Parmeggiani, D. Martella, M. Burresi, and D. S. Wiersma, "Light-Fueled Microscopic Walkers," *Advanced Materials*, vol. 27, no. 26, pp. 3883–3887, 2015.

[56] S. U. Pickering, "CXCVI. -Emulsions.," *J. Chem. Soc. Trans.*, vol. 91, pp. 2001–2021, 1907.

[57] Y. Yang, Z. Fang, X. Chen, W. Zhang, Y. Xie, Y. Chen, Z. Liu, and W. Yuan, "An overview of pickering emulsions: Solid-particle materials, classification, morphology, and applications," *Frontiers in Pharmacology*, vol. 8, no. MAY, pp. 1–20, 2017.

[58] F. H. C. Crick and J. Watson, "Molecular Structure of Nucleic Acids : A Structure for Deoxyribose Nucleic Acid," *Nature,*, vol. 171, no. 4356, pp. 737–738, 1953.

[59] N. C. Seeman, "Nucleic acid junctions and lattices," *Journal of Theoretical Biology*, vol. 99, no. 2, pp. 237–247, 1982.

[60] J. Chen and N. C. Seeman, "Synthesis from DNA of a molecule with the connectivity of a cube," *Nature*, vol. 350, no. 6319, pp. 631–633, 1991.

[61] Y. Zhang and N. C. Seeman, "eAccess-Service der Universitaetsbibliothek der TUM," *Journal of the American Chemical Society*, no. 13, pp. 1661–1669, 1994.

[62] W. M. Shih, J. D. Quispe, and G. F. Joyce, "A 1.7-kilobase single-stranded DNA that folds into a nanoscale octahedron," *Nature*, vol. 427, no. 6975, pp. 618–621, 2004.

[63] A. Chworos, I. Severcan, A. Y. Koyfman, P. Weinkam, E. Oroudjev, H. G. Hansma, and L. Jaeger, "Building programmable jigsaw puzzles with RNA," *Science*, vol. 306, no. 5704, pp. 2068–2072, 2004.

[64] N. C. Seeman and P. S. Lukeman, "Nucleic acid nanostructures: Bottom-up control of geometry on the nanoscale," *Reports on Progress in Physics*, vol. 68, no. 1, pp. 237–270, 2005.

[65] N. C. Seeman, "Nanomaterials based on DNA.," *Annual review of biochemistry*, vol. 79, pp. 65–87, 2010.

[66] S. H. Park, C. Pistol, S. J. Ahn, J. H. Reif, A. R. Lebeck, C. Dwyer, and T. H. LaBean, "Finite-size, fully addressable DNA tile lattices formed by hierarchical assembly procedures," *Angewandte Chemie - International Edition*, vol. 45, no. 5, pp. 735–739, 2006.

[67] P. W. Rothemund, "Folding DNA to create nanoscale shapes and patterns," *Nature*, vol. 440, no. 7082, pp. 297–302, 2006.

[68] R. P. Feynman, "There's plenty of room at the bottom: An invitation to enter a new field of physics," in *Caltech's Eng Sci*, pp. 22–36, 1960.

[69] S. M. Douglas, H. Dietz, T. Liedl, B. Högberg, F. Graf, and W. M. Shih, "Self-assembly of DNA into nanoscale three-dimensional shapes," *Nature*, vol. 459, no. 7245, pp. 414–418, 2009.

[70] H. Dietz, S. M. Douglas, and W. M. Shih, "Folding DNA into twisted and curved nanoscale shapes," *Science*, vol. 325, no. 5941, pp. 725–730, 2009.

[71] T. Gerling, K. F. Wagenbauer, A. M. Neuner, and H. Dietz, "Dynamic DNA devices and assemblies formed by shape-complementary, non-base pairing 3D components," *Science*, vol. 347, no. 6229, pp. 1446–1452, 2015.

[72] A. N. Schechter, K. Singer, H. Lehmann, W. Castle, T. Huisman, and E. Jaffe, "ASH 50th anniversary review Hemoglobin research and the origins of molecular medicine," *Blood*, vol. 112, no. 10, pp. 3927–3938, 2008.

[73] K. Wang, J. M. Hamill, B. Wang, C. Guo, S. Jiang, Z. Huang, and B. Xu, "Structure determined charge transport in single DNA molecule break junctions," *Chemical Science*, vol. 5, no. 9, pp. 3425–3431, 2014.

[74] H. Mohrbach, A. Johner, and I. M. Kulić, "Cooperative lattice dynamics and anomalous fluctuations of microtubules," *European Biophysics Journal*, vol. 41, no. 2, pp. 217–239, 2012.

[75] O. Kahraman, H. Mohrbach, M. M. Müller, and I. M. Kulić, "Confotronic dynamics of tubular filaments," *Soft Matter*, pp. 2836–2847, 2014.

[76] F. Ziebert, H. Mohrbach, and I. M. Kulić, "Why Microtubules Run in Circles: Mechanical Hysteresis of the Tubulin Lattice," *Physical Review Letters*, vol. 114, no. 14, 2015.

[77] T. Sanchez, I. M. Kulic, and Z. Dogic, "Circularization, photomechanical switching, and a supercoiling transition of actin filaments," *Physical Review Letters*, vol. 104, no. 9, pp. 65–68, 2010.

[78] T. Odijk, "Stiff Chains and Filaments under Tension," *Macromolecules*, vol. 28, pp. 7016–7018, 1995.

[79] S. C. Mao, X. D. Han, Z. Zhang, and M. H. Wu, "The nano- and mesoscopic cooperative collective mechanisms of inhomogenous elastic-plastic transitions in polycrystalline TiNi shape memory alloys," *Journal of Applied Physics*, vol. 101, no. 10, 2007.

[80] J. Monod, J. Wyman, and J. P. Changeux, "on the Nature of Allosteric Transitions: a Plausible Model.," *Journal of molecular biology*, vol. 12, no. 1, pp. 88–118, 1965.

[81] W. Wang, L. M. Nocka, B. Z. Wiemann, D. M. Hinckley, I. Mukerji, and F. W. Starr, "Holliday Junction Thermodynamics and Structure: Coarse-Grained Simulations and Experiments," *Scientific Reports*, vol. 6, no. October 2015, pp. 1–13, 2016.

[82] Y. Liu and S. C. West, "Happy Hollidays: 40th anniversary of the Holliday junction.," *Nature reviews. Molecular cell biology*, vol. 5, no. 11, pp. 937–944, 2004.

[83] R. Holliday, "A mechanism for gene conversion in fungi," *Genetics Research*, vol. 5, no. 2, pp. 282–304, 1964.

[84] E. von Kitzing, D. M. Lilley, and S. Diekmann, "The stereochemistry of a four-way DNA junction: A theoretical study," *Nucleic Acids Research*, vol. 18, no. 9, pp. 2671–2683, 1990.

[85] D. R. Duckett, A. I. H. Murchie, and D. M. J. Lilley, "The role of metal ions in the conformation of the four-way DNA junction," *The EMBO Journal*, vol. 9, pp. 583–590, 1990.

[86] R. M. Clegg, a. I. Murchie, a. Zechel, C. Carlberg, S. Diekmann, and D. M. Lilley, "Fluorescence resonance energy transfer analysis of the structure of the four-way DNA junction.," *Biochemistry*, vol. 31, no. 20, pp. 4846–56, 1992.

[87] R. M. Clegg, a. I. Murchie, and D. M. Lilley, "The solution structure of the four-way DNA junction at low-salt conditions: a fluorescence resonance energy transfer analysis," *Biophysical Journal*, vol. 66, no. 1, pp. 99–109, 1994.

[88] C. Joo, S. a. McKinney, D. M. Lilley, and T. Ha, "Exploring rare conformational species and ionic effects in DNA Holliday junctions using single-molecule spectroscopy," *Journal of Molecular Biology*, vol. 341, no. 3, pp. 739–751, 2004.

[89] C. P. Mountford, a. R. Mount, S. a.G. Evans, T. J. Su, P. Dickinson, a. H. Buck, C. J. Campbell, J. G. Terry, J. S. Beattie, a. J. Walton, P. Ghazal, and J. Crain, "Time-resolved FRET and FLIM of four-way DNA junctions," *Journal of Fluorescence*, vol. 16, no. 6, pp. 839–845, 2006.

[90] D. M. J. Lilley, "Structures of helical junctions in nucleic acids," 2000.

[91] F. Weysser, O. Benzerara, A. Johner, and I. M. Kulić, "Topological energy storage of work generated by nanomotors," *Soft Matter*, vol. 11, no. 4, pp. 732–740, 2015.

[92] Q. Li, G. Fuks, E. Moulin, M. Maaloum, M. Rawiso, I. Kulic, J. T. Foy, and N. Giuseppone, "Macroscopic contraction of a gel induced by the integrated motion of light-driven molecular motors," *Nature Nanotechnology*, vol. 10, no. 2, pp. 161–165, 2015.

[93] N. Koumura, R. W. J. Zijistra, R. A. Van Delden, N. Harada, and B. L. Feringa, "Light-driven monodirectional molecular rotor," *Nature*, vol. 401, no. 6749, pp. 152–155, 1999.

[94] T. M. Herne and M. J. Tarlov, "Characterization of DNA Probes Immobilized on Gold Surfaces," *Journal of the American Chemical Society*, vol. 119, no. 38, pp. 8916–8920, 1997.

[95] R. Levicky, T. M. Herne, M. J. Tarlov, and S. K. Satija, "Using self-assembly to control the structure of DNA monolayers on gold: A neutron reflectivity study," *Journal of the American Chemical Society*, vol. 120, no. 38, pp. 9787–9792, 1998.

[96] A. B. Steel, T. M. Herne, and M. J. Tarlov, "Electrochemical quantitation of DNA immobilized on gold," *Analytical Chemistry*, vol. 70, no. 22, pp. 4670–4677, 1998.

[97] M. Yang, H. C. M. Yau, and H. L. Chan, "Adsorption Kinetics and Ligand-Binding Properties of Thiol-Modified Double-Stranded DNA on a Gold Surface," *Langmuir*, vol. 14, no. 21, pp. 6121–6129, 1998.

[98] H. Wackerbarth, M. Grubb, J. Zhang, A. G. Hansen, and J. Ulstrup, "Long-range order of organized oligonucleotide monolayers on Au(111) electrodes," *Langmuir*, vol. 20, no. 5, pp. 1647–1655, 2004.

[99] R. Lao, S. Song, H. Wu, L. Wang, Z. Zhang, L. He, and C. Fan, "Electrochemical interrogation of DNA monolayers on gold surfaces," *Analytical Chemistry*, vol. 77, no. 19, pp. 6475–6480, 2005.

[100] R. N. Love, J.C., L.A. Estroff, J.K. Kriebel and G. Whitesides, *Self-Assembled Monolayers of Thiolates on Metals as a Form of Nanotechnology*, vol. 105. 2005.

[101] Y. Xiao, R. Y. Lai, and K. W. Plaxco, "Preparation of electrode-immobilized, redox-modified oligonucleotides for electrochemical DNA and aptamer-based sensing.," *Nature protocols*, vol. 2, no. 11, pp. 2875–2880, 2007.

[102] U. Rant, K. Arinaga, T. Fujiwara, S. Fujita, M. Tornow, N. Yokoyama, and G. Abstreiter, "Excessive Counterion Condensation on Immobilized ssDNA in Solutions of High Ionic Strength," *Biophysical Journal*, vol. 85, no. 6, pp. 3858–3864, 2003.

[103] U. Rant, K. Arinaga, S. Fujita, N. Yokoyama, G. Abstreiter, and M. Tornow, "Dynamic electrical switching of DNA layers on a metal surface," *Nano Letters*, vol. 4, no. 12, pp. 2441–2445, 2004.

[104] U. Rant, K. Arinaga, M. Tornow, W. K. Yong, R. R. Netz, S. Fujita, N. Yokoyama, and G. Abstreiter, "Dissimilar kinetic behavior of electrically manipulated single- and double-stranded DNA tethered to a gold surface," *Biophysical Journal*, vol. 90, no. 10, pp. 3666–3671, 2006.

[105] U. Rant, K. Arinaga, S. Fujita, N. Yokoyama, G. Abstreiter, and M. Tornow, "Electrical manipulation of oligonucleotides grafted to charged surfaces," *Organic and Biomolecular Chemistry*, vol. 4, no. 18, pp. 3448–3455, 2006.

[106] U. Rant, K. Arinaga, S. Scherer, E. Pringsheim, S. Fujita, N. Yokoyama, M. Tornow, and G. Abstreiter, "Switchable DNA interfaces for the highly sensitive detection of label-free DNA targets.," *Proc. Nat. Acad. Sci. USA*, vol. 104, no. 44, pp. 17364–9, 2007.

[107] W. Kaiser and U. Rant, "Conformations of End-Tethered DNA Molecules on Gold Screening , and Temperature," *Journal of the American Chemical Society*, vol. 132, no. 15, pp. 7935–7945, 2010.

[108] A. Langer, P. a. Hampel, W. Kaiser, J. Knezevic, T. Welte, V. Villa, M. Maruyama, M. Svejda, S. Jähner, F. Fischer, R. Strasser, and U. Rant, "Protein analysis by time-resolved measurements with an electro-switchable DNA chip," *Nature Communications*, vol. 4, 2013.

[109] a. Langer, W. Kaiser, M. Svejda, P. Schwertler, and U. Rant, "Molecular dynamics of DNA-protein conjugates on electrified surfaces: Solutions to the drift-diffusion equation," *Journal of Physical Chemistry B*, vol. 118, no. 2, pp. 597–607, 2014.

[110] A. Langer, M. Schräml, R. Strasser, H. Daub, T. Myers, D. Heindl, and U. Rant, "Polymerase/DNA interactions and enzymatic activity: Multi-parameter analysis with electro-switchable biosurfaces," *Scientific Reports*, vol. 5, no. January, pp. 1–15, 2015.

[111] E. Kopperger, J. List, S. Madhira, F. Rothfischer, D. C. Lamb, and F. C. Simmel, "A self-assembled nanoscale robotic arm controlled by electric fields," *Science*, vol. 359, no. 6373, pp. 296–301, 2018.

[112] A. Huhle, D. Klaue, H. Brutzer, P. Daldrop, S. Joo, O. Otto, U. F. Keyser, and R. Seidel, "Camera-based three-dimensional real-time particle tracking at kHz rates and Ångström accuracy," *Nature Communications*, vol. 6, 2015.

[113] P. Liu, Y. Zhou, M. Guo, S. Yang, O. Félix, D. Martel, Y. Qiu, Y. Ma, and G. Decher, "Fluorescence-enhanced bio-detection platforms obtained through controlled "step-by-step" clustering of silver nanoparticles," *Nanoscale*, vol. 10, no. 2, pp. 848–855, 2018.

[114] G. Schneider and G. Decher, "From functional core/shell nanoparticles prepared via layer-by-layer deposition to empty nanospheres," *Nano Letters*, vol. 4, no. 10, pp. 1833–1839, 2004.

[115] R. R. Chance, A. Prock, and R. Silbey, "Molecular Fluorescence and Energy Transfer Near Interfaces," in *Advances in Chemical Physics*, pp. 1–65, 1978.

[116] B. N. Persson, "Theory of the damping of excited molecules located above a metal surface," *Journal of Physics C: Solid State Physics*, vol. 11, no. 20, pp. 4251–4269, 1978.

[117] G. Schneider, G. Decher, N. Nerambourg, R. Praho, M. H. V. Werts, and M. Blanchard-Desce, "Distance-dependent fluorescence quenching on gold nanoparticles ensheathed with layer-by-layer assembled polyelectrolytes," *Nano Letters*, vol. 6, no. 3, pp. 530–536, 2006.

[118] B. J. Roxworthy, A. M. Bhuiya, S. P. Vanka, and K. C. Toussaint, "Understanding and controlling plasmon-induced convection," *Nature Communications*, vol. 5, pp. 1–8, 2014.

[119] J. S. Donner, G. Baffou, D. McCloskey, and R. Quidant, "Plasmon-assisted optofluidics," *ACS Nano*, vol. 5, no. 7, pp. 5457–5462, 2011.

[120] M. Wang, C. Zhao, X. Miao, Y. Zhao, J. Rufo, Y. J. Liu, T. J. Huang, and Y. Zheng, "Plasmofluidics: Merging Light and Fluids at the Micro-/Nanoscale," *Small*, vol. 11, no. 35, pp. 4423–4444, 2015.

[121] L. Rayleigh, "LIX. ¡i¿On convection currents in a horizontal layer of fluid, when the higher temperature is on the under side¡/i¿," *Philosophical Magazine Series 6*, vol. 32, no. 192, pp. 529–546, 1916.

[122] H. Bénard, "Les tourbillons cellulaires dans une nappe liquide," *Revue Générale des Sciences Pures et Appliquées*, vol. 11, pp. 1261–1271 and 1300–1328, 1900.

[123] P. Bergé and M. Dubois, "Rayleigh-bénard convection," *Contemporary Physics*, vol. 25, no. 6, pp. 535–582, 1984.

[124] C. Millot, L. A. Fillot, O. Lame, P. Sotta, and R. Seguela, "Assessment of polyamide-6 crystallinity by DSC: Temperature dependence of the melting enthalpy," *Journal of Thermal Analysis and Calorimetry*, vol. 122, no. 1, pp. 307–314, 2015.

[125] Y. Katoh and M. Okamoto, "Crystallization controlled by layered silicates in nylon 6-clay nano-composite," *Polymer*, vol. 50, no. 19, pp. 4718–4726, 2009.

[126] K. Miyasaka and K. Makishima, "Transition of nylon 6 γ phase crystals by stretching in the chain direction," *Journal of Polymer Science Part A: Polymer Chemistry*, vol. 5, pp. 3017–3027, 1967.

[127] T. Itoh, "Change with temperature in crystal structures of nylons 6, 66 and 610," *Japanese Journal of Applied Physics*, vol. 15, no. 12, pp. 2295–2306, 1976.

[128] G. Gururajan, S. P. Sullivan, T. P. Beebe, D. B. Chase, and J. F. Rabolt, "Continuous electrospinning of polymer nanofibers of Nylon-6 using an atomic force microscope tip," *Nanoscale*, vol. 3, no. 8, pp. 3300–3308, 2011.

[129] J. H. Lienhard(IV) and J. H. Lienhard(V), *A Heat Transfer Textbook*. Phlogiston Press, Cambridge Massachusetts, 2008.

[130] M. Born and E. Wolf, *Principles of Optics 7th edition*. Cambridge University Press, Cambridge, 1999.

[131] C. G. Worley and R. W. Linton, "Removing sulfur from gold using ultraviolet/ozone cleaning," *Journal of Vacuum Science & Technology A: Vacuum, Surfaces, and Films*, vol. 13, no. 4, pp. 2281–2284, 1995.

[132] J. Liu and Y. Lu, "Preparation of aptamer-linked gold nanoparticle purple aggregates for colorimetric sensing of analytes," *Nature Protocols*, vol. 1, no. 1, pp. 246–252, 2006.

[133] J. Zhang, S. Song, L. Zhang, L. Wang, H. Wu, D. Pan, and C. Fan, "Sequence-specific detection of femtomolar DNA via a chronocoulometric DNA sensor (CDS): Effects of nanoparticle-mediated amplification and nanoscale control of DNA assembly at electrodes," *Journal of the American Chemical Society*, vol. 128, no. 26, pp. 8575–8580, 2006.

[134] J. Zhang, S. Song, L. Wang, D. Pan, and C. Fan, "A gold nanoparticle-based chronocoulometric dna sensor for amplified detection of dna," *Nature Protocols*, vol. 2, no. 11, pp. 2888–2895, 2007.

[135] K. Hu, D. Lan, X. Li, and S. Zhang, "Electrochemical DNA biosensor based on nanoporous gold electrode and multifunctional encoded DNA-Au bio bar codes," *Analytical Chemistry*, vol. 80, no. 23, pp. 9124–9130, 2008.

[136] D. B. Peckys, N. De Jonge, M. L. Simpson, and T. E. McKnight, "End-specific strategies of attachment of long double stranded DNA onto gold-coated nanofiber arrays," *Nanotechnology*, vol. 19, no. 43, 2008.

List of Figures

1 A : Cas de la fibre linéaire bidirectionnelle. B : Cas du tore. De par sa géométrie, il est compréssé à l'intérieur et étiré à l'extérieur, la chaleur provoque plus de compression vers le bas donc la fibre tourne sur elle-même pour minimiser sa frustration. 6

2 A : ADN marqué par fluorescence attaché sur une surface d'or par des liaisons thiols : la fluorescence est inhibée pour les brins d'ADN trop proches de la surface. L'illumination chauffe l'or et créé un courant de convection dans la chambre d'observation. Le flux soulève les brins et permet l'observation d'un signal de fluorescence. B : Trois étapes de la vague à différents temps après le début de l'illumination, les flèches indiquent la direction de propagation de la vague. Echelle : 100 μm, Carte de couleur : Niveaux de gris 8-bit. 8

1.1 Table of simple mechanisms, from *Chambers' Cyclopaedia*, 1728. 16

2.1 **"The embedded wheel" paradigm : Global zero elastic energy modes (ZEEMs) in prestrained elastic objects.** a) Closing an elastic fiber into a ring induces compressive strain in the inner portion (solid line) and tensile strain on the outside (dashed line). b) The torus now has a deformation mode that leaves its elastic energy unchanged : the collective rotation of the fiber's cross-sections around their axis. c) A wide array of elastic objects such as a Möbius strip or an edge-crumpled disk possess global ZEEMs. 21

2.2 A sausage rolling on the inside of a pan upon cooking, the four consequent images span approximately one second, see [52]. 23

2.3 Blue light induced phototropism in higher plants requires the establishment of a differential gradient of auxin (from [53]. A)Diagram of a hypocotyl exhibiting a phototropic response. Auxin synthesized in the apical portions of the stem is polarly transported toward the root predominately through the central vasculature and to a lesser extent via epidermal and subepidermal cell layers (downward pointing red arrows). B) Cross section within the elongation zone of an Arabidopsis seedling hypocotyl illustrating the gradients of phot1 (blue light sensitive receptor) activity (false-colored white to blue) and auxin accumulation (false-colored white to yellow). 24

2.4 Experimental realizations of the fiberdrive with a) PDMS (radius 2cm, thickness 0.6mm) and b) Nylon (radius 6cm, thickness 0.6mm). The direction of rotation depends on the sign of the thermal expansion coefficient, positive for PDMS and negative for Nylon. 25
2.5 Rolling motion of a nylon-6 rod (diameter 0.6 mm, length 12 cm) (A) and a PDMS rod (diameter 3 mm, length 11 cm) (B). 25
2.6 a) From its topology, the torus has a strain gradient imposed by the bending. b) When put in contact with a hot plate, the temperature gradient between the surface and the ambiant air induces a thermal prestrain in the z-direction perpendicular to the plane. c) The conflict between the geometrically imposed prestrain and the thermally driven prestrain gives rise to a dynamic instability : the torus begins to turn with a constant speed ω. . . 28
2.7 The geometry of the toroidal fiberdrive. The internal temperature profile T_{int} of each cross-section is decomposed in two modes. The thermal z-mode is pumped by the heat flux p normal to the substrate (represented by the red horizontal line). The x-mode ΔT_x emerges from the z-mode ΔT_z by frame rotation with the angle Φ. 29
2.8 The temperature gradient between the hot plate and the ambient air bends the rod via thermal expansion or contraction. Due to the confinement (on the plate) the curving stays in-plane, which effectively creates a torque. The direction of the curvature $\boldsymbol{\kappa}$ relative to the velocity $\mathbf{V}$ depends on the sign of the thermal expansion coefficient. 31
2.9 Continuous onset of rotation of a fiver closed to a ring as given by (2.22). Shown is the scaled angular velocity, $\bar{\omega}$, as a function of the rescaled effective driving $\frac{\bar{p}}{z_s}$. 34
2.10 By constraining the fiber in place with a holder, a spiral can be created. It can be thermally driven to produce rotation using the same principle as for the fiberdrive. 35
2.11 Discontinuous onset of rolling motion for a straight fiber given by solving (2.28). Shown is the scaled angular velocity, $\bar{\omega}$, as a function of the rescaled effective driving, $\sqrt{\frac{b}{c}}\bar{p}$. The black branch is stable, the red one unstable. . . 36
2.12 The fiberboid effect is shown to work on several types of polymers. A) Dried starch rods (spaghetti) propelled on a heating plate. The lower panel shows a kymograph (space-time plot) of the motion orthogonal to the fiber axis. B) Silicone rubber rod, superposition of images. The rolling trajectory is slightly curved due to the slight conical shape of the sample. C) Collective motion of several nylon-6 rods confined between two spacers. The lower panel again shows the kymograph. 39
2.13 Macaroni noodles rolling on the surface of a wet sponge-like material. Pasta is a versatile tool to demonstrate the fiberboid effect. Here it is driven by an evaporation flux. The time scales are four orders of magnitude slower than for the thermal fiberboid but it is nonetheless the same physics that powers the motion. 40

3.1 The main samples studied are fishing lines made of Nylon with diameters ranging from 0.12mm to 0.8mm. 42

3.2 Collective spontaneous self-healing of defects in a circular fiber motor from nylon-6 rotating at 190°C. A strong deformation defect (kink) emerges at time t = 7 s and persists for several seconds. The continued collective rotation of the fiber leads to a complete self-healing at a later time (t = 30 s) 43

3.3 The angular frequency of various-sized nylon rings (fiber thickness 0.6 mm) as a function of plate temperature. The error bars are equal to the standard deviation of ten measurements on a ring and the lines are only guides for the eye. 44

3.4 Spiral fiberdrive (fiber thickness 0.8mm, total spiral length 3.2m) realized according to the design showed in Fig. 2.10. It is rotating at 185°C lifting a payload (Eiffel Tower replica of weight 20 g). The fiber is guided from the spiral holder through two brass tubes and rotates freely there. Inset: position of the weight as it is lifted. 45

3.5 Continuous operation long time-testing of a spiral fiber motor. The fiber (nylon-6) is guided to a 13 turn, 0.6 mm diameter spiral and runs at T=160°C. The magenta line is a fit to $f(t) = f_0 exp(\frac{-t}{t_r})$, with $f_0 = 0.63$Hz and with the exponential frequency relaxation time of $t_r = 34h$ ($1.28\text{x}10^5 s$). The error bars are the standard deviations from 10 separate measurements. 46

3.6 When clamping the spiral at one end, it continues to operate, storing elastic energy. The longer tests were performed until a buckling event as depicted on the right happened, the tests were stopped to prevent mechanical damage to the spirals. 46

3.7 Charging of the 'spiral fiber battery'. Inset: number of turns as a function of time for spirals of various lengths that are rigidly blocked at one end. The lines are fits to the theory (subsection 2.2.4 and equation 2.36), which allows an estimate of the stored elastic-energy density, shown in the main panel as a function of spiral length. The red line is the predicted scaling with L^2. . 47

3.8 The stalling torque of the spirals studied in Fig. 3.7 as a function of spiral length, which displays a linear scaling (red line) 48

3.9 Rolling velocity (same fiber as in Fig. 3.13). During the first temperature cycle (red line), the fiber undergoes an annealing process and becomes conditioned ('trained'). In the subsequent cycles of decreasing/increasing temperature, the fiber attains a reproducible velocity (blue/green curves). The error bar are calculated from the standard deviation of three different specimen. 49

3.10 Slow annealing of a 800 μm nylon fiber at 110°C results in some transient reshaping and eventually within the time course of 10-20 seconds leads to an ideally straight and rolling fiber. 50

3.11 Exposing a nylon fiber (800 μm) directly to an elevated temperature (180°C) results in rapid uncontrolled reshaping. The final shape remains stationary and does not move or roll over the surface. 51

3.12 Measurement of linear and angular velocity. a) A nylon-6 fiber of radius 60 μm rolling at 185°C. b) Kymograph of the motion along the red line in a). In addition to a constant velocity linear motion, the fiber displays a velocity modulation (yellow arrows) in phase with its rotary motion. On the right, the effective radius of the fiber is shown, deduced from the ratio of linear and angular velocity. 52
3.13 Thermally induced curvature as a function of temperature for a nylon-6 fiber of radius 0.3 mm. The errors bars are calculated from the standard deviation of three different specimen. 53
3.14 Rolling velocity as a function of the plate temperature for annealed PVDF fibers of diameter 0.5 mm. The errors bars are calculated from the standard deviations of ten measurements. 54
3.15 Single fibers are bidirectional motor units able to perform work, in the experiment shown here it is against their own weight on an inclined plane. Shown is the angular turning frequency of a nylon-6 fiber (0.2 mm radius) as a function of the axial torque per length at two different temperatures (red, 180°C; blue, 140°C). Solid lines are fits to the theoretically predicted torque-velocity relation of Eq. (B.60). 55
3.16 fibers with decreasing radii rotate with increasing angular frequencies: experimental data for two temperatures and a power-law fit $R^{-\gamma}$ with $\gamma = 0.75$. The errors bar are calculated from the standard deviation of three different specimen. 55

4.1 Natural confotronic systems in nature. A) At high salt, collective flipping and rotations of DNA basepairs induces a collective switch from the right-handed conformation of B-DNA to the left-handed conformation of the Z-DNA, from [73]. B) The bacteria spiroplasma undergo active conformational transitions of their cytoskeletal sheet (found on the inside of their membranes). By undergoing a yet unspecified lattice switch that induces a right-left-helical kink and actively propagates along their body they manage to rapidly swim, from [47]. C) The transition from the oxy-conformation (left) to the deoxy-conformation (right) in hemoglobin is correlated with the oxygen concentration in the blood, from [72]. 59
4.2 Propagation of a mechanical perturbation along the backbone of a model polymer - the scissor-foldamer. The connectivity between individual "scissor"-units allows for some cooperativity between neigbours. 61
4.3 **Idealized schematic of the junction conformations.** The stacked (a) iso-I and (b) iso-II conformations predominate at moderate and high salt concentrations. (c) The open conformation is mainly observed at low salt concentration, and also potentially acts as an intermediary of conformational changes between iso-I and II, from [81]. 61
4.4 Coarsed-grained representation of confotronic dimer. It consists of two switchable Holliday Junction-units linked together. 62
4.5 A Holliday junction with a palindromic sequence can undergo a branch migration in a diffusive manner. The process is accompanied with rotation of the four branches at a rate of 1 turn for every 10.5 basepairs migrated. . . 63

4.6 Applications of the tanglotron. (a) A ”topo gel” consisting of reticulated tanglotrons acts as an artificial muscle. (b) The time-scale-bridging function of a tanglotron. It can easily move objects billion times heavier than itself via the trick of transient energy buffering in the chains. (c) The rotary motion can be transformed into linear actuation via a DNA cruciform structure (at positions 1 and 1’). The tanglotron device can now bridge to any DNA nano-assembly if we cut/open the end loops of the cruciform at connections 2 and 2’. The cruciform transmits both rotary to rotary motion and rotary to linear motion. (d) The motor unit can be directly coupled to distant catalytic centers that act as energy consumers, here an ATP-synthase. The (transmembrane) proton motive subunit of the ATP-synthase is replaced by the distant rotary motor, softly coupled by polymer chains. In reverse, supplying the synthase with excess ATP turns it itself a rotary motor unit, from [91]. 64
4.7 Electrically induced, persistent switching of a DNA layer on a Au surface. Left: The fluorescence intensity observed from the dye-labeled DNA layer alternates upon periodically reversing the electrode charge. Right: Negatively biased electrodes repel the likewise charged DNA strands, bright fluorescence is emitted from the dye attached to the DNA’s top end. Positive surface charge attracts the strands and due to the close proximity to the metal efficient energy transfer from the excited dye to the Au results in a substantial quenching of fluorescence, from [103] 65
4.8 The design of the HyperDrive. The motor is grafted onto a gold electrode via thiol groups at the end of the two strands, the rest of the surface is covered by mercaptohexanol molecules. The part that can be actuated via an alternative potential is pictured in blue, it can migrate between two extreme positions thanks to it palindromic sequence. The ”feet” are complementary to the ”shoes” grafted on the micrometric bead and allow for the coupling between the motor and the bead, they can transmit the rotation caused by the migration of the junction to the bead. 66
4.9 One powercycle of the HyperDrive. Starting on the top left with a negative potential, the construct is fully extended and bound to the bead. Upon switching to a positive potential, the junction starts to migrate, causing the rotation of the bead bound to the end strands. The rate of the branch migration added to the torque exerted by the Hyperdrive rips off the feet from the bead. Once it has reached the end of its course, the construct is flat on the surface and unbound from the bead. Switching back to a negative potential, the junction starts to migrate the other way around but the end strands undergo a void rotation since they are not bound to the bead. At the end of this step the junction is back to a fully extended state and bound to the bead, reaching the end of one cycle. 67

5.1 Oligonucleotides used to from the two distinct Holliday junctions used as monomers for the confotronic fiber. 70
5.2 Schematic of the confotronic dimer showing the complementary sequences as well as the two points where the junctions are linked by the DNA T4 ligase. 70

5.3 Example of a polyacrylamide gel run at 2mM Mg^{2+} concentration. Line 2 and 4 are the DNA ladder from Fig. C.1. Line 1 is a single Holliday junction and line 3 is the confotronic dimer. 71
5.4 Comparison of the migration "speed" (the length in basepairs of a dsDNA migrating until the same height as indicated by the ladder lines) of the single Holliday junction and the confotronic dimer as a function of Mg^{2+} concentration. 72
5.5 Left : scheme of a magnetic tweezer setup, from [112]. Right : 3D representation of the setup of Wilfried Grange in IPCMS on which the future confotronic fibers will be measured. 73
5.6 Full sequence of the four oligonucleotides constituting the Hyperdrive, see Fig. C.2 for more details. 74
5.7 The two extreme configurations of the Hyperdrive construct (without the "legs"). The overhangs on the sides present both on the left and on the right are the non-palindromic "stoppers". When a positive potential is applied at the electrode, the construct lies flat on the surface. The red part is recognized by the enzyme BbsI that cuts the dsDNA strand in the location marked in green. When a negative potential is applied at the electrode, the construct is fully extended away from the surface. 74
5.8 Polyacrylamide gel used to control the assembly of the Hyperdrive. Line 1 and 7 : DNA ladder of Fig. C.1 right. Line 2 and 3 : oligonucleotides constituting the motor, OL 64 and 65 respectively, see Fig. C.2. Line 4 : the fully assembled Hyperdrive. Line 5 and 6 : twice the same content, the assembled Hyperdrive digested by BbsI. 75
5.9 A gold surface coated with florescently labeled DNA strands shows a moving "blob" of fluorescence upon first illumination. 76
5.10 A fluorescent "blob" moving on the surface attracts fluorescent particles suspended in solution along its path. Image obtained through summation of multiple successive frames of a recording. 77
5.11 The heating of the gold surface by the illumination induces convection cells in the fluid above. The DNA strands initially lying on the surface whose fluorescence is quenched are lifted by the resulting flow and thus emit a fluorescence signal. 78
5.12 PIV analysis of the convection flow triggered by the illumination from two subsequent frames of an acquisition, 3mm above the gold surface. The solid lines are constant velocities, the histogram of the velocities is given in Fig. 5.13. The "eye of the storm" shows the center of the illumination spot. . . 79
5.13 Histogram of the velocities represented in Fig. 5.12. Starting from zero velocity at the surface, the flow goes up to dozens of μm/s at 3mm above the surface. 80
5.14 Glass slide with two disks of gold (500μm in diameter, 1mm apart edge to edge). Left : at the start of the illumination. Right : after 26 minutes of continuous illumination. The convection flow induced by the two disks gathers the tracer particles on the line linking them. 81

5.15 PIV analysis of the flow induced by the two gold disks (calculated by the ImageJ pluggin). They show an inversion of the flow between 0.2 and 1mm above the surface. 81

A.1 Mechanical characterization of nylon-6 fibers. Left: The storage modulus vs. frequency for temperatures from 30 to 190°C. Right: The loss modulus vs. frequency for the same temperature range. 87
A.2 2D WAXS intensity profile for the annealed nylon-6 fiber at a) 120°C, b) 185°C, and c) 240°C showing the anisotropy of the signals before melting above 220°C. Note: The fiber axis lies in the vertical direction. 88
A.3 1D WAXS intensity profile for the annealed nylon-6 fiber at a) 120°C, b) 185°C, and c) 240°C and the corresponding fitting curve (light green curve). The red (equatorial), blue (45 degrees oblique) and dark green (meridional) curves correspond to the scattering profiles from the sections in Fig. A.2. The orange curves in c) are the amorphous peaks contributing to the signal for the polymer melt. 89
A.4 Relative longitudinal strain of rolling fiber samples with diameters 0.6 mm and lengths between 10 and 12 cm. 90

B.1 A fiber confined by its own weight in the X-Y plane. When considering a cross section in the X-Z plane, the curvature can be assumed along the X direction. The co-rotating frame is spanned by the vectors e_1 and e_2, with the angle Φ between e_1 and e_2 92

C.1 Description of the bands and fragment sizes for the Gene Ruler DNA ladder, provided by the supplier. Left: Ladder used for the agarose gels. Right : Ladder used for the polyacrylamide gels. 103
C.2 Detailed informations about the oligonucleotides used for the Hyperdrive project, bought from Microsynth, provided by the company. 104
C.3 Emission and absorption spectra of the fluorescent dye atto 565. 105

Arthur BAUMANN

Active Motion and Self-Propulsion of Polymers and Fibres

Résumé

Ce manuscrit de thèse porte sur l'étude de deux projets distincts. Le premier fait état de la conception expérimentale ainsi que de l'étude théorique d'un tout nouveau type de moteur basé sur des fibres de polymères : le fiberdrive. Le fonctionnement de ce moteur s'appuie sur un nouveau concept physique décrit ici, les modes de déformation à énergie élastique nulle. Ces modes de déformation sont entraînés par un flux d'énergie qui provoque une déformation élastique au sein du matériau. Le présent manuscrit développe un modèle théorique qui est confronté à la première réalisation expérimentale de ce type de moteur. Le système réalisé est le moteur le plus simple au monde, un stator sans rotor.

La deuxième partie du manuscrit introduit le concept de confotronique, l'étude de système composés d'unités commutables individuellement coopérant à grande échelle. Ce concept est mis en oeuvre dans la réalisation d'une fibre confotronique à base d'ADN ainsi que dans la conception d'un moteur moléculaire à base d'ADN.

Mots-clés : Matière molle, élasticité, polymères, moteurs, confotronique, ADN, convection

Résumé en anglais

This thesis manuscript deals with the study of two distinct projects. The first deals with the experimental design as well as the theoretical study of a brand new type of engine based on polymer fibers: the fiberdrive. The operation of this engine is based on a new physical concept described here, deformation modes with zero elastic energy (ZEEMs). These deformation modes are driven by a flow of energy that causes elastic deformation within the material. This manuscript develops a theoretical model that is confronted with the first experimental realization of this type of engine. The realized system is the simplest engine in the world, a stator without rotor.

The second part of the manuscript introduces the concept of confotronics, the study of system composed of individually switchable units cooperating on a large scale. This concept is implemented in the realization of a DNA-based confotronic fiber as well as in the design of a DNA-based molecular engine.

Keywords: soft matter, elasticity, polymers, motors, confotronic, DNA, convection